The Astrophysical Journal Supplement Series, 175:48–85, 2008 March

MULTIWAVELENGTH CONSTRAINTS ON THE COSMIC STAR FORMATION HISTORY FROM SPECTROSCOPY: THE REST-FRAME ULTRAVIOLET, Hα, AND INFRARED LUMINOSITY FUNCTIONS AT REDSHIFTS $1.9 \lesssim z \lesssim 3.4$[1]

Naveen A. Reddy,[2,3] Charles C. Steidel,[2] Max Pettini,[4] Kurt L. Adelberger,[5]
Alice E. Shapley,[6] Dawn K. Erb,[7] and Mark Dickinson[3]
Received 2007 May 21; accepted 2007 June 16

ABSTRACT

We use a sample of rest-frame UV-selected and spectroscopically observed galaxies at redshifts $1.9 \leq z < 3.4$, combined with ground-based spectroscopic Hα and *Spitzer* MIPS 24 μm data, to derive the most robust measurements of the rest-frame UV, Hα, and infrared (IR) luminosity functions (LFs) at these redshifts. Our sample is by far the largest of its kind, with over 2000 spectroscopic redshifts in the range $1.9 \leq z < 3.4$ and ~15,000 photometric candidates in 29 independent fields covering a total area of almost a square degree. Our method for computing the LFs takes into account a number of systematic effects, including photometric scatter, Lyα line perturbations to the observed optical colors of galaxies, and contaminants. Taking into account the latter, we find no evidence for an excess of UV-bright galaxies over what was inferred in early $z \sim 3$ LBG studies. The UV LF appears to undergo little evolution between $z \sim 4$ and $z \sim 2$. Corrected for extinction, the UV luminosity density (LD) at $z \sim 2$ is at least as large as the value at $z \sim 3$ and a factor of ~9 larger than the value at $z \sim 6$, primarily reflecting an increase in the number density of bright galaxies between $z \sim 6$ and $z \sim 2$. Our analysis yields the first constraints anchored by extensive spectroscopy on the infrared and bolometric LFs for faint and moderately luminous ($L_{\rm bol} \lesssim 10^{12}\ L_{\odot}$) galaxies. Adding the IR to the emergent UV luminosity, incorporating independent measurements of the LD from ULIRGs, and assuming realistic dust attenuation values for UV-faint galaxies, indicates that galaxies with $L_{\rm bol} < 10^{12}\ L_{\odot}$ account for ≈80% of the bolometric LD and SFRD at $z \sim 2$–3. This suggests that previous estimates of the faint end of the $L_{\rm bol}$ LF may have underestimated the steepness of the faint-end slope at $L_{\rm bol} < 10^{12}\ L_{\odot}$. Our multiwavelength constraints on the global SFRD indicate that approximately one-third of the present-day stellar mass density was formed in subultraluminous galaxies between redshifts $z = 1.9$–3.4.

Subject headings: galaxies: evolution — galaxies: formation — galaxies: high-redshift — galaxies: luminosity function, mass function — galaxies: starburst — infrared: galaxies

Online material: color figures

1. INTRODUCTION

Constraining the star formation history and stellar mass evolution of galaxies is a central component of understanding galaxy formation. Observations of the stellar mass and star formation rate density, the QSO density, and galaxy morphology at both low ($z \lesssim 1$) and high ($z \gtrsim 3$) redshifts indicate that most of the activity responsible for shaping the bulk properties of galaxies to their present form occurred in the epochs between $1 \lesssim z \lesssim 3$ (e.g., Dickinson et al. 2003; Rudnick et al. 2003; Madau et al. 1996; Lilly et al. 1995, 1996; Steidel et al. 1999; Shaver et al. 1996; Fan et al. 2001; Di Matteo et al. 2003; Conselice et al. 2004; Papovich et al. 2003; Shapley et al. 2001; Giavalisco et al. 1996). While this period in the universe was perhaps the most active in terms of galaxy evolution and accretion activity, it was not until recently that advances in detector sensitivity and efficiency, the increased resolution and light-gathering capability afforded by larger 8–10 m class telescopes, and a number of new powerful imagers and spectrographs on space-based missions such as *HST*, *Spitzer*, and *Chandra*, allowed for the study of large numbers of galaxies at $z \sim 2$. These developments have prompted a spate of multiwavelength surveys of high-redshift galaxies from the far-IR/submillimeter to IR, near-IR, optical, and UV, enabling us to examine the SEDs of star-forming galaxies over much of the 7 decades of frequency over which stars emit their light either directly or indirectly through dust processing (e.g., Steidel et al. 2003, 2004; Daddi et al. 2004a, 2004b; Franx et al. 2003; van Dokkum et al. 2003, 2004; Abraham et al. 2004; Chapman et al. 2005; Smail 2003).

The first surveys that efficiently amassed large samples of high-redshift galaxies used the observed $U_n G\mathcal{R}$ colors of galaxies to identify those with a deficit of Lyman continuum flux (e.g., Steidel et al. 1995) in the U_n band (i.e., U "drop-outs") for galaxies at $z \sim 3$. Those initial results have been adapted to select galaxies at higher redshifts ($z > 4$; e.g., Bouwens et al. 2005, 2004; Dickinson et al. 2004; Bunker et al. 2004; Yan et al. 2003) and moderate redshifts ($1.4 \lesssim z \lesssim 3$; Adelberger et al. 2004; Steidel et al. 2004). Combining these high-redshift results with those from *GALEX* (e.g., Wyder et al. 2005), we now have an unprecedented view of the rest-frame UV properties of galaxies from the epoch of reionization to the present, perhaps the only wavelength for which

[1] Based, in part, on data obtained at the W. M. Keck Observatory, which is operated as a scientific partnership among the California Institute of Technology, the University of California, and NASA, and was made possible by the generous financial support of the W. M. Keck Foundation. Also based in part on observations made with the *Spitzer Space Telescope*, which is operated by the Jet Propulsion Laboratory, California Institute of Technology, under a contract with NASA.

[2] California Institute of Technology, MS 105-24, Pasadena, CA 91125.
[3] National Optical Astronomy Observatory, 950 North Cherry Avenue, Tucson, AZ 85719.
[4] Institute of Astronomy, Madingley Road, Cambridge CB3 OHA, UK.
[5] McKinsey & Company, 1420 Fifth Avenue, Suite 3100, Seattle, WA 98101.
[6] Department of Astrophysical Sciences, Peyton Hall, Ivy Lane, Princeton, NJ 08544.
[7] Harvard-Smithsonian Center for Astrophysics, 60 Garden Street, Cambridge, MA 02138.

star-forming galaxies have been studied across more than ~93% of the age of the universe. The accessibility of rest-frame UV wavelengths over almost the entire age of the universe makes rest-frame UV luminosity functions (LFs) useful tools in assessing the cosmic star formation history in a consistent manner.

The foray of observations into the epoch around $z \sim 2$ has occurred relatively recently, and with it have come various determinations of the UV LFs at these epochs (Gabasch et al. 2004; Le Fèvre et al. 2005). Unfortunately, such studies are often limited because either (1) they are purely magnitude limited (resulting in inefficient selection of galaxies at the redshifts of interest and even fewer galaxies with secure spectroscopic redshifts and poorly determined contamination fraction), (2) they generally rely on photometric redshifts that are highly uncertain at $z \sim 2$, and/or (3) they are estimated over a relatively small number of fields such that cosmic variance may be an issue. While purely magnitude limited surveys allow one to easily quantify the selection function, as we show below, Monte Carlo simulations combined with accurate spectroscopy can be used to quantify even the relatively complicated redshift selection functions and biases of color-selected samples of high-redshift galaxies. This "simulation" approach allows one to assess a number of systematics (e.g., photometric imprecision, perturbation of colors due to line strengths, etc.) and their potential effect on the derived LF; these systematic effects have been left untreated in previous calculations of the LFs at $z \sim 2$–3 (Gabasch et al. 2004; Le Fèvre et al. 2005) but are nonetheless found to be important in accurately computing the LF (e.g., Adelberger & Steidel 2000; Bouwens et al. 2004, 2005, 2006).

For the past several years, the main focus of our group has been to assemble a large sample of galaxies at the peak epoch of galaxy formation and black hole growth, corresponding to redshifts $1.5 \lesssim z \lesssim 2.6$, in multiple independent fields. The selection criteria aim to identify actively star-forming galaxies at $z \sim 2$ with the same range in intrinsic UV color and extinction as Lyman break galaxies (LBGs) at $z \sim 3$ (Steidel et al. 2003). The color selection criteria are described in Adelberger et al. (2004) and Steidel et al. (2004). Initial results from the survey, including analyses of the star formation rates, stellar populations, stellar and dynamical masses, gas-phase metallicities, morphologies, outflow properties, and clustering are presented in several papers (e.g., Shapley et al. 2005; Adelberger et al. 2005a, 2005b; Erb et al. 2006a, 2006b, 2006c; Reddy et al. 2006b, 2005; Reddy & Steidel 2004; Steidel et al. 2005). With a careful accounting of extinction, photometric imprecision, and systematic effects caused by observational limitations, rest-frame UV-selected samples can be used to estimate the cosmological star formation history (e.g., Steidel et al. 1999; Adelberger & Steidel 2000; Bouwens et al. 2004, 2005, 2006; Bunker et al. 2004, 2006).

There are primarily two methods by which one can attempt to construct "complete" luminosity functions that make a reasonable account of all star formation at a given epoch. The first method is to observe galaxies over as wide a range in wavelengths as possible in order to establish a census of all galaxies that dominate the star formation rate density. For example, the union of rest-frame UV (Adelberger et al. 2004; Steidel et al. 2004), rest-frame optical (Franx et al. 2003; Daddi et al. 2004b), and submillimeter-selected samples (e.g., Smail et al. 1997; Hughes et al. 1998; Barger et al. 1998; Blain et al. 2002; Chapman et al. 2005) should account for optically bright galaxies with little to moderate dust extinction as well as the population of optically faint and heavily reddened galaxies. One can then examine the intersection between these various samples and, taking into account overlap, compute the total star formation rate density (Reddy et al. 2005). Unfortunately, this technique poses several challenging problems, not the least of which are the practicality of obtaining multiwavelength data in a large number of uncorrelated fields, disparate data quality and photometric depth between optical and near-IR images, and the inefficiency of spectroscopically identifying galaxies in near-IR–selected samples to properly quantify the selection function.

The second approach, and the one we adopt in this paper, is to estimate sample completeness by way of simulations. This method involves simulating many realizations of the intrinsic distribution of galaxy properties at high redshift, subjecting these realizations to the same photometric methods and selection criteria as applied to real data, and adjusting the simulated realizations until convergence between the expected and observed distribution of galaxy properties is achieved. The method thus corrects for a large fraction of galaxies that might be "missing" from the sample, just as long as some of them are spectroscopically observed. The obvious disadvantage of this method is that some (e.g., optically faint) galaxies will never be scattered into our selection window and hence we cannot account for such galaxies in our analysis. However, multiwavelength data in several of our fields enable us to quantify the magnitude of, and correct for, the incompleteness resulting from objects that never scatter into our sample. Simulations such as the kind presented in this paper become even more important at higher redshift ($z \gtrsim 4$), where no corresponding multiwavelength data exist to assess the fraction of galaxies that are not recovered by color selection. In our case, applying the Monte Carlo method to joint photometric and spectroscopic samples of high-redshift galaxies allows one to assess the systematic effects of photometric scattering and the intrinsic variation in colors due to line emission and absorption with unprecedented accuracy. In this paper, we take advantage of a large sample of spectroscopically confirmed star-forming galaxies to arrive at the first completeness-corrected spectroscopic estimate of the UV LF and star formation rate density (SFRD) at $z \sim 2$, computed across the many independent fields of our survey. We extend our results by using spectroscopy of Lyman break galaxies in many new independent fields to recompute the UV LF and SFRD at $z \sim 3$.

While considerable progress in quantifying the cosmic star formation history can be achieved by UV observations alone, the most robust determination can only come from an analysis at multiple wavelengths, where systematic effects (e.g., extinction) can be corrected for. In addition, assessing the star formation history consistently at several different wavelengths allows for a useful cross-check between results and may reveal any underlying trends between the star-forming properties of galaxies and redshift. In this paper, we combine extensive multiwavelength data in our fields with our spectroscopically derived completeness corrections to measure the rest-frame UV, Hα, and infrared luminosity functions at redshifts $z \sim 2$–3. The primary goal of this paper is to then use these luminosity functions to evaluate the cosmic star formation history in a consistent manner across 4 decades of wavelength.

The outline of this paper is as follows. In § 2, we describe the fields of our survey and the color criteria used to selected candidate galaxies at $z \sim 2$. We then proceed with a description of the spectroscopic follow-up and quantify the fraction of contaminants, including low-redshift ($z < 1$) star-forming galaxies and low- and high-redshift active galactic nuclei (AGNs) and QSOs, within the sample. We conclude § 2 by demonstrating that the redshift distribution for the spectroscopic sample is not significantly biased when compared with the redshift distribution of all photometric candidates at $z \sim 2$. In § 3, we detail the Monte Carlo method used to assess both photometric bias and error, the effect of Lyα line perturbations on the observed rest-UV colors

TABLE 1
SURVEY FIELDS

Field Name	α[a] (J2000.0)	δ[b] (J2000.0)	Field Size (arcmin^2)	N_{BX}[c]	$N_{BX}(1.9 \leq z < 2.7)$[d]	N_{LBG}[e]	$N_{LBG}(2.7 \geq z < 3.4)$[f]
Q0000	00 03 25	−26 03 37	18.9	...	...	28	12
CDFa	00 53 23	12 33 46	78.4	...	...	100	30
CDFb	00 53 42	12 25 11	82.4	...	...	121	21
Q0100	01 03 11	13 16 18	42.9	345	65	100	18
Q0142	01 45 17	−09 45 09	40.1	287	72	100	20
Q0201	02 03 47	11 34 22	75.7	...	...	87	13
Q0256	02 59 05	00 11 07	72.2	...	...	120	42
Q0302	03 04 23	−00 14 32	244.9	...	...	191	29
Q0449	04 52 14	−16 40 12	32.1	188	40	88	13
B20902	09 05 31	34 08 02	41.8	...	...	78	34
Q0933	09 33 36	28 45 35	82.9	...	...	211	47
Q1009	10 11 54	29 41 34	38.3	306	33	137	25
Q1217	12 19 31	49 40 50	35.3	240	26	65	11
GOODS-N	12 36 51	62 13 14	155.3	909	138	210	62
Q1307	13 07 45	29 12 51	258.7	1763	40	564	8
Westphal	14 17 43	52 28 49	226.9	612	39	334	177
Q1422	14 24 37	22 53 50	113.0	...	...	453[g]	92[h]
3C 324	15 49 50	21 28 48	44.1	...	...	51	10
Q1549	15 51 52	19 11 03	37.3	243	49	119	46
Q1623	16 25 45	26 47 23	290.0	1348	209	580	24
Q1700	17 01 01	64 11 58	235.3	1472	92	438	38
Q2206	22 08 53	−19 44 10	40.5	213	49	52	22
SSA 22a	22 17 34	00 15 04	77.7	...	...	146	47
SSA 22b	22 17 34	00 06 22	77.6	...	...	89	28
Q2233	22 36 09	13 56 22	85.6	...	...	94	36
DSF 2237b	22 39 34	11 51 39	81.7	...	...	176	45
DSF 2237a	22 40 08	11 52 41	83.4	...	...	121	30
Q2343	23 46 05	12 49 12	212.8	1018	128	428	25
Q2346	23 48 23	00 27 15	280.3	1069	37	171	1
Total	...	...	3186.1	10013	1017	5452	1006

[a] Right ascension in hours, minutes, and seconds.
[b] Declination in degrees, arcminutes, and arcseconds.
[c] Number of BX candidates to $\mathcal{R} = 25.5$.
[d] Number of spectroscopically confirmed BX candidates with redshifts $1.9 \leq z < 2.7$, excluding those whose spectra indicate an AGN/QSO. Note that the total number of galaxies, excluding AGNs and QSOs, with spectroscopic redshifts $1.9 \leq z < 2.7$ in the survey (total in all fields is 1288) is larger than the numbers given here since a significant fraction of LBG and BM candidates lie at these redshifts.
[e] Number of LBG candidates to $\mathcal{R} = 25.5$.
[f] Number of spectroscopically confirmed LBG candidates with redshifts $2.7 \leq z < 3.4$, excluding those whose spectra indicate an AGN/QSO. Note that the total number of galaxies, excluding AGNs and QSOs, with spectroscopic redshifts $2.7 \leq z < 3.4$ in the survey (total in all fields is 1058) is larger than the numbers given here since a small fraction of BX candidates lie at these redshifts.
[g] Number includes 180 galaxies with $25.5 < \mathcal{R} \leq 26.0$.
[h] Number includes 10 galaxies with $25.5 < \mathcal{R} \leq 26.0$.

of galaxies, and the procedure used to correct our sample for completeness. Our results pertaining to the intrinsic Lyα equivalent width and reddening distributions of $1.9 \leq z < 3.4$ galaxies are discussed in § 4. Results on the rest-frame UV, IR, and Hα LFs are presented respectively in §§ 5, 6, and 7. Finally, we discuss the implications of our results for the luminosity and global star formation rate densities in § 8. A flat ΛCDM cosmology is assumed with $H_0 = 70$ km s^{-1} Mpc^{-1}, $\Omega_\Lambda = 0.7$, and $\Omega_m = 0.3$.

2. DATA: SAMPLE SELECTION AND SPECTROSCOPY

2.1. *Fields*

Our $z \sim 2$ survey is being conducted primarily in fields chosen for having $V \leq 17.5$ mag QSOs with redshifts $2.5 \lesssim z \lesssim 2.8$, ideally placed to study the correlation between $z \sim 2$ galaxies and H I and high-metallicity (e.g., C IV) absorbing systems in the intergalactic medium (IGM; see Adelberger et al. 2005b). We have extended our survey to include the GOODS-North field (Dickinson et al. 2003; Giavalisco et al. 2004), encompassing the original HDF–North field (Williams et al. 1996, 2000), and the Westphal field (currently encompassed by the large Extended Groth Strip survey) to take advantage of the multiwavelength data amassed for these fields. Imaging was conducted under similar conditions as the $z \sim 3$ fields of Steidel et al. (2003). The 14 fields of the $z \sim 2$ survey are summarized in Table 1 (instruments used and dates of observation are shown in Table 1 of Steidel et al. 2004).

We have expanded significantly the number of spectroscopically confirmed LBGs beyond the original sample from 17 fields presented in Steidel et al. (2003) by including those LBGs selected in the newer fields of the $z \sim 2$ survey. We have used these new spectroscopic redshifts, in addition to those previously published in Steidel et al. (2003), to reevaluate the UV LF and SFRD at $z \sim 3$. Fields where we have carried out LBG selection are also listed in Table 1.

One of the unique advantages of our analysis is that we use a large number of uncorrelated fields (14 and 29 for the $z \sim 2$ and $z \sim 3$ surveys, respectively), combined with a large sample of spectroscopic redshifts between $1.9 \leq z < 3.4$, in order to

compute the LF, negating the need for uncertain normalization corrections to account for clustering and cosmic variance. For example, we find evidence for significant large-scale structure within several fields of the $z \sim 2$ survey (e.g., Steidel et al. 2005), generally characterized by overdensities in redshift space above what would be expected given our redshift selection function. By averaging results over many fields well distributed throughout the sky, we can estimate the LF insensitive to variations in large-scale structure, and furthermore estimate the magnitude of the effect of cosmic variance on the results. The total area of all of the independent fields of the $z \sim 3$ survey is $\sim$3200 arcmin^2, or close to a full square degree. The $z \sim 2$ survey area is $\sim$1900 arcmin^2. Despite the smaller area covered by the $z \sim 2$ survey, there are roughly twice as many BX candidates as LBGs given the larger surface density of the former.

2.2. *Photometry*

Photometry was performed using a modified version of FOCAS (Valdes 1982). Object detection was done at $\mathcal{R}$ band, and $G - \mathcal{R}$ and $U_n - G$ colors were computed by applying the $\mathcal{R}$-band isophotal apertures to the G and U_n images (see Steidel et al. 2003, 2004 for further details). The optical images have typical depth of $\mathcal{R} \sim 27.5$ as measured through a $\sim 3''$ diameter aperture (3 σ). Field-to-field variations in photometry are dominated by systematics due to the different instruments, filter sets, and slightly varying observing conditions when the fields were imaged. These field-to-field systematics are negligible compared to measurement errors. We have incorporated some of these effects (e.g., seeing, air mass of the observation, CCD response, and filter shape) in computing the expected colors of galaxies with known intrinsic properties. Modeling all the field-to-field variations in photometry rapidly becomes a very complex problem, infeasible to resolve within a reasonable time frame. The remaining biases (e.g., errors in the zero points used) are discussed in § 3.2.

2.3. *Color Selection*

Even with a priori knowledge of the intrinsic properties of all $z \sim 2$ galaxies, constructing a practical set of selection criteria to select all galaxies in any desired redshift range and reject all others is an intractable problem. One extreme is to select all objects down to a given magnitude limit, such as in flux-limited surveys of high-redshift galaxies, but unfortunately such studies suffer from significant amounts of foreground contamination. Color-selected samples have the advantage of allowing one to specifically target a desired redshift range while minimizing the number of interlopers. Perhaps the most successful of the various color criteria that have been designed to select high-redshift galaxies is rest-frame UV color selection, initially used to target galaxies at $z \sim 3$ (Steidel et al. 1995), and extended to higher redshifts (e.g., Bouwens et al. 2005, 2004; Bunker et al. 2004; Dickinson et al. 2004; Yan et al. 2003). The success of this technique is partly due to its simplicity in that only a few broadband filters are required to assemble such samples. Further, at lower redshifts ($1.4 \lesssim z \lesssim 3.5$), galaxies can be spectroscopically observed and precise redshifts can be obtained in a short amount of observing time on 8–10 m class telescopes. Color-selected high-redshift galaxy surveys will, as a consequence, have rather complex selection functions. The approach described in § 3 allows one to quantify such selection functions with relative ease.

The criteria used to select galaxies with redshifts $1.9 \lesssim z \lesssim 2.7$ based on their rest-frame UV colors were designed to recover objects with intrinsic properties similar to those of $z \sim 3$ LBGs. The colors at $z \sim 2$ were estimated from spectral synthesis analysis of 70 LBGs with broadband $U_n G \mathcal{R} J K_s$ photometry and spectroscopic redshifts (Adelberger et al. 2004; Steidel et al. 2004). Initial spectroscopy of $z \sim 2$ candidates led to a refinement of the criteria used to select galaxies at redshifts $1.9 \lesssim z \lesssim 2.7$ to their present form:

$$\begin{aligned} G - \mathcal{R} &\geq -0.2, \\ U_n - G &\geq G - \mathcal{R} + 0.2, \\ G - \mathcal{R} &\leq 0.2(U_n - G) + 0.4, \\ U_n - G &\leq G - \mathcal{R} + 1.0, \end{aligned} \tag{1}$$

termed as "BX" selection (Adelberger et al. 2004; Steidel et al. 2004), with fluxes in units of AB magnitudes (Oke & Gunn 1983). Candidates were selected to $\mathcal{R} = 25.5$ to ensure a sample of galaxies amenable to spectroscopic follow-up. This limit corresponds to an absolute magnitude at observed $\mathcal{R}$-band that is 0.6 mag fainter at $z = 2.2$ (the mean redshift of BX candidates with $z > 1$) than at $z \sim 3$. In addition, we exclude all sources with $\mathcal{R} < 19$ that are saturated in our images, all of which are stars. The above criteria yielded 10,013 candidates in the 14 fields, with an average surface density of $\sim$5 arcmin^{-2}, uncorrected for contamination from objects with redshifts $z < 1.4$ (see § 2.5). The number of candidates in each field are summarized in Table 1. Note that we did not select BX galaxies in 15 fields of the $z \sim 3$ survey (Steidel et al. 2003) since spectroscopy of these fields was carried out before the $z \sim 2$ survey began.

The color criteria used to select LBGs at redshifts $2.7 \lesssim z \lesssim 3.4$ are published in Steidel et al. (2003) and are summarized here for convenience:

$$\begin{aligned} G - \mathcal{R} &\leq 1.2, \\ U_n - G &\geq G - \mathcal{R} + 1.0. \end{aligned} \tag{2}$$

These criteria form the superset of the individual sets of criteria for "C," "D," "M," and "MD" candidate types given in Table 4 of Steidel et al. (2003). Hereafter we will refer to all these different candidate types as LBGs. Candidates were selected to $\mathcal{R} = 25.5$, except in the field Q1422, where the photometric depth allowed selection of candidates to $\mathcal{R} = 26.0$. The number of $z \sim 3$ candidates in each field are also summarized in Table 1. Given the constraints of the color criteria and the $\mathcal{R} = 25.5$ spectroscopic limit, the combined BX and LBG samples constitute $\sim$25% of the total $\mathcal{R}$ and K_s-band counts to $\mathcal{R} = 25.5$ and $K_s(\mathrm{AB}) = 24.4$, respectively.

2.4. *Spectroscopic Follow-up*

The spectroscopic follow-up of candidates is discussed extensively in Steidel et al. (2003) and Steidel et al. (2004). Of the 10,013 BX candidates, we have targeted 24% (2382 out of 10,013) with spectroscopy, yielding 1711 redshift identifications, or a 72% success rate averaged over all fields. As discussed in § 2.6, the spectroscopic success rate is primarily determined by the observing conditions, and subsequent spectroscopy of spectroscopic failures indicates they have similar redshift distribution as successes. Similarly, of the 5452 LBG candidates, 1903 were targeted with 1492 successful redshifts. Figure 1 shows arbitrarily normalized redshift distributions for the BX and LBG samples. The mean spectroscopic redshifts for the BX and LBG samples, when restricted to those objects with $z > 1$, are $\langle z \rangle = 2.20 \pm 0.32$ and $\langle z \rangle = 2.96 \pm 0.26$, respectively. Preliminary versions of these histograms, along with sample spectra of BX galaxies and LBGs, are presented in Steidel

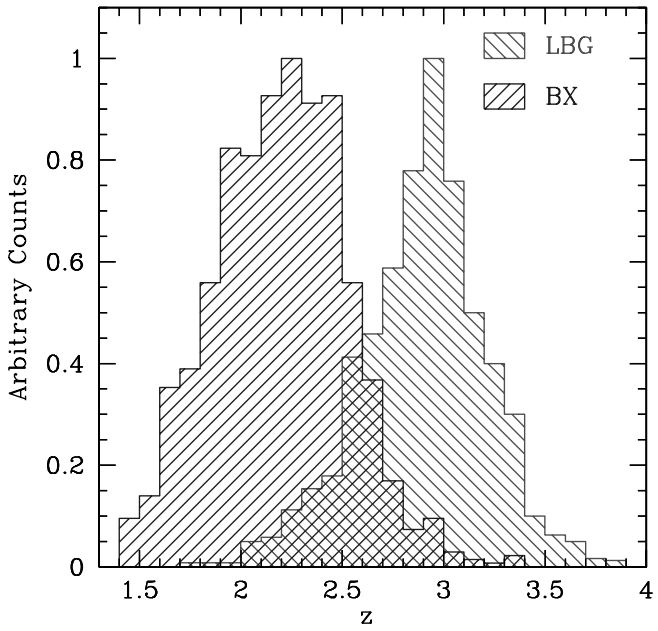

FIG. 1.—Arbitrarily normalized spectroscopic redshift distributions of galaxies with $z > 1.4$ in the BX and LBG samples. The total number of galaxies represented here is 2569. [*See the electronic edition of the Supplement for a color version of this figure.*]

et al. (2003) and Steidel et al. (2004). Table 2 lists the spectroscopic fractions relevant for the BX and LBG samples.

2.5. *Interloper Contribution and AGNs*

The region of color space defined by BX selection (e.g., Fig. 4) is also expected to include galaxies outside of the targeted redshift range, including star-forming galaxies at $z \lesssim 0.2$ and stars (see Fig. 10 of Adelberger et al. 2004). Spectroscopy shows that there is indeed a subset of BX candidates that are interlopers—candidates with redshifts $z < 1.4$—with a much higher contamination rate among candidates with $\mathcal{R} < 23.5$, as indicated in Table 3. One can impose a rough magnitude cutoff to only consider those candidates with $\mathcal{R} \geq 23.5$, but this would preclude the analysis of the bright end of the BX and LBG luminosity distributions, as well as more detailed studies of the UV spectra of optically bright objects. Other options to reduce the contamination fraction include using the $\mathcal{R} - K$ color where the associated bands no longer bracket strong spectral breaks for low-redshift sources. For example, the *BzK* criteria of Daddi et al. (2004b) can be used to reduce the foreground contamination fraction in color-selected samples.

The interloper fractions are apt to decrease as the survey progresses and we become more adept at excluding them from masks based on other multiwavelength data, such as their $\mathcal{R} - K$ colors. However, until now, we have not used any of the techniques discussed above to actively discriminate against placing possible interlopers on slit masks; doing so would complicate our ability to apply the observed contamination fractions to determine the interloper rate among all BX/LBG sources. Therefore, the fractions in columns (4) and (7) of Table 3 are assumed to represent the overall fraction of interlopers as a function of $\mathcal{R}$ for the photometric samples. For the BX sample, most of the contamination at bright magnitudes arises from foreground galaxies. For the LBG sample, most of the contamination arises from stars. Applying a bright magnitude limit of $\mathcal{R} = 23.5$ will reduce the overall contamination fractions of the BX and LBG samples to 9% and 3%, respectively.

The BX sample also includes a small number of broad-lined QSOs and broad- and narrow-line ($\sigma < 2000$ km s^{-1}) AGNs whose rest-UV colors are similar to those of high-redshift star-forming galaxies but which show prominent (and in some cases broad) emission lines such as Lyα, C IV, and N V. The detection rate of such sources is $\sim$2.8% (similar to the rate found among UV-selected $z \sim 3$ galaxies; Steidel et al. 2002) but is a strong function of apparent magnitude where all but two of the objects with $\mathcal{R} < 22.0$ and $z > 1$ are QSOs. The fractions of spectroscopically confirmed BXs and LBGs that show high-ionization UV lines indicative of an AGN or QSO are listed in Table 2. As

TABLE 2
SPECTROSCOPIC AND AGN/QSO FRACTIONS OF THE BX AND LBG SAMPLES

	BX					LBG				
$\mathcal{R}$	$N_{\rm phot}$[a]	$N_{\rm spec}$[b]	$f_{\rm spec}$[c]	$f_{\rm AGN}$[d]	$f_{\rm AGN}(z \geq 1.4)$[e]	$N_{\rm phot}$[f]	$N_{\rm spec}$[g]	$f_{\rm spec}$[h]	$f_{\rm AGN}$[i]	$f_{\rm AGN}(z \geq 1.4)$[j]
19.0–22.0	620	74	0.12	0.12	0.78	142	30	0.21	0.33	1.00
22.0–22.5	162	31	0.19	0.00	0.00	34	7	0.21	0.17	1.00
22.5–23.0	252	77	0.31	0.05	0.20	71	25	0.35	0.23	0.67
23.0–23.5	466	178	0.38	0.01	0.02	137	62	0.45	0.07	0.10
23.5–24.0	1053	330	0.31	0.03	0.03	392	177	0.45	0.02	0.03
24.0–24.5	1894	511	0.27	0.01	0.01	881	398	0.45	0.02	0.03
24.5–25.0	2741	341	0.12	<0.01	<0.01	1617	442	0.27	0.01	0.01
25.0–25.5	2819	169	0.06	0.02	0.02	1994	336	0.17	<0.01	<0.01
25.5–26.0	...	...	...	...	...	180[k]	15[k]	0.08[k]	0.00[k]	0.00[k]
Total	10007	1711	0.17	0.02	0.02	5448	1492	0.27	0.03	0.03

[a] Number of BX candidates.
[b] Number of BX candidates with spectroscopic redshifts.
[c] Fraction of BX candidates with spectroscopic redshifts.
[d] Fraction of AGNs/QSOs in BX sample with spectroscopic redshifts.
[e] Fraction of AGNs/QSOs in BX sample with $z_{\rm spec} \geq 1.4$.
[f] Number of LBG candidates.
[g] Number of LBG candidates with spectroscopic redshifts.
[h] Fraction of LBG candidates with spectroscopic redshifts.
[i] Fraction of AGNs/QSOs in LBG sample with spectroscopic redshifts.
[j] Fraction of AGNs/QSOs in LBG sample with $z_{\rm spec} \geq 1.4$.
[k] Numbers are for Q1422 field.

TABLE 3
INTERLOPER ($z < 1.4$) STATISTICS OF THE BX AND LBG SAMPLES

	BX			LBG		
$\mathcal{R}$ (1)	$N_{z\geq 0}$[a] (2)	$N_{0\leq z<1.4}$[b] (3)	$f_{0\leq z<1.4}$[c] (4)	$N_{z\geq 0}$[a] (5)	$N_{0\leq z<1.4}$[b] (6)	$f_{0\leq z<1.4}$[c] (7)
19.0–22.0.....	74	65	0.88	30	20	0.67
22.0–22.5.....	31	28	0.90	7	5	0.71
22.5–23.0.....	77	56	0.73	25	17	0.68
23.0–23.5.....	178	65	0.37	62	19	0.31
23.5–24.0.....	330	58	0.18	177	19	0.11
24.0–24.5.....	511	37	0.07	398	13	0.03
24.5–25.0.....	341	19	0.06	442	1	<0.01
25.0–25.5.....	169	4	0.02	336	2	<0.01
25.5–26.0.....	...	...	...	15	0	<0.01
Total	1711	332	0.19	1492	96	0.06

[a] Number of sources with spectroscopic redshifts.
[b] Number of sources with $z < 1.4$.
[c] Fraction with $z < 1.4$.

discussed in Reddy et al. (2006a) we have found the presence of additional AGNs in the sample based on either X-ray or IR data. For the analysis presented here, we exclude AGNs from the sample based on the presence of high-ionization UV emission lines. The effect of including AGNs/QSOs in the rest-frame UV LF is discussed further in § 8.2.

2.6. *Spectroscopic Completeness*

Assessing photometric and spectroscopic completeness is a key ingredient in determining the total completeness of our survey. The photometric completeness (i.e., the fraction of galaxies at redshifts $1.9 \lesssim z \lesssim 3.4$ that satisfy either the BX or LBG color selection) is discussed in § 3. Here we focus on the extent to which the redshift distribution of the spectroscopic sample reflects that of the photometric sample as a whole. There are several observations that suggest that the redshift selection functions for the spectroscopic samples reflect the overall redshift selection functions had we obtained spectroscopic redshifts for every single candidate. First, the success of measuring redshifts is primarily a function of the weather conditions (e.g., cirrus, seeing) at the time of observation, with a 90% success rate in the best conditions. Repeat observations of objects for which we were unable to secure a redshift initially indicate that the redshift distribution of spectroscopic failures is similar to that of spectroscopic successes. In other words, our failure to measure a redshift is generally not attributable to the redshift being far from what one would expect from the color selection criteria.

Second, Figure 2 demonstrates that optical apparent magnitude is independent of redshift for the BX and LBG samples, keeping in mind that the $\mathcal{R} = 25.5$ limit is applied to the photometric (and hence also spectroscopic) sample. This is important because if the redshifts of objects were correlated with their optical apparent magnitude, then we might expect the redshift distribution of spectroscopically identified candidates to differ from candidates in general given that our mask prioritization scheme gives more weight to candidates with magnitudes in the range $23.5 \lesssim \mathcal{R} \lesssim 24.5$ (§ 2.4). Given these results, we proceed under the assumption that spectroscopic selection does not significantly bias the recovered redshift distribution relative to that of the underlying photometric sample.

It is instructive to note that, with respect to the redshift distribution, there are two forms of completeness we must concern ourselves with. The first is how well the redshift selection function for the *spectroscopic* sample reflects the underlying selection function for the *photometric* sample. We have just argued that the spectroscopic and photometric samples must have similar redshift distributions. The second is how well the *photometric* selection function reflects the underlying redshift distribution of *all* star-forming galaxies. As discussed in § 5.5, the number density of galaxies is roughly constant as a function of redshift in the redshift ranges $1.9 \leq z < 2.7$ and $2.7 \leq z < 3.4$. The modulation of this intrinsic (roughly constant) redshift distribution into the Gaussian distribution of Figure 1 can be modeled with great precision by way of Monte Carlo simulations, as we demonstrate below. Readers who wish to skip directly to the results may proceed to § 4.

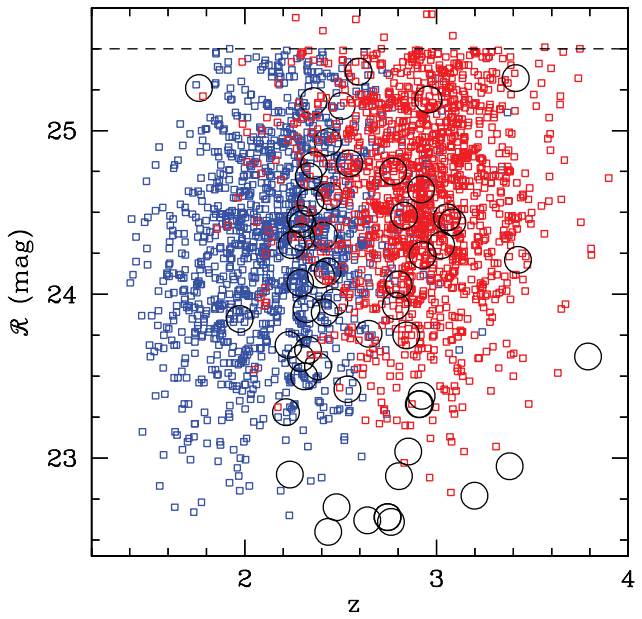

FIG. 2.—Apparent magnitude vs. redshift for spectroscopically confirmed BX objects (*in blue*) and LBGs (*in red*) in the redshift range $1.4 < z < 4.0$. AGNs/QSOs in the BX and LBG samples are denoted by the large open circles. The dashed horizontal line indicates the self-imposed $\mathcal{R} = 25.5$ limit to the photometric (and hence spectroscopic) samples. The few objects shown with magnitudes fainter than this limit are from the Q1422 field.

3. METHOD: INCOMPLETENESS CORRECTIONS

A primary aim of this analysis is to connect the observed properties of BX galaxies and LBGs to the underlying population of *all* star-forming galaxies at redshifts $z \sim 2$–3. To this end, we have constructed a plausible population of galaxies with a range of redshifts ($1.4 \lesssim z \lesssim 4.0$), luminosities, and reddening, and determined the fraction of these galaxies that would satisfy our color criteria. As is typically done, inverting these fractions and applying them to the observed counts allows one to estimate the underlying distribution of galaxies. In this section we discuss in detail the procedure used to reconstruct the intrinsic population of galaxies at redshifts $1.9 \lesssim z \lesssim 3.4$.

3.1. *Monte Carlo Simulations*

We employed a Monte Carlo approach both to (1) determine the transformation between the intrinsic properties of a galaxy (e.g., its luminosity, reddening, and redshift) and its observed rest-UV colors and (2) quantify the effects of photometric errors in their measured rest-UV colors, similar to the method used in Shapley et al. (2001), Adelberger & Steidel (2000), and Steidel et al. (1999). Template galaxies with intrinsic sizes of 0.05″–0.8″ and exponential light profiles were convolved with the average

PSF (typically 1″) of the optical images. Variations in the light profile used (e.g., exponential; de Vaucouleurs) have a negligible effect on the simulation results; the intrinsic size of the light-emitting region (∼0.5″–0.8″ based on *HST* ACS observations; Law et al. 2007) is almost always smaller than the seeing disk.

The expected rest-UV colors of a galaxy with a particular redshift and reddening are computed by assuming a G. Bruzual & S. Charlot (1996, private communication) template galaxy with constant star formation for 1 Gyr and a Calzetti et al. (2000) extinction law.[8] The BX selection criteria were designed to select $z \sim 2$ galaxies with a range of SEDs similar to those found for LBGs at higher redshifts (Adelberger et al. 2004). Spectral synthesis modeling and external multiwavelength information indicates that most UV-selected $z \sim 2$–3 galaxies can be described by long-duration (>100 Myr) starbursts and the constant star formation model described above should reproduce this behavior to the extent required by the simulations (e.g., Shapley et al. 2005). In particular, the rest-UV colors of galaxies are essentially constant after 10^8 yr of star formation, once the mix of O and B stars stabilizes.[9] The Calzetti et al. (2000) reddening law reproduces the *average* expected star formation rates of $z \sim 2$–3 galaxies based on extinction free stacked X-ray and radio estimates (e.g., Reddy & Steidel 2004) and further reproduces the average dust obscuration of galaxies with bolometric luminosities in the range $10^{11}\ L_\odot \lesssim L_{\rm bol} \lesssim 10^{12.2}\ L_\odot$, where the bulk of our sample lies (Reddy et al. 2006b). The use of a constant star-forming model and the Calzetti reddening law should therefore adequately parameterize the SEDs of most optically bright star-forming galaxies at $z \sim 2$–3. An advantage of spectroscopic follow-up of photometrically selected BX galaxies and LBGs is that we can also constrain the effects of IGM opacity and Lyα absorption/emission (§ 3.3), both of which are redshift dependent. All of these perturbing effects will result in a wide range of spectral shapes and should account for any galaxies that are not exactly described by a Calzetti et al. (2000) attenuated constant star-forming SED.

A large distribution of galaxy colors was then computed assuming a particular luminosity function (LF) and the observed $E(B-V)$ distribution for spectroscopically confirmed galaxies. Small variations in the assumed Schechter parameters of the LF do little to change the results, since our main goal is to sufficiently populate redshift space and rest-UV color space with a realistic distribution of objects. The results are also insensitive to small variations in the assumed $E(B-V)$ distribution as long as the range of $E(B-V)$ chosen reflects that expected for the galaxies. A by-product of the luminosity function analysis is that we also compute the best-fit underlying $E(B-V)$ distribution. The validity of the assumed LF and $E(B-V)$ distributions can be tested by comparing with the inferred LF and $E(B-V)$ distributions. Significant differences between the assumed and inferred distributions imply that the initial assumptions for the LF and $E(B-V)$ distribution were different from their true values. The colors were corrected for opacity due to the IGM, assuming a Madau (1995) model, and corrected for filter and CCD responses and air masses appropriate for the each field of the survey.

The intrinsic rest-UV colors are randomly assigned to simulated galaxies that are then added to the images in increments of 200 galaxies at a time. This ensures that the image including all added (simulated) galaxies has confusion statistics similar to the observed image, since this will affect the photometric uncertainties and systematics due to blending. We then attempt to recover these simulated galaxies using the same software used to recover the real data and record whether a simulated galaxy is detected and what its observed magnitude and colors are. We repeated this procedure until approximately 2×10^5 simulated galaxies were added to each of the U_n, G, and $\mathcal{R}$ images of each field. This large number of simulated galaxies is necessary in order to sufficiently populate each bin of luminosity, reddening, and redshift.

The end product of the simulations are sets of transformations for each field that give the probabilities that galaxies with intrinsic luminosities (L'), reddenings (E'), and redshifts (z') will be observed to have luminosities L, reddenings E, and redshifts z (or alternatively, the probabilities that galaxies with true properties $L'E'z'$ will be measured with a particular set of rest-UV colors).

3.2. *Photometric Uncertainties*

We have used the results of the Monte Carlo simulations (§ 3.1) to estimate the photometric errors and determine optimal bin sizes for subsequent analysis. For each simulated galaxy that is detected, we have recorded the true and measured rest-UV colors. As the uncertainties may vary depending on magnitude or color, we have binned the detected galaxies in magnitude and color for each field and have only considered galaxies that would be detected as candidates since these are the only objects that are relevant to our analysis. We used bin sizes of 0.5 mag in $\mathcal{R}$ and 0.2 mag in $U_n - G$ and $G - \mathcal{R}$ color to determine the uncertainties in the recovered magnitudes and colors of objects in each field. Systematic bias in the $G - \mathcal{R}$ color was estimated by computing the quantity $\Delta[G-\mathcal{R}] = (G-\mathcal{R})_{\rm meas} - (G-\mathcal{R})_{\rm true}$, which was typically $\lesssim 0.04$ mag with uncertainty estimated to be $\sigma(\Delta[G-\mathcal{R}]) \sim 0.09$ mag. The typical random uncertainties in $U_n - G$ and $\mathcal{R}$ are ∼0.15 mag and ∼0.13 mag, respectively. These quantities were determined using the same method as presented in Shapley et al. (2001, 2005) and Steidel et al. (2003). The uncertainties were generally larger for objects faint in $\mathcal{R}$ (Steidel et al. 2003). The field-to-field results were consistent with each other (i.e., the typical biases and uncertainties from field-to-field were within 0.1 mag of each other). The photometric errors are slightly smaller in size than the bin sizes (0.2 mag) used to estimate the reddening and luminosity distribution. A more refined method discussed in § 3.4.2 will correct for any systematic scattering of objects into adjacent bins due to photometric error and/or Lyα perturbations to the colors.

3.3. Lyα *Equivalent Width* ($W_{\rm Ly\alpha}$) *Distribution*

The presence of Lyα absorption and/or emission can perturb the observed rest-UV colors of $z \sim 2$–3 galaxies by up to 0.75 mag depending on the redshift and intrinsic (rest-frame) Lyα equivalent width $W_{\rm Ly\alpha}$. To investigate these effects, we measured the $W_{\rm Ly\alpha}$ for 414 spectroscopically confirmed BX galaxies with redshifts $1.9 \leq z < 2.7$ in 7 different fields of the BX survey. The resulting distribution for all galaxies with $1.9 \leq z < 2.7$ is shown in Figure 3*a*, with the characteristic asymmetric shape. The photometric scattering probability associated with this $W_{\rm Ly\alpha}$ distribution is shown in Figure 4. The two shaded "zones" in Figure 4 reflect the redshift ranges where Lyα falls within the U_n and G bands. This figure demonstrates how galaxies that are targeted by the BX criteria can be shifted out of the BX selection window due to Lyα emission or absorption.

Since our ultimate goal is to determine how the $W_{\rm Ly\alpha}$ distribution perturbs the intrinsic colors of galaxies (i.e., the colors we would measure in the absence of absorption and/or emission),

[8] Note that because our selection, and hence simulations, are concerned with the rest-UV colors, adopting a Maraston et al. (2006) model (where most of the difference with the model of G. Bruzual & S. Charlot [1996, private communication] is in the rest-optical) should minimally affect our results.

[9] There is considerable leeway in the best-fit star formation histories for the optical/IR SEDs of UV-selected $z \sim 2$ galaxies, but external constraints point to burst timescales of >100 Myr (Shapley et al. 2005; Erb et al. 2006c).

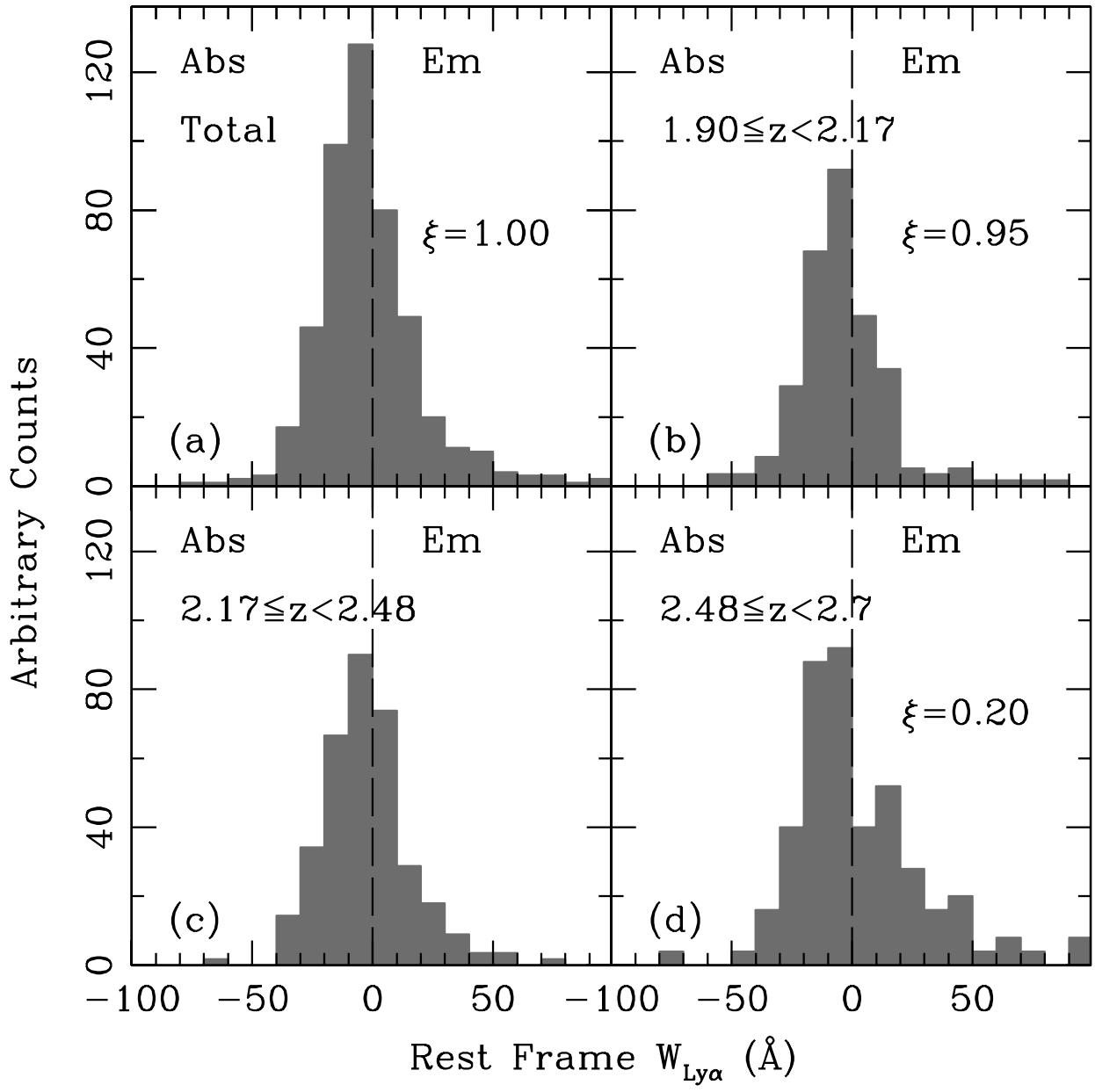

FIG. 3.—(*a*) Rest-frame Lyα equivalent width ($W_{\rm Ly\alpha}$) distribution for 482 spectroscopically observed $z \sim 2$ galaxies. (*b*)–(*d*) $W_{\rm Ly\alpha}$ distribution for subsets in redshift. We use the convention that $W_{\rm Ly\alpha} > 0$ implies emission. The distributions are absorption dominated in all cases. The ξ values indicate the probability that the distributions are drawn from the same parent population as the $W_{\rm Ly\alpha}$ distribution for galaxies at $2.17 \leq z < 2.48$, the redshift range where Lyα does not affect the rest-UV colors.

we must first determine whether the measured $W_{\rm Ly\alpha}$ distribution reflects the intrinsic distribution for the parent population of galaxies. In other words, we must check if our color selection criteria introduces significant biases into the measured $W_{\rm Ly\alpha}$ distribution. We can begin by examining some characteristics of the measured $W_{\rm Ly\alpha}$ for BX galaxies and LBGs, summarized in Table 4. The BX distribution has $\langle W_{\rm Ly\alpha} \rangle \sim -1$ Å, somewhat lower than the mean $W_{\rm Ly\alpha}$ for LBGs. While the measurements of $W_{\rm Ly\alpha}$ for *individual* galaxies may be highly uncertain, the difference in the *average* $W_{\rm Ly\alpha}$ suggests that the high-redshift (LBG) population has a higher incidence of Lyα in emission than the low-redshift (BX) population. This disparity between the lower and higher redshift populations can be better appreciated by examining column (3) of Table 4, which shows that the fraction of galaxies with $W_{\rm Ly\alpha} \geq 20$ Å ($f20$) is almost twice as high among LBGs as it is for BX galaxies.

The change in $f20$ is even more apparent when we consider BX galaxies in different redshift ranges: $f20$ for BX galaxies with redshifts between $z \approx 2.5$ and $z = 2.7$ is twice that of BX galaxies with redshifts between $z = 1.9$ and $z \approx 2.5$ (Table 4). These results suggest that star-forming galaxies exhibit a higher incidence of Lyα emission at higher redshifts, but is this trend intrinsic to high-redshift galaxies, or is it introduced as a result of color selection bias, as Figure 4 suggests?

We can test for systematics induced by the color criteria by examining $f20$ for BX galaxies at redshifts $2.17 \leq z < 2.48$, where Lyα lies outside the *U* and *G* bands. These galaxies have a similar $f20$ to that of $z < 2.17$ galaxies (Table 4), implying that the fraction of absorption versus emission line systems culled by the BX criteria is similar between the $z < 2.17$ and the $2.17 \leq z < 2.48$ samples (this assumes that there is little evolution in the $W_{\rm Ly\alpha}$ distribution between the $z < 2.17$ and $2.17 \leq z < 2.48$

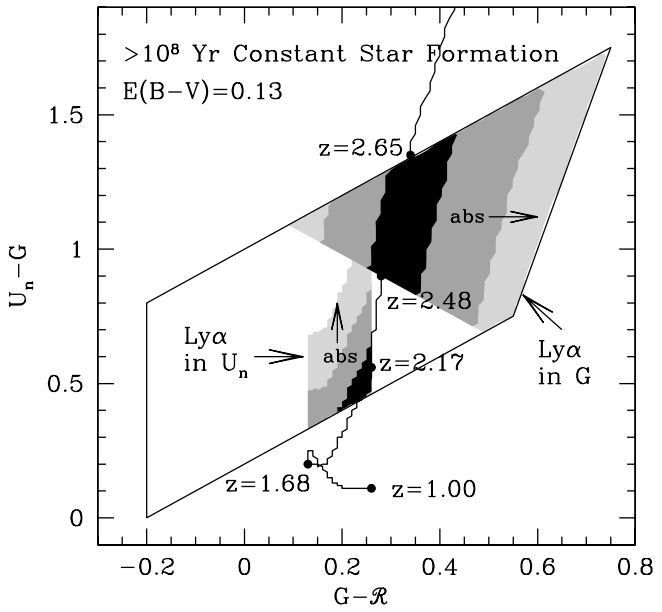

FIG. 4.—Perturbation of $U_nG\mathcal{R}$ colors from Lyα absorption and emission. The trapezoid is the BX selection window defined by eq. (1). The $U_nG\mathcal{R}$ colors of a template galaxy with constant star formation for >100 Myr (after which the UV colors are essentially constant) and $E(B-V) = 0.13$ (the mean for the $z \sim 2$ sample) assuming a Calzetti et al. (2000) extinction law is shown by the solid curve, proceeding from redshift $z = 1$ to 3. The lower and upper shaded regions correspond to redshift ranges where the Lyα line falls in the U_n and G bands, respectively. In the absence of photometric errors and assuming all galaxies can be described by the SED assumed here, galaxies with redshifts $1.68 \lesssim z \lesssim 2.17$ and $2.48 \lesssim z \lesssim 2.93$ will fall in the dark gray regions with a probability of 64% based on the $W_{\rm Ly\alpha}$ distribution in Fig. 3. The medium and light gray regions correspond to scattering probabilities of 30% and 6%, respectively. Arrows labeled "abs" indicate the direction in which the colors will be perturbed with increasing Lyα absorption.

subsamples). Focusing on the high-redshift subsample with $2.48 \leq z < 2.70$, Figure 4 suggests that these galaxies are more likely to satisfy the BX criteria if they have Lyα in absorption, yet their $f20$ is similar to that of LBGs. In other words, the $2.48 \leq z < 2.70$ subsample has an $f20$ value that does not indicate a preferential selection of absorption over emission line galaxies relative to that of the lower redshift subsamples. Rather, the $f20$ value is *larger* than those for the lower redshift subsamples and is similar to that of the LBGs. These conclusions are supported by a Kolmogorov-Smirnov test, the results of which are summarized in Figure 3. Namely, ξ in the figure indicates the probability that the $W_{\rm Ly\alpha}$ distributions for the total sample, the sample with $1.90 \leq z < 2.17$, and the sample with $2.48 \leq z < 2.70$, are drawn from the same parent population as the sample with $2.17 \leq z < 2.48$, where Lyα does not effect the $U_nG\mathcal{R}$ colors. Galaxies with $2.48 \leq z < 2.70$ have a $W_{\rm Ly\alpha}$ distribution that deviates significantly from the one at $2.17 \leq z < 2.48$.

Assuming that the UV properties of galaxies are independent of their Lyα line profiles would then suggest that the BX color criteria do not significantly modulate the intrinsic $W_{\rm Ly\alpha}$ distribution of $z \sim 2$ galaxies.[10] For the purposes of our simulations, we make the approximation that the observed $W_{\rm Ly\alpha}$ distribution for BX galaxies can be applied to our simulated galaxies to obtain the average perturbation of their rest-UV colors.

Since the Lyα line falls in the G band for galaxies in the entire redshift range $2.7 \leq z < 3.4$, we cannot examine trends in the $W_{\rm Ly\alpha}$ distribution for the LBGs in the same way we did for the BXs. However, in § 4.1 we justify why the $W_{\rm Ly\alpha}$ distribution for LBGs should approximately reflect the intrinsic $W_{\rm Ly\alpha}$ distribution for $z \sim 3$ galaxies. Also in § 4.1, the incompleteness corrections are used to test whether our initial assumptions of the $W_{\rm Ly\alpha}$ distributions are correct.

[10] Shapley et al. (2003) have demonstrated that $W_{\rm Ly\alpha}$ is in fact dependent on the rest-frame UV colors and magnitudes of galaxies. However, the small biases that these trends may have on the observed $W_{\rm Ly\alpha}$ do not have a significant impact on the derived LFs at $z \sim 2$ and $z \sim 3$.

TABLE 4
MEASURED $W_{\rm Ly\alpha}$ DISTRIBUTIONS

Sample (1)	$\langle W_{\rm Ly\alpha}\rangle$[a] (Å) (2)	$f(W_{\rm Ly\alpha}) \geq 20$ Å[b] (3)
BX (ALL: $1.90 \leq z < 2.70$).....	−1	0.12
BX ($1.90 \leq z < 2.17$).....	−1	0.08
BX ($2.17 \leq z < 2.48$).....	−2	0.11
BX ($2.48 \leq z < 2.70$).....	2	0.20
LBG ($2.70 \leq z < 3.4$)	9	0.23

[a] Mean rest-frame $W_{\rm Ly\alpha}$.
[b] Fraction with $W_{\rm Ly\alpha} \geq 20$.

3.4. *Quantifying Incompleteness*

3.4.1. *Effective Volume* ($V_{\rm eff}$) *Method*

The fraction of galaxies with a given set of binned properties that satisfy the color criteria can be computed directly from the results of the Monte Carlo simulations. These binned properties might be the optical luminosity (L), redshift (z), and reddening [$E(B-V)$] of a galaxy. Under the assumption that these properties are independent of each other, and if we let the indices i, j, and k run over the range of values of L, z, and $E(B-V)$, then the true number of galaxies in the ijkth bin can be approximated as

$$n_{ijk}^{\rm true} \simeq n_{ijk}^{\rm obs}/\bar{p}_{ijk}, \tag{3}$$

where $\bar{p}_{ijk}$ are the mean probabilities that a galaxy in the ijkth bin is (1) detected and (2) satisfies the color criteria (e.g., Adelberger 2002). These probabilities $\bar{p}_{ijk}$ are simply

$$\bar{p}_{ijk} = \frac{1}{n_{ijk}} \sum^{n} p_{ijkn}, \tag{4}$$

where p_{ijkn} is the probability that the nth simulated galaxy in the ijkth bin will be detected as a candidate, and n_{ijk} is the total number of simulated galaxies in the ijkth bin. The values p_{ijkn} take into account the probability that the colors of the nth simulated galaxy will be perturbed by the $W_{\rm Ly\alpha}$ distribution of Figure 3 and still be selected as a BX object. They also fold in the probability that a noncandidate simulated galaxy will fall in the BX selection window. Dividing by n_{ijk} normalizes the mean probabilities $\bar{p}_{ijk}$ and accounts for both the fraction of galaxies whose photometric errors scatter them out of the BX selection window and galaxies that are not detected in the simulations. If the true comoving volume corresponding to the jth bin in redshift is V_j, then the effective volume associated with the jth bin in z is

$$V_j^{\rm eff} \equiv V_j \sum^{ik} \bar{p}_{ijk} = V_j \xi_j, \tag{5}$$

where ξ_j are commonly referred to as "completeness coefficients,"

$$\xi_j \equiv \sum^{ik} \bar{p}_{ijk}. \tag{6}$$

The photometric properties of each field are unique due to differences in the observing conditions, and this will affect the computed ξ_j. We can then determine the completeness coefficients for each field and then perform a weighted average of them (i.e., weighted according to the field size) to obtain mean completeness coefficients, $\bar{\xi}_j$.

3.4.2. *Maximum Likelihood Method* ($V_{\rm lik}$)

While the procedure just described can be used to make an initial guess as to the shape of the reddening and luminosity distributions, it can lead to spurious results, particularly for objects whose true colors are such that they lie outside of or close to the edges of the BX selection window. Equation (3) is approximately true only if the average measured properties of a galaxy are the same as the true (simulated) properties, and this will certainly not be the case for galaxies that are preferentially scattered into the BX window due to photometric errors or the presence of Lyα absorption/emission (e.g., Adelberger 2002). The approach described above will also not take into account photometric bias and the preferential scattering of objects from one bin to another if the bin sizes are comparable to (or smaller than) the photometric errors (Adelberger 2002).

Figure 5 further illustrates these issues. In the simplest case, galaxies that fall within a particular bin of true properties (say, $L_0'E_0'z_0'$) will, on average, have measured properties corresponding to bin $L_0E_0z_0$. In this case, we can use the approach of § 3.4.1 (i.e., the $V_{\rm eff}$ method) to simply divide the observed number of galaxies in bin $L_0E_0z_0$ by the probability that galaxies in bin $L_0'E_0'z_0'$ will be observed in bin $L_0E_0z_0$ (call that probability $p_{0'0'0'\rightarrow 000}$), as shown by the leftmost arrow in Figure 5. However, we can point to several examples that suggest that there may not be a one-to-one correspondence between bins of intrinsic and observed properties, as illustrated by the remaining arrows in Figure 5. First, in order to accurately compute the luminosity and reddening distributions at $z \sim 2$, we cannot make our bin sizes much larger than the typical photometric errors since the observed range of $U_n - G$ and $G - \mathcal{R}$ colors for galaxies at a single redshift ($\lesssim$0.8 mag) is only $\lesssim$4 times the typical photometric error in $U_n - G$ and $G - \mathcal{R}$. Therefore, galaxies that ought to fall within a particular bin of measured properties will be scattered into adjacent bins. This would not be a problem if each bin of measured properties gained and lost an equal number of galaxies, but since the luminosity and reddening distributions are peaked, photometric errors will scatter galaxies away from the peak and into the wings of the distributions. Second, the distribution of errors in colors is not symmetric with respect to the true values such that there is a systematic tendency to scatter galaxies into redder bins more often than bluer ones (Steidel et al. 2003). Third, the presence of Lyα absorption in a galaxy's spectrum will, depending on the redshift, cause us to overestimate the reddening. Finally, there will be some galaxies whose true properties are such that on average they lie outside the selection windows, and only get scattered into the sample because of photometric errors, such as might be the case for galaxies lying close to the color selection boundaries.

Because of these systematic effects, the number of galaxies within a particular bin of measured properties will be some weighted combination of the numbers of galaxies within intrinsic bins that contribute to that measured bin of properties. The weights are simply the "transitional" or scattering probabilities indicated by the arrows in Figure 5, and these can be determined from the Monte Carlo simulations. Formally, the number of galaxies we expect to observed in a bin of measured

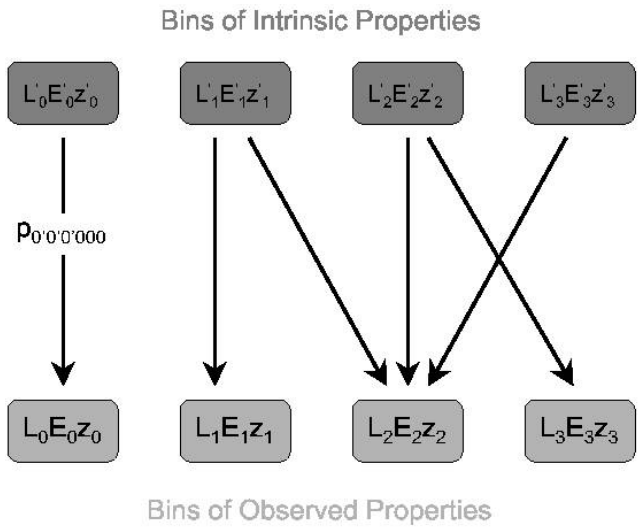

FIG. 5.—Cartoon illustration of how the probability that a galaxy with intrinsic (true) properties $L'E'z'$ may not have a one-to-one correspondence with bins of observed (measured) properties LEz (or measured colors ugr). [*See the electronic edition of the Supplement for a color version of this figure.*]

luminosity L, reddening E, and redshift z within a field of size $\Delta\Omega$ is

$$\bar{n}(L,\ E,\ z)\frac{dV}{d\Omega\, dz} = \mu \times \int dL'\, dE'\, dz' f(L')g(E')h(z') \times p_{L'E'z'\rightarrow LEz}\frac{dV}{d\Omega\, dz}, \quad (7)$$

where μ is related to the total comoving number density of galaxies; $p_{L'E'z'\rightarrow LEz}$ is the (transitional) probability that galaxies with intrinsic $L'E'z'$ will be measured to have LEz; and $f(L')$, $g(E')$, and $h(z')$ are the intrinsic distributions of luminosity, reddening, and redshift, respectively, normalized such that

$$\int_{L_{\rm min}}^{L_{\rm max}} dLf(L) = \int_{E_{\rm min}}^{E_{\rm max}} dEg(E) = \int_{z_{\rm min}}^{z_{\rm max}} dzh(z) = 1 \quad (8)$$

(Adelberger 2002). Our goal is to determine the intrinsic distributions $f(L)$, $g(E)$, and $h(z)$, but inverting equation (7) to solve for these distributions is intractable. One alternative is to compute the likelihood ($\mathcal{L}$) of observing our data, which is expressed as a list of galaxies with observed $L_iE_iz_i$, for a given set of fgh distributions,

$$\mathcal{L}(L_iE_iz_i) \propto \exp\left[-\mu\Delta\Omega \int dL\, dE\, dz \bar{n}(L,E,z)\frac{dV}{d\Omega\, dz}\right] \times \prod_i \bar{n}(L_iE_iz_i). \quad (9)$$

The discrete form of equation (9), extended to incorporate each of l different fields, can be expressed as

$$\mathcal{L}(n_{ijkl}) \propto \exp\left(-\sum_{ijkl}\bar{n}_{ijkl}\right)\prod_{ijkl}\bar{n}_{ijkl}^{n_{ijkl}}, \quad (10)$$

where $\bar{n}_{ijkl}$ is the mean number of galaxies in the ith bin of luminosity, jth bin of reddening, and kth bin of redshift in the lth field that the assumed values of f_i, g_j, and h_k imply; and n_{ijkl} is the observed number of galaxies in the same bin (e.g., Adelberger 2002). The discrete version of equation (7) is

$$\bar{n}_{ijkl} = \mu \Delta\Omega_l \sum_{i'j'k'} f_{i'} g_{j'} h_{k'} V_{k'} p_{l,i',j',k' \rightarrow ijk}, \quad (11)$$

where $\Delta\Omega_l$ is the size of the lth field, $V_{k'}$ is the comoving volume in Mpc^3 arcmin^{-2} corresponding to bin k' in redshift, and $p_{l,i',j',k' \rightarrow ijk}$ is the probability that a galaxy in the lth field in the $i'j'k'$ bin of luminosity, reddening, and redshift, will have measured properties corresponding to bin ijk. Assuming that the data quality does not vary significantly from field to field, we can simplify the probabilities such that

$$\bar{p}_{i'j'k' \rightarrow ijk} \equiv \sum_l \Delta\Omega_l p_{li'j'k' \rightarrow ijk} / \sum_l \Delta\Omega_l. \quad (12)$$

Maximizing the likelihood as expressed in equation (10) is equivalent to minimizing

$$-\ln \mathcal{L} \propto \sum_{ijk} \bar{n}_{ijk} - \sum_{ijk} n_{ijk} \ln \bar{n}_{ijk}, \quad (13)$$

and is more amenable to computation than equation (10).

3.4.3. *Implementation of the Maximum Likelihood Method*

We first used the Monte Carlo simulations to determine the transitional probabilities that relate the true luminosities, reddenings, and redshifts of galaxies to their observed rest-UV colors. Following the discussion of § 3.3, the colors of galaxies were perturbed by randomly assigning a $W_{\rm Ly\alpha}$ according to the distributions shown in Figure 3 for the BX sample and the distribution shown in Figure 8 of Shapley et al. (2003) for LBGs (see also Fig. 8). We took advantage of both the $U_n - G$ and $G - \mathcal{R}$ colors in our analysis of the $z \sim 2$ sample to provide more stringent constraints on the $E(B - V)$ distribution, something that was not possible at $z \sim 3$, where most galaxies only had limits in U_n either due to severe blanketing by the Lyα forest or the suppression of continuum flux shortward of the Lyman limit.

Figure 6 is useful in visualizing the transitional probabilities, in this case for the BX sample, where we show the relative probability distribution for galaxies between $1.0 < z < 3.0$ to be selected by the BX criteria. The probability distribution is weighted by the incidence of galaxies with intrinsic colors as determined from the LF and $E(B - V)$ distributions assumed in computing the transitional probabilities. This distribution reflects both photometric error and Lyα perturbation of the expected rest-UV colors. One noticeable feature of Figure 6 is the divergent behavior of the selection function for low- ($z \lesssim 2.0$) and high- ($z \gtrsim 2.7$) redshift galaxies, where higher redshift galaxies have redder $U_n - G$ colors for a given SED. This can be understood, in part, by examining Figure 4. If $z \sim 2$ galaxies can be reasonably described by the SED and reddening assumed above, then we would expect that galaxies with $z > 2.7$ would only be scattered into the BX window if there were large changes in their colors, either due to photometric errors or Lyα perturbation. First, we find no evidence that photometric errors increase for galaxies at higher redshifts. Second, the $(1 + z)$ dependence of the observed $W_{\rm Ly\alpha}$ will result in a larger color change (for a fixed rest-frame $W_{\rm Ly\alpha}$) for higher redshift galaxies than for lower redshift galaxies, such that the scattering probability distribution covers a larger area in color space, making it less likely for a particular source to fall within the BX selection window. Finally, the $U_n - G$ color changes more rapidly for higher redshift galaxies where Lyα forest absorption begins to increasingly affect the U_n band. All of these effects could explain the relatively small number of $z > 2.7$ galaxies singled out with the BX criteria. The advantage of rest-UV selection is that the drop-off in BX efficiency for $z > 2.7$ can be compensated for by adopting the $z \sim 3$ LBG criteria whose selection function begins to rise for $z > 2.7$ and which use exactly the same filter set, negating the need for additional observations (Steidel et al. 2003).

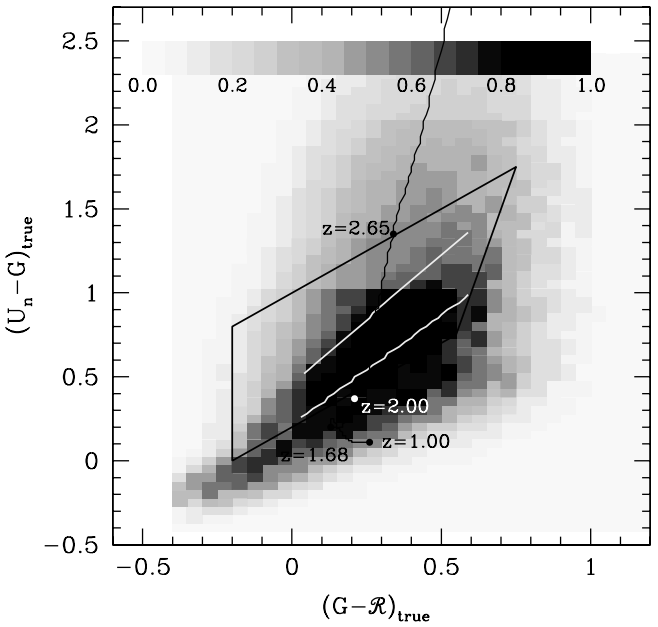

FIG. 6.—Relative probability distribution for galaxies with intrinsic colors $(U_n - G)_{\rm true}$ and $(G - \mathcal{R})_{\rm true}$ to be detected and selected as BX objects (*solid line*, same as in Fig. 4). The distribution is weighted according to the incidence of galaxies with a particular set of intrinsic colors as determined from the LF and $E(B - V)$ distributions used to compute the transformation between intrinsic and observed colors. The distribution is nonzero exterior to the BX window (*trapeezoid*) as a result of photometric error and Lyα line perturbations of the colors. Galaxies with expected (or intrinsic) $U_n - G$ colors bluer than required to satisfy BX criteria are particularly prone to selection as discussed in § 3.3. The region between the white curves denotes the swath of color space where galaxies with redshifts $2.17 < z \leq 2.48$ are expected to lie. These galaxies' colors are unaffected by Lyα line perturbations.

Unlike the $z > 2.7$ galaxies discussed above, $1.0 \lesssim z \lesssim 2.0$ galaxies are crowded into a narrower region of color space as is evident from Figure 4. Small variations in colors as a result of photometric errors or Lyα absorption can shift a large number of such galaxies into the BX selection window. This effect can be viewed in Figure 6, where there is a high relative probability for galaxies with blue $U_n - G$ colors (the "BM" galaxies; e.g., Fig. 10 of Adelberger et al. 2004) to satisfy BX selection, partly due to the effect of Lyα absorption in these systems (see Fig. 3*b*). The highest density region in this figure (between the two white curves of Fig. 6) occurs in the same color space expected to be occupied by galaxies at redshifts where the Lyα line does not affect the $U_n G\mathcal{R}$ colors ($2.17 < z \leq 2.48$). Figure 6 also demonstrates the fallacy of the assumption in equation (3), where the true and observed rest-UV colors may be significantly and, more importantly, systematically different for galaxies lying in particular regions of color space. Figure 6 is meant to be purely illustrative and, in reality (as in our simulations), the probability distribution will be "smeared" out when one considers galaxies with a range of spectral shapes.

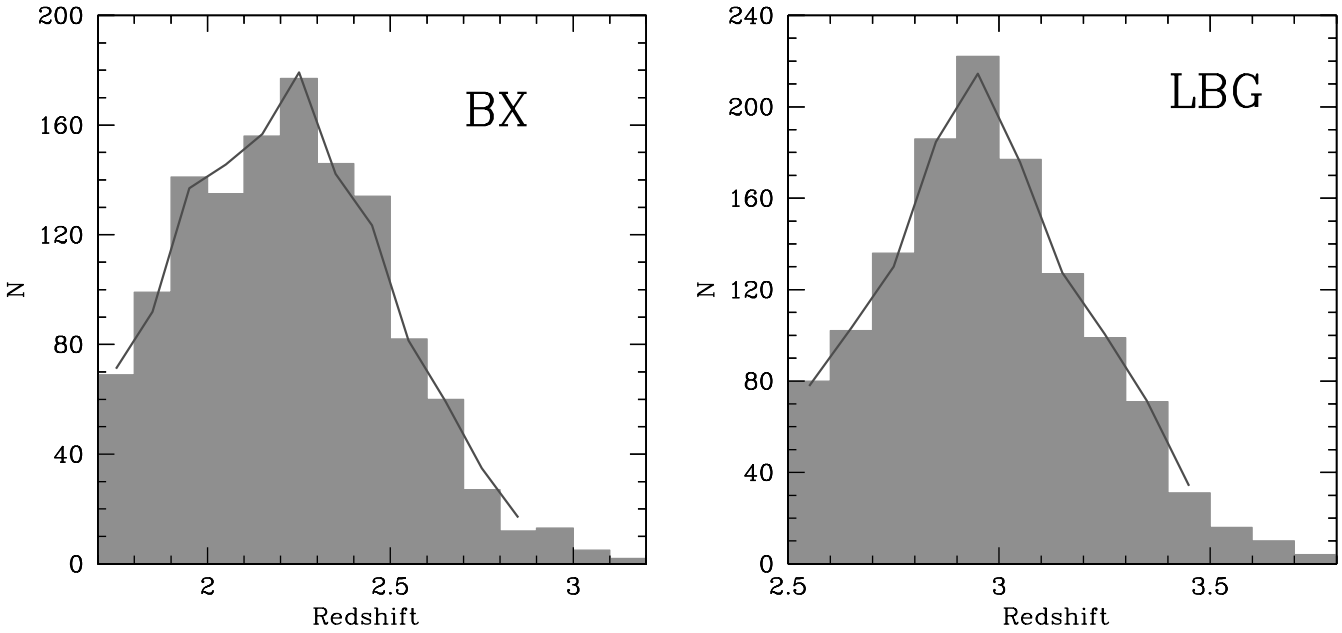

FIG. 7.—Expected redshift distributions (*lines*) given our best-fit reddening and luminosity distributions, compared with the observed redshift distributions of BX galaxies (*left*) and LBGs (*right*), indicated by the shaded histograms. [*See the electronic edition of the Supplement for a color version of this figure.*]

The effects of IGM opacity, Lyα absorption/emission, and photometric error (§§ 3.1, 3.3, and 3.2) imply that simple boxcar approximations to the redshift selection function (even in photometric surveys) are unrealistic, irrespective of the wavelengths used to select galaxies. The advantage of our combined Monte Carlo, photometric, and spectroscopic approach is that even complicated selection functions can be quantified relatively easily and thus be corrected for in the final analysis.

In practice, minimizing equation (13) while simultaneously varying the intrinsic distributions of luminosity, reddening, and redshift (*fgh*) can lead to spurious results given the large parameter space and possibility of numerous local minima in likelihood space. A reasonable approach is to then make some simplifying assumptions, such as fixing the redshift distribution to be constant and assuming an LF computed using the method of § 3.4.1. One can then minimize equation (13) with respect to the distribution of spectral shapes (g) as parameterized by the $E(B-V)$ color excess, using values of $p_{i'j'k'\rightarrow ijk}$ relevant for the spectroscopic sample. In other words, $p_{i'j'k'\rightarrow ijk}$ will give the probability that a galaxy with true properties in the $i'j'k'$th bin will be measured with properties in the ijkth bin and be spectroscopically observed. The probability that a candidate lying within a particular bin of $\mathcal{R}$ magnitude will be spectroscopically observed is approximated using the spectroscopic fractions listed in Table 2. These spectroscopic fractions are then multiplied by the probability that an object is a star-forming galaxy (i.e., not an AGN/QSO) using the AGN/QSO fractions in the relevant magnitude range (Table 2). At this stage, we must rely on the spectroscopic sample since we can only estimate $E(B-V)$ for galaxies with redshifts. Then, keeping g fixed to the best-fit $E(B-V)$ distribution, we take advantage of the full photometric sample to minimize equation (13) with respect to the luminosity distribution (f). The revised estimate of f can then be held fixed to refine our estimate of g. The process goes through several iterations where at the last stage we vary f, g, and h simultaneously. The results of this procedure indicate that our initial assumption of a constant redshift distribution (i.e., number of galaxies in each of the redshift bins is roughly constant) is a reasonable one to make. The redshift distributions predicted for BX galaxies and LBGs given the maximum likelihood *fgh* distributions are excellent matches to the observed redshift distributions of BX galaxies and LBGs, as shown in Figure 7.

Uncertainties in the luminosity and $E(B-V)$ distribution were estimated by generating many fake realizations of our observed data from the catalogs of simulated galaxies and recomputing the best-fit *fgh*. The dispersions in measurements of *fgh* are taken to be the 1 σ errors. It is important to note that the errors in our estimates are due to a combination of Poisson noise and field-to-field dispersion. Unlike all other previous estimates of the $z \sim 2$–3 UV LF, our determination incorporates the largest spectroscopic sample of galaxies at these redshifts and automatically takes into account the *systematic* effects mentioned in § 3.4.2.

4. RESULTS: INTRINSIC $W_{\rm Ly\alpha}$ AND $E(B-V)$ DISTRIBUTIONS

4.1. *Validity of Assumed $W_{\rm Ly\alpha}$ Distributions*

An important question is whether the distribution of Lyα emission and absorption profiles of galaxies changes as a function of redshift. Such trends with redshift may indicate fundamental differences in the ISM of galaxies and/or changing large-scale environments as a function of redshift. Can we do better job of determining whether the intrinsic $W_{\rm Ly\alpha}$ distribution of galaxies changes as a function of redshift? Ideally, we would have liked to include the $W_{\rm Ly\alpha}$ distribution as another free parameter in the maximum likelihood method discussed in §§ 3.3 and 3.2, so that instead of maximizing three functions (*fgh*), we would be maximizing four. However, this would needlessly complicate our ability to determine the maximum likelihood *fgh* distributions, especially since the luminosity distribution (f) is insensitive to small changes in the $W_{\rm Ly\alpha}$ distribution. As a compromise, we *can* investigate how different assumptions of the intrinsic $W_{\rm Ly\alpha}$ distributions of galaxies affect the distributions that we expect to measure.

Figure 4 illustrates how the color selection criteria can modulate the observed $W_{\rm Ly\alpha}$ distribution of galaxies, such that the observed distribution may be different than the intrinsic distribution. The Monte Carlo simulations discussed in § 3 allow us to directly compare the measured (observed) $W_{\rm Ly\alpha}$ distributions for

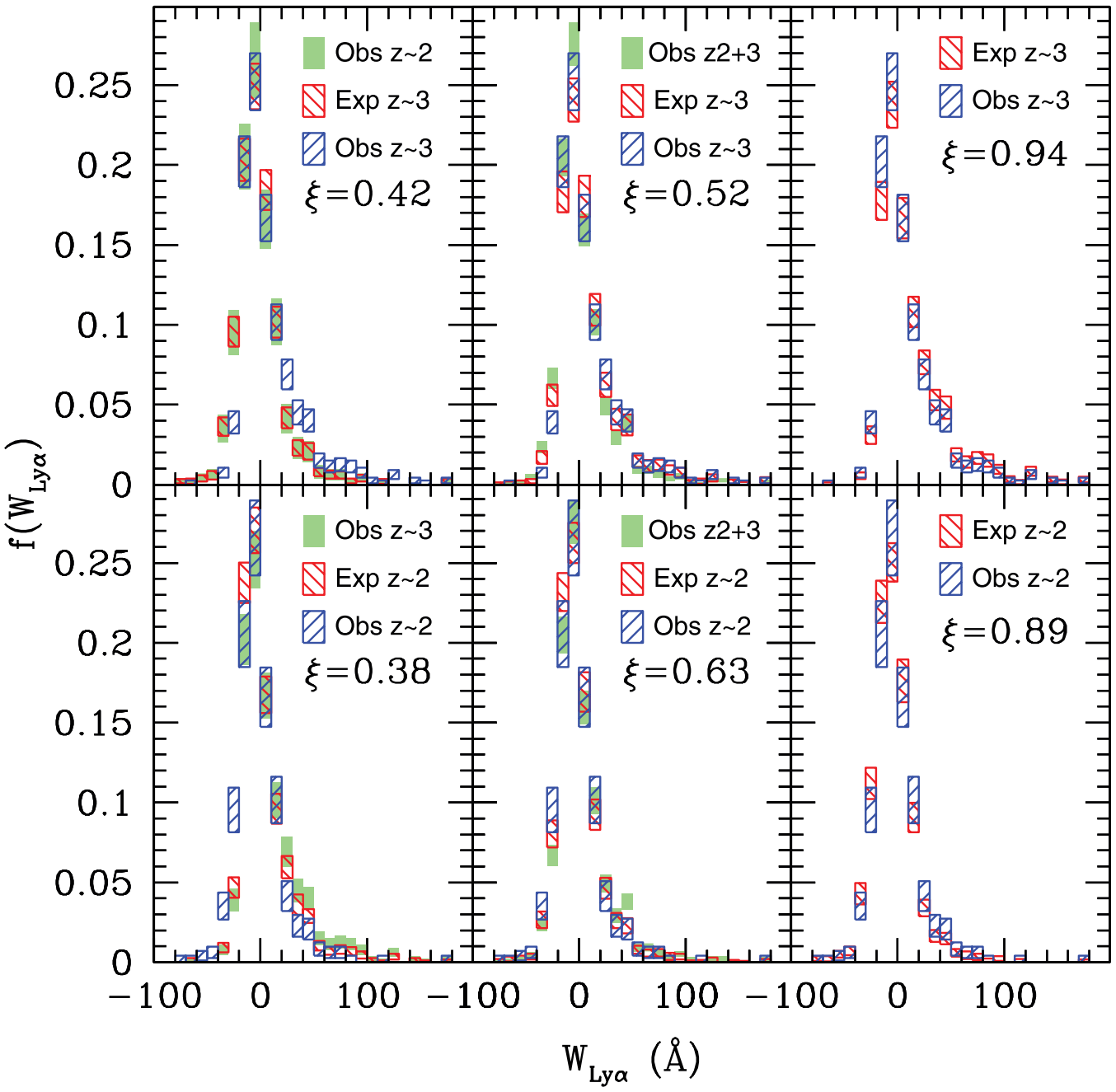

FIG. 8.—Comparisons between expected and observed $W_{\rm Ly\alpha}$ distributions for different assumptions of the intrinsic $W_{\rm Ly\alpha}$ distributions between redshifts $2.7 \leq z < 3.4$ (*top panels*) and $1.9 \leq z < 2.7$ (*bottom panels*). The assumed intrinsic distributions are denoted by green rectangles in the left and middle panels. The assumed intrinsic distributions are the same as the observed distributions (*blue rectangles*) in the right panels. The expected and observed distributions are indicated in red and blue, respectively, in all six panels. The length of the bars represent the dispersion in values of the $W_{\rm Ly\alpha}$ distribution derived assuming many realizations of the LF and $E(B-V)$ distribution (see text). The parameter ξ denotes the likelihood that the observed and expected distributions are drawn from the same distribution. We use the convention that $W_{\rm Ly\alpha} > 0$ implies Lyα emission.

the BX and LBG samples with those expected based on the transitional probabilities. The results of this comparison are summarized in Figure 8, which shows $W_{\rm Ly\alpha}$ for various assumptions of the input $W_{\rm Ly\alpha}$ distribution. We consider three cases. In the first case, we assume that the intrinsic $W_{\rm Ly\alpha}$ distribution of galaxies at $z \sim 3$ is identical to that measured at $z \sim 2$. In the second case, we assume that the intrinsic $W_{\rm Ly\alpha}$ distribution at $z \sim 3$ is an equally weighted combination of the measured distributions at $z \sim 2$ and $z \sim 3$. In the third case, we assume that the intrinsic $W_{\rm Ly\alpha}$ distribution at $z \sim 3$ is identical to the measured distribution at $z \sim 3$. Three analogous cases are considered for the $z \sim 2$ sample.

For example, the top left panel of Figure 8 shows the $W_{\rm Ly\alpha}$ distribution for $2.7 \leq z < 3.4$ galaxies that one would expect (*red rectangles*) if the *intrinsic* distribution at $2.7 \leq z < 3.4$ is identical to the measured $W_{\rm Ly\alpha}$ distribution for lower redshift ($1.9 \leq z < 2.7$) galaxies (*green rectangles*, labeled "Obs $z \sim 2$"). The validity of assuming a particular *intrinsic* distribution can be tested by comparing the expected distribution (*red rectangles*) with the actual measured distribution (*blue rectangles*). The vertical sizes of the rectangles for the observed distributions reflect Poisson errors. Uncertainties in the expected distributions (*red rectangles*) are computed by constructing many samples of galaxies drawn

randomly from the maximum likelihood luminosity and $E(B-V)$ distributions (§§ 4.2 and 5), and fixing the vertical bar size to the dispersion in the $W_{\rm Ly\alpha}$ distributions measured for each of these simulated samples.

The top left panel of Figure 8 shows that assuming an intrinsic distribution of $W_{\rm Ly\alpha}$ for galaxies at redshifts $2.7 \leq z < 3.4$ that is identical to the measured distribution of $W_{\rm Ly\alpha}$ for BX-selected ($1.9 \leq z < 2.7$) galaxies results in an expected distribution at $2.7 \leq z < 3.4$ that deviates significantly from the distribution that we actually *measured*. In this case, the expected distribution exhibits a larger fraction of galaxies with absorption and a deficit of emission-line galaxies when compared with the measured $W_{\rm Ly\alpha}$ distribution. Therefore, the intrinsic $W_{\rm Ly\alpha}$ for $2.7 \leq z < 3.4$ galaxies must have lower and higher fractions, respectively, of absorption and emission-line galaxies than what is observed among lower redshift ($1.9 \leq z < 2.7$) galaxies. The bottom left panel of Figure 8 tells a similar story. Assuming $1.9 \leq z < 2.7$ galaxies have an intrinsic $W_{\rm Ly\alpha}$ identical to that measured for LBGs ($2.7 \leq z < 3.4$) results in an expected distribution for $1.9 \leq z < 2.7$ galaxies that has a lower frequency of absorption-line systems than what is actually observed at $1.9 \leq z < 2.7$. Therefore, the intrinsic $W_{\rm Ly\alpha}$ distribution for $1.9 \leq z < 2.7$ galaxies must include a larger fraction of galaxies with Lyα in absorption than what is observed for higher redshift ($2.7 \leq z < 3.4$) galaxies.

The middle panels of Figure 8 show what happens if we assume that the intrinsic $W_{\rm Ly\alpha}$ distribution at $1.9 \leq z < 2.7$ and $2.7 \leq z < 3.4$ is simply an equally weighted combination of the distributions measured in these two redshift ranges.[11] In the bottom middle panel, the expected and observed distributions are not significantly different, so it is plausible that the intrinsic distribution of $W_{\rm Ly\alpha}$ for redshift $1.9 \leq z < 2.7$ galaxies resembles an equally weighted combination of the distributions measured for BX galaxies and LBGs. However, as the top middle panel indicates, such an intrinsic distribution overpredicts the number of galaxies at $2.7 \leq z < 3.4$ with Lyα in absorption. Decreasing the fraction of galaxies with absorption in the intrinsic distribution (e.g., by assuming some non–equally weighted combination of $W_{\rm Ly\alpha}$ distributions at low and high redshifts) may result in a better match for the observed $z \sim 3$ distribution but would lose agreement with the observed $z \sim 2$ distribution.

Finally, if we assume that the intrinsic $W_{\rm Ly\alpha}$ distributions at $1.9 \leq z < 2.7$ and $2.7 \leq z < 3.4$ are identical to those we actually measure in these two redshift ranges, then the expected distributions are very close to what is actually measured (Fig. 8, *right panels*). In fact, the expected distributions are only marginally different from the *assumed* intrinsic distributions, even if the assumptions are erroneous (compare red and green rectangles in left and middle panels of Figure 8; a Kolmogorov-Smirnov (K-S) test indicates a $\gtrsim$50% probability that the intrinsic and expected distributions are drawn from the same populations). These observations suggest that the BX and LBG color selection criteria do not alter significantly the parent $W_{\rm Ly\alpha}$ distribution of galaxies. We already discussed in § 3.3 why this must be the case for BX galaxies, since there is a redshift range covered by BX selection where the $U_nG\mathcal{R}$ colors are unaffected by Lyα; we have just shown it to be true for LBGs also.

In all cases shown in Figure 8, we have quantified the disparity in the observed and expected $W_{\rm Ly\alpha}$ distributions by computing the statistic ξ as follows. We generated 10,000 realizations of the expected $W_{\rm Ly\alpha}$ distribution (in the same way as we did to compute the uncertainties in the expected distribution; see above). We then performed a K-S test to determine the probability ($p_{\rm KS}$) that each of these realizations are drawn from the same distribution as the observed $W_{\rm Ly\alpha}$ distribution. The quantity ξ is then defined as the ratio of the number of realizations where $p_{\rm KS} < 0.5$ to the total number of realizations (10,000). Low values of ξ indicate that the expected and observed distributions are less likely to have been drawn from the same parent distribution. The values of ξ are given in each panel of Figure 8 and support our conclusion that the color criteria do not significantly alter the intrinsic $W_{\rm Ly\alpha}$ distributions. In summary, we find evidence that the fraction of emission-line galaxies ($f20$) appears to increase with redshift (Table 4) and that such a trend is most likely not due to selection bias, as demonstrated by the differences in the expected and observed $W_{\rm Ly\alpha}$ distributions for galaxies at lower and higher redshift (Fig. 8).

4.2. $E(B-V)$ Distributions

A useful by-product of the maximum likelihood method (§§ 3.4.2 and 3.4.3) is the distribution of galaxy spectral shapes, parameterized by the color excess $E(B-V)$, corrected for incompleteness. Figure 9 shows the best-fit $E(B-V)$ distributions, compared with the observed distributions, for galaxies at redshifts $1.9 \leq z < 2.7$ and $2.7 \leq z < 3.4$ (also tabulated in Table 5). Using the $V_{\rm eff}$ method (§ 3.4.1) results in $E(B-V)$ distributions that are within 10% of the observed distributions and therefore deviate significantly from our best-fit distributions at $z \sim 2$ and $z \sim 3$. The analysis indicates that the true $E(B-V)$ distributions are slightly bluer, on average, than observed. Table 5 lists the mean and dispersion of $E(B-V)$ for the observed and maximum likelihood distributions for galaxies at redshifts $1.9 \leq z < 2.7$ and $2.7 \leq z < 3.4$.

The measured $E(B-V)$ distribution for the BX sample is expected to be slightly biased toward redder spectral shapes than the intrinsic values because our photometric method makes the colors appear slightly redder than they really are—and thus $E(B-V)$ is redder—particularly for fainter galaxies (§ 3.4.2). In addition, the presence of Lyα absorption in a galaxy's spectrum will, depending on the redshift, cause the G-band magnitude to appear fainter than the true broadband magnitude (corrected for line effects), such that $E(B-V)$ will be overestimated. This latter effect can be visualized for $1.9 \leq z < 2.7$ galaxies in the left panel of Figure 9: the distribution uncorrected for the effects of Lyα (*dashed blue line*) is systematically redder than the corrected distribution (*solid red line*), owing to the presence of Lyα absorption among, and the low $f20$ value of, the majority of galaxies at $1.9 \leq z < 2.7$ (e.g., Figs. 3 and 8). The systematic effects induced by Lyα are less apparent in the $E(B-V)$ distribution for $2.7 \leq z < 3.4$ galaxies, primarily because the LBG selection window spans a region of color space that is significantly larger than the typical color change induced by Lyα perturbations.

Before proceeding with a discussion of $E(B-V)$ as an indicator of dust reddening and the variation of $E(B-V)$ with redshift and apparent magnitude, we remind the reader that we can only correct for the incompleteness of objects whose colors are such that they are scattered into the selection windows. In other words, there are undoubtedly galaxies at these redshifts that will never scatter into the BX/LBG selection windows—for example, those galaxies that are optically faint either because they have little star formation or are very dusty starbursts (e.g., DRGs and SMGs). Therefore, the $E(B-V)$ for such dusty galaxies will not be reflected in the distributions shown in Figure 9. Typically, such very dusty galaxies would have $E(B-V) > 0.45$, although a

[11] Since the comoving number densities of galaxies at redshifts $1.9 \leq z < 2.7$ and $2.7 \leq z < 3.4$ are similar, it is reasonable to approximate the combined $W_{\rm Ly\alpha}$ distribution as an equally weighted sum of the measured distributions in these two redshift ranges.

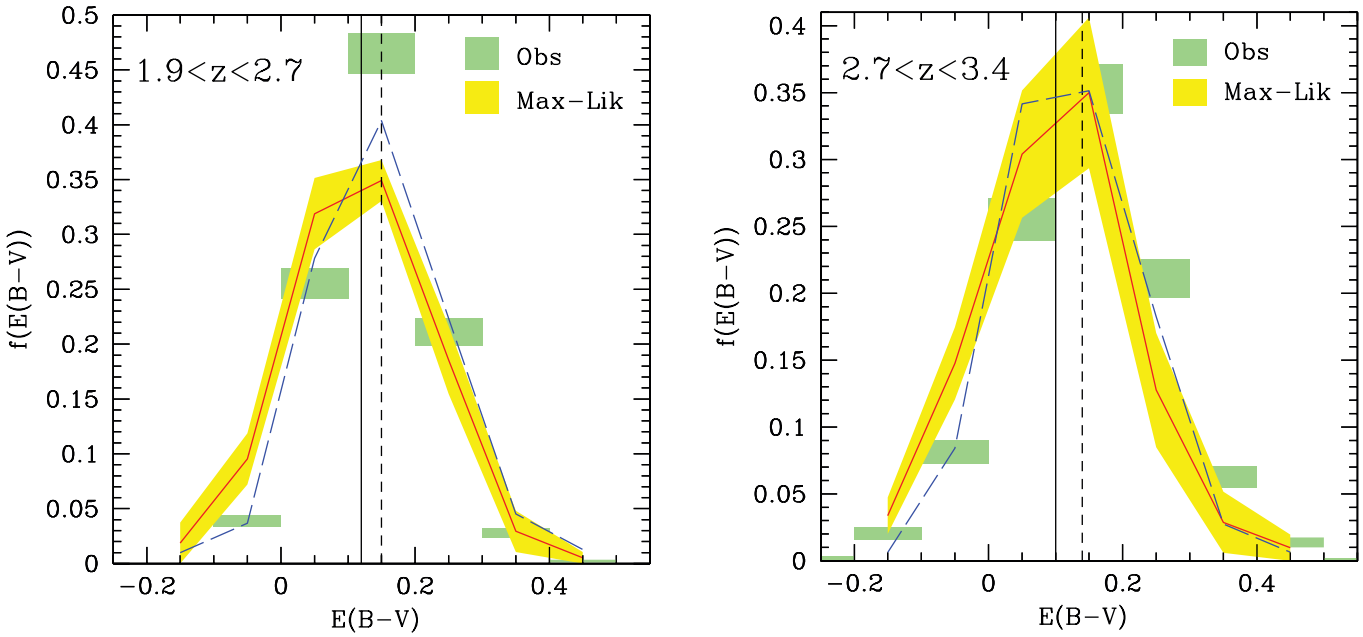

FIG. 9.—Comparison of best-fit and observed $E(B-V)$ distributions for galaxies at redshifts $1.9 \leq z < 2.7$ (*left panel*) and $2.7 \leq z < 3.4$ (*right panel*). Histograms denote the observed distributions, computed from the $G-\mathcal{R}$ colors, and assuming a constant star formation model attenuated by the Calzetti et al. (2000) law. The width of each bar reflects the Poisson error in the corresponding bin. The red lines and yellow shaded regions indicate the mean and 1 σ errors on the maximum likelihood (best-fit) distributions. The blue dashed lines indicate the distribution without correcting for Lyα perturbation to the observed colors. Dashed and solid vertical lines, respectively, denote the average $E(B-V)$ for the observed and best-fit distributions. The $E(B-V)$ distribution data are summarized in Table 5.

significant fraction also show bluer $E(B-V)$ comparable to those of BX/LBGs (Chapman et al. 2005). Because these dusty star-forming and quiescent galaxies are in large part optically faint, not accounting for them in our analysis should minimally affect our $E(B-V)$ distribution for *optically bright* galaxies (Fig. 9). Further, as we show in § 8.2, comparison of our UV LF with those derived from magnitude limits surveys suggests that we must be reasonably complete for UV-bright ($\mathcal{R} < 25.5$) galaxies at $z \sim 2$–3.

4.2.1. $E(B-V)$ as a Proxy for Dust Reddening

Up until now, we have been using $E(B-V)$ (the rest-frame UV slope) to parameterize the range of spectral shapes observed among high-redshift galaxies. A number of studies have shown that $E(B-V)$ also has a physical interpretation: it correlates very well with the reddening, or dust obscuration, of most high-redshift galaxies (e.g., Calzetti et al. 2000; Adelberger & Steidel 2000; Reddy et al. 2006b). Here we define reddening as the attenuation of luminosity by dust that can be parameterized, for example, by the quantity $L_{\rm bol}/L_{\rm UV}$. Combining *Spitzer* MIPS data for a sample of *spectroscopically confirmed* redshift $1.5 \lesssim z \lesssim 2.6$ galaxies where K-corrections could be computed accurately, Reddy et al. (2006b) showed that $E(B-V)$ not only correlates with $L_{\rm bol}$ for galaxies with $L_{\rm bol} \lesssim 10^{12.3}\ L_{\odot}$, but that the correlation is identical to that established for local galaxies (Calzetti et al. 2000; Meurer et al. 1999).

The $E(B-V)$ for relatively dust-free (or very young) galaxies is dominated by intrinsic variations in the SEDs of high-redshift galaxies, and so $E(B-V)$ is not a direct indicator of reddening for these galaxies (which is why we measure a non-negligible number density of galaxies with $E(B-V) < 0$ when assuming a single SED). Further, there is a significant presence of very dusty galaxies with $L_{\rm bol} \gtrsim 10^{12}\ L_{\odot}$ that are optically bright ($\mathcal{R} < 25.5$) and satisfy the rest-UV color criteria but have $E(B-V)$ that severely underpredict their attenuations and bolometric luminosities (Reddy et al. 2006b). Finally, we remind the reader that we cannot account for the $E(B-V)$ of objects that have a zero probability of being scattered into our sample. Nonetheless, our completeness-corrected estimates of the $E(B-V)$ distributions suggest an average attenuation between dust-corrected

TABLE 5
NORMALIZED $E(B-V)$ DISTRIBUTIONS

$E(B-V)$	BX (Measured)	$1.9 \leq z < 2.7$ (Max. Lik.)	LBG (Measured)	$2.7 \leq z < 3.4$ (Max. Lik.)
−0.2 to −0.1[a]	<0.01	0.02 ± 0.02	0.02 ± 0.01	0.03 ± 0.01
−0.1 to 0.0[a]	0.04 ± 0.01	0.10 ± 0.02	0.08 ± 0.01	0.15 ± 0.03
0.0 to 0.1	0.26 ± 0.01	0.32 ± 0.03	0.26 ± 0.02	0.30 ± 0.05
0.1 to 0.2	0.47 ± 0.02	0.34 ± 0.02	0.35 ± 0.02	0.35 ± 0.06
0.2 to 0.3	0.21 ± 0.01	0.19 ± 0.03	0.21 ± 0.01	0.13 ± 0.04
0.3 to 0.4	0.03 ± 0.01	0.03 ± 0.02	0.06 ± 0.01	0.03 ± 0.02
0.4 to 0.5	<0.01	0.01 ± 0.01	0.01 ± 0.01	0.01 ± 0.01
$\langle E(B-V) \rangle$	0.15 ± 0.07	0.12 ± 0.12	0.14 ± 0.07	0.10 ± 0.09

[a] We measure a non-negligible number of galaxies with $E(B-V) < 0$ since the $E(B-V)$ of dust-free and/or very young galaxies is dominated by intrinsic variations in the SED (see text).

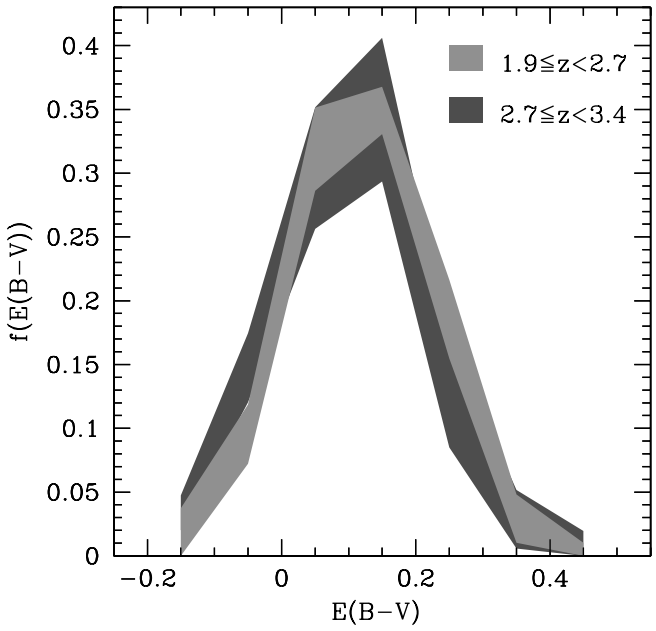

FIG. 10.—Comparison of maximum likelihood $E(B-V)$ distributions for galaxies at redshifts $1.9 \leq z < 2.7$ and $2.7 \leq z < 3.4$. [*See the electronic edition of the Supplement for a color version of this figure.*]

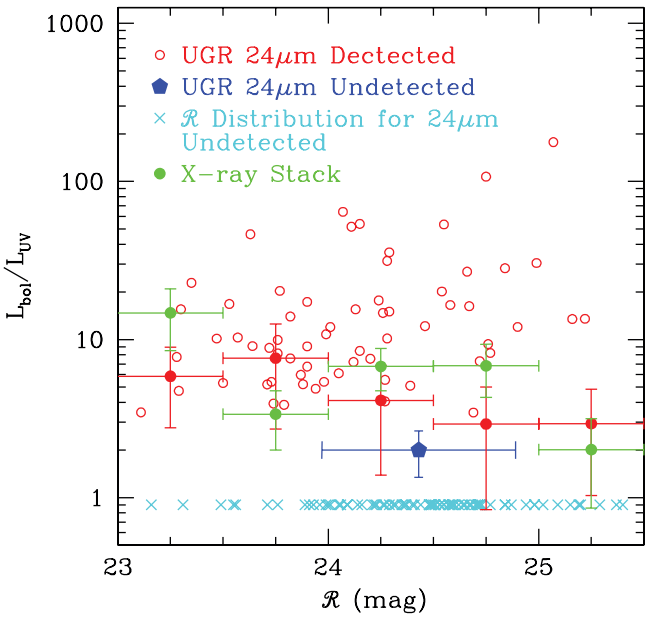

FIG. 11.—Distribution of attenuation factors, parameterized as L_{bol}/L_{UV}, as inferred from *Spitzer* MIPS data, as a function of apparent optical magnitude $\mathcal{R}$ for rest-UV–selected galaxies with redshifts $1.5 \lesssim z \lesssim 2.6$. Also indicated is the stacked average for 48 galaxies undetected at 24 μm (*large blue pentagon*) and unconfused with brighter sources; the distribution in $\mathcal{R}$ magnitude for a larger sample of 73 galaxies undetected at 24 μm is shown by the arbitrarily normalized crosses. Total stacked 24 μm and X-ray averages are indicated by the solid red circles and green points, respectively, that include all galaxies.

and uncorrected UV luminosity, L_{UV}^{cor}/L_{UV}, of ~4–5. This is similar to the value measured from (1) stacked X-ray data for BX galaxies and LBGs (Nandra et al. 2002; Reddy & Steidel 2004), and (2) MIPS luminosities and dust-corrected UV and Hα luminosities (Reddy et al. 2006b; Erb et al. 2006b). It is also the same value advocated by Steidel et al. (1999) in correcting observed UV luminosities for dust extinction among $z \sim 3$ LBGs.

4.2.2. *Comparison of Reddening Distributions with Redshift*

Remarkably, we find very little evolution in the reddening distribution between redshifts $1.9 \lesssim z \lesssim 3.4$, despite the roughly 730 Myr timespan between the mean redshifts for the low- ($\langle z \rangle = 2.30$) and high- ($\langle z \rangle = 3.05$) redshift samples, as shown in Figure 10. It is not surprising that the two distributions should span a similar range of $E(B-V)$, since the BX criteria were designed to select galaxies with a similar range of spectral properties as LBGs. Even so, the incompleteness corrections modulate two very different observed $E(B-V)$ distributions for the lower and higher redshift samples to the point where they are virtually identical. The difference in the fraction of large $W_{Ly\alpha}$ emission systems between the two samples (§ 4.1), and the possibility that such large $W_{Ly\alpha}$ emission systems could be young and relatively dust-free galaxies (§ 8), does little to modulate the overall reddening distributions since such galaxies constitute a small fraction of the overall population.

The similarity in $E(B-V)$ and dust attenuation between $z \sim 2$ and $z \sim 3$ galaxies agrees with the stacked X-ray studies of BXs and LBGs (Reddy & Steidel 2004; Nandra et al. 2002). As we discuss in § 8, the lack of evolution in $E(B-V)$ implies that the extinction properties of bright ($\mathcal{R} \leq 25.5$) star-forming galaxies are not changing significantly between redshift $z \sim 3$ and $z \sim 2$, unlike the situation at lower ($z \lesssim 2$) and higher ($z \gtrsim 3$) redshifts (e.g., Reddy et al. 2006b; Bouwens et al. 2006).

4.2.3. *Reddening Distribution as a Function of Rest-Frame UV Magnitude*

Before turning to a discussion of the LF, we must first determine whether the best-fit $E(B-V)$ distribution shows any systematic changes as a function of rest-frame UV magnitude, since such changes can, in principle, affect the shape and normalization of the LF. As a first test, we restricted the maximum likelihood analysis (§§ 3.4.2 and 3.4.3) to particular magnitudes in the range $22.0 \leq \mathcal{R} \leq 25.5$, and we did not find any significant trend in the $E(B-V)$ distribution as a function of magnitude to $\mathcal{R} = 25.5$.

Because $E(B-V)$ can be used as a proxy for the reddening of galaxies (§ 4.2.1), we have further investigated whether the reddening distribution varies as a function of observed apparent magnitude by exploiting the multiwavelength data in several survey fields. To accomplish this, we relied on our interpretation of the *Spitzer* MIPS data for a sample of BX-selected galaxies in the GOODS-N field; these data give us an independent probe of the dust emission in $z \sim 2$ galaxies. Figure 11 shows the dust obscuration factors, parameterized as L_{bol}/L_{UV}, where $L_{bol} \equiv L_{IR} + L_{UV}$ (infrared plus UV luminosity),[12] as a function of observed optical magnitude, from the MIPS analysis of the GOODS-North field by Reddy et al. (2006b). The open red circles indicate rest-UV-selected objects at $1.5 \leq z \leq 2.6$, most of which are BX galaxies, detected at 24 μm, and the large pentagon and crosses denote the average stack and distribution in $\mathcal{R}$ magnitude, respectively, for galaxies undetected at 24 μm. The total 24 μm stacked averages including both detected and undetected galaxies at 24 μm are shown by the solid red circles. Similarly, the L_{bol}/L_{UV} inferred from X-ray stacked averages (computed in manner similar to that presented in Reddy & Steidel 2004, where L_{bol} is determined from the X-ray flux) including all galaxies, irrespective of direct detection in the *Chandra* 2 Ms data (Alexander et al. 2003) are shown by the green points. While there is some evidence that the *dispersion* in attenuation factor increases toward fainter magnitudes, as

[12] Here we define L_{IR} as the total luminosity between 8 and 1000 μm.

evidenced by the larger spread of 24 μm detection galaxies and as would be expected if optically faint galaxies have contribution from both heavily dust-obscured objects as well as those with intrinsically low star formation rates, the results of Figure 11 suggest that the *average* extinction correction (based on the stacked points) is approximately constant over the range in $\mathcal{R}$ magnitude considered here.[13] These results confirm the trends noted by Adelberger & Steidel (2000), who used local templates to deduce that the observed UV luminosities of galaxies at redshifts $z = 0$, $z \sim 1$, and $z \sim 3$ are insensitive to dust obscuration, $L_{\rm bol}/L_{\rm UV}$ (e.g., Fig. 17 of Adelberger & Steidel 2000). We have confirmed this trend explicitly at redshifts $1.5 \lesssim z \lesssim 2.6$. The observed (unobscured) UV luminosity (i.e., the emergent luminosity after attenuation by dust) to $\mathcal{R} = 25.5$ will also be insensitive to bolometric luminosity since dust obscuration is tightly correlated with bolometric luminosity (Reddy et al. 2006b). While the attenuation factors and bolometric luminosities of $z \sim 2$–3 galaxies are insensitive to the *unobscured* UV luminosity, at least to $\mathcal{R} = 25.5$, there is a very strong dependence of the *dust-corrected* UV luminosity (or IR or bolometric luminosity) on the attenuation factors of galaxies (Reddy et al. 2006b; Adelberger & Steidel 2000; see also § 8.4). For the purposes of the present analysis, we will assume that the reddening distribution of galaxies is constant to $\mathcal{R} = 25.5$. We will return to the issue of how a varying reddening distribution affects our calculation of the total luminosity density in § 6.4.

5. RESULTS: UV LUMINOSITY FUNCTIONS

5.1. *Preferred LFs*

To provide the closest match between rest-frame wavelengths, and thus avoid cosmological *K*-corrections, we used $\mathcal{R}$ band as a tracer of rest-frame 1700 Å emission at the mean redshift of the LBG sample, $\langle z \rangle \sim 3.05$. Similarly, we used a "composite" magnitude between G and $\mathcal{R}$ band ($m_{G\mathcal{R}}$) as a tracer of rest-frame 1700 Å at the mean redshift of the BX sample, $\langle z \rangle \sim 2.30$, where $m_{G\mathcal{R}}$ is simply the magnitude corresponding to the average of the G and $\mathcal{R}$ fluxes. Absolute magnitudes were computed using the standard relation

$$M_{\rm AB}(1700\ \text{Å}) = m - 5\log(d_L/10\ \text{pc}) + 2.5\log(1+z), \quad (14)$$

where $M_{\rm AB}(1700$ Å) is the absolute magnitude at rest-frame 1700 Å, d_L is the luminosity distance, and m is the apparent magnitude at $\mathcal{R}$ band at $z \sim 3$ or at the composite $G\mathcal{R}$ band at $z \sim 2$. We have made the reasonable assumption that the SED *K*-correction is approximately zero for the average rest-UV SED of BX-selected galaxies after a star formation age of 100 Myr for the typical reddening [$E(B-V) \sim 0.15$] of galaxies in our sample.

The maximum likelihood rest-frame 1700 Å luminosity functions for $z \sim 2$ and $z \sim 3$ galaxies are shown in Figure 12 and listed in Table 6. The LFs were computed by using the entire photometric sample and holding the best-fit $E(B-V)$ distribution (as determined from the spectroscopic sample; Fig. 9) fixed. The extension of the spectroscopically determined $E(B-V)$ distribution to the photometric sample is a reasonable approximation given that (1) the spectroscopic and photometric samples are likely to have the same redshift distribution (§ 2.6) and (2) the $E(B-V)$ distribution remains unchanged as a function of $\mathcal{R}$ magnitude to $\mathcal{R} = 25.5$ (§ 4.2.3). By nature of the maximum likelihood method, our LF computation includes corrections for the systematic effects of photometric bias and Lyα perturbations. Errors in the luminosity functions reflect both Poisson counting statistics and field-to-field variations; the latter are accounted for by examining the dispersion in the LF as a function of magnitude for each of the fields of the survey (see § 5.4). The best-fit Schechter (1976) function and parameters for the $z \sim 2$ LF are also indicated. Uncertainties in the faint-end slope α, characteristic absolute magnitude M^* (or characteristic luminosity L^*), and characteristic number density ϕ^* are estimated by simulating many realizations of the LF as allowed by the errors (assuming the errors follow a normal distribution), fitting a Schechter function to each of these realizations, and then determining the dispersion in measured values for α, M^*, and ϕ^* for these realizations.

Based on integrating our maximum likelihood LFs, the fraction of star-forming galaxies with redshifts $1.9 \leq z < 2.7$ and $M_{\rm AB}(1700\ \text{Å}) < -19.33$ (i.e., $\mathcal{R} = 25.5$ at $z = 2.3$) that have colors that satisfy BX criteria is ≈58%. Similarly, the fraction of star-forming galaxies with redshifts $2.7 \leq z < 3.4$ and $M_{\rm AB}(1700\ \text{Å}) < -20.02$ ($\mathcal{R} = 25.5$ at $z = 3.05$) that have colors that satisfy the LBG criteria is ≈47%. Note that some galaxies escaping LBG selection will be scattered into the BX window and vice versa. Also, some galaxies that are intrinsically fainter (or brighter) than $\mathcal{R} = 25.5$ will be scattered into (or out of) the BX and LBG samples due to photometric error. The *total* fraction of galaxies with $1.9 \leq z < 3.4$ and $\mathcal{R} < 25.5$ that satisfy *either* the BX or LBG criteria is 0.55.

In the following sections, we examine various aspects of the luminosity functions derived here, including the differences in the LF derived using the $V_{\rm eff}$ versus maximum likelihood method, the significance (or lack thereof) of the Schechter parameters, and field-to-field variations. We conclude this section by examining how photometric redshifts can introduce nontrivial biases in the computation of the LF.

5.2. *Comparison of the $V_{\rm eff}$ and Maximum Likelihood Methods*

The maximum likelihood technique was used to derive the LFs presented here. However, because many published LFs are derived using the less accurate $V_{\rm eff}$ method, particularly for dropout samples at high redshift, it is useful to determine how close (or how far) such determinations are from reality by comparing with our maximum likelihood value.

Figure 13 compares the LFs at $z \sim 2$ computed using the $V_{\rm eff}$ (§ 3.4.1) and maximum likelihood (§ 3.4.2) methods, along with a comparison of the $V_{\rm eff}$ determination at $z \sim 2$ from Sawicki & Thompson (2006). The figure clearly demonstrates the systematic bias at both bright and faint magnitudes of the $V_{\rm eff}$ LF with respect to the maximum likelihood value. These biases are particularly apparent for criteria that target a narrow range in color space, such as the BX criteria, where photometric scatter or perturbations due to Lyα can be as large or larger than the width of the color selection windows (e.g., Figs. 4 and 6). For example, we would have inferred a significantly shallower faint-end slope of $\alpha = -1.21 \pm 0.15$ had we relied on the LF derived from the $V_{\rm eff}$ method.[14] For the LBG criteria, we find little difference in the $V_{\rm eff}$ and maximum likelihood determinations of the LF, mostly due to the fact that the LBG selection window covers a larger area of color space and outlier objects (with colors placing them near

[13] We note that Reddy et al. (2006b) excluded objects from their analysis that were directly detected in the *Chandra* 2 Ms data in the GOODS-N field (Alexander et al. 2003) of which almost all are AGNs.

[14] Note that our $V_{\rm eff}$ determination is slightly different from that of Sawicki & Thompson (2006) despite the use of the exact same filter set and color criteria between the two studies, since our $V_{\rm eff}$ determination includes the effects of Lyα line perturbations to the rest-UV colors and incorporates the maximum likelihood $E(B-V)$ distribution in the LF calculation.

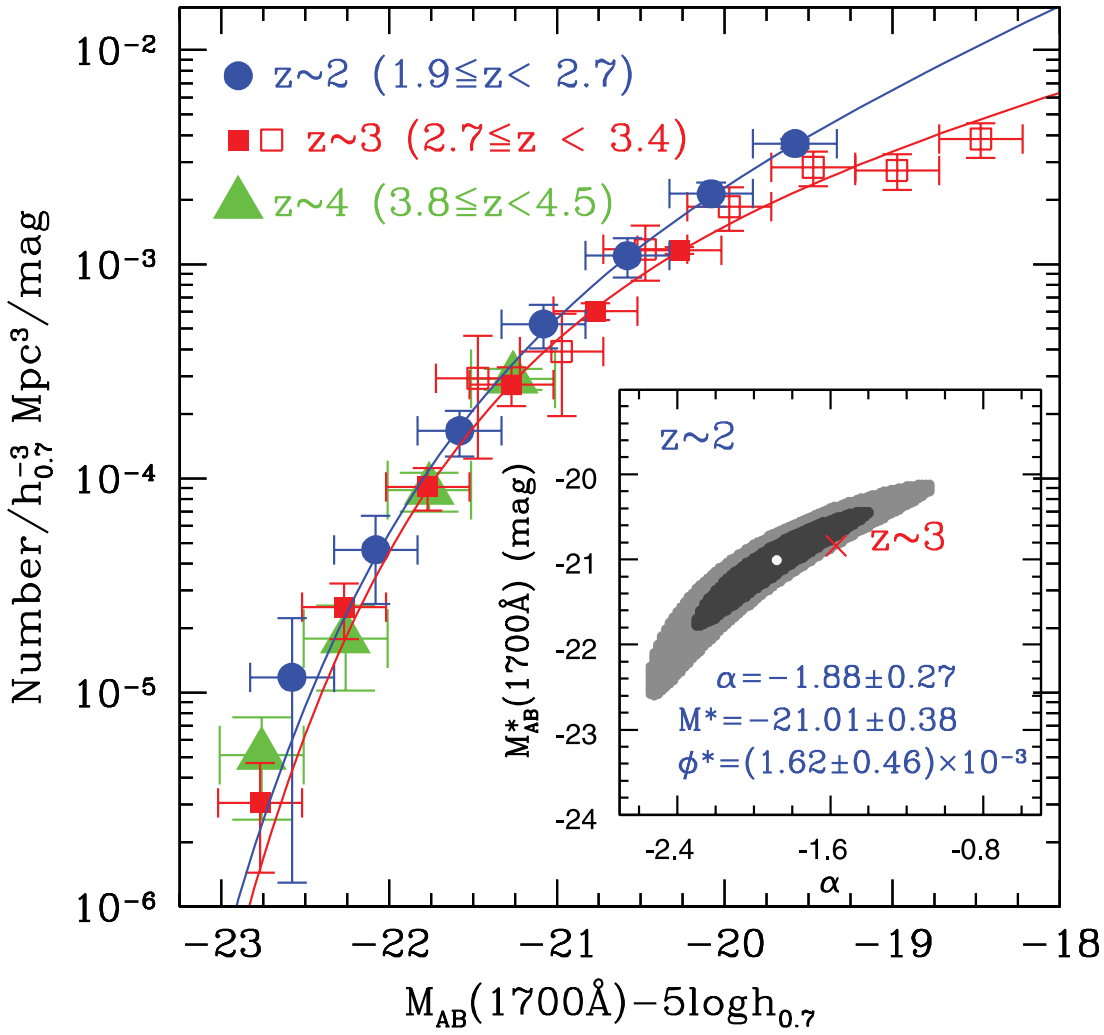

FIG. 12.—Rest-frame UV luminosity functions at $z \sim 2$ (*solid circles*) and $z \sim 3$ (*solid and open squares*, for ground-based observations and *HST*, respectively) computed in our analysis, compared with $z \sim 4$ results (*triangles*) from Steidel et al. (1999). All data have been recast to the same cosmology used throughout this paper. Also indicated are the best-fit Schechter (1976) functions for the $z \sim 2$ (*blue line*) and $z \sim 3$ (*red line*) LFs. No shift in normalization was applied to the LFs. Confidence contours demonstrate the degeneracy between α and M^* for the $z \sim 2$ fit, as shown in the inset. The red cross denotes α and M^* for $z \sim 3$ galaxies.

TABLE 6

REST-FRAME UV LUMINOSITY FUNCTIONS OF $1.9 \lesssim z \lesssim 3.4$ GALAXIES

Redshift Range	M_{AB}(1700 Å)	ϕ ($\times 10^{-3}\ h_{0.7}^3$ Mpc^{-3} mag^{-1})
$1.9 \leq z < 2.7$	−22.83 to −22.33	0.012 ± 0.01
	−22.33 to −21.83	0.05 ± 0.02
	−21.83 to −21.33	0.17 ± 0.04
	−21.33 to −20.83	0.53 ± 0.12
	−20.83 to −20.33	1.10 ± 0.23
	−20.33 to −19.83	2.13 ± 0.27
	−19.83 to −19.33	3.66 ± 0.18
$2.7 \leq z < 3.4$	−23.02 to −22.52	0.0031 ± 0.0016
	−22.52 to −22.02	0.025 ± 0.007
	−22.02 to −21.52	0.09 ± 0.02
	−21.52 to −21.02	0.27 ± 0.06
	−21.02 to −20.52	0.60 ± 0.06
	−20.52 to −20.02	1.16 ± 0.04

the selection boundaries) for which the bias is the largest will make up a significantly smaller fraction of the sample.

5.3. *Schechter Parameters*

The spectroscopic sample allows us to accurately constrain the LF, taking into account sample completeness, interloper fraction, and line perturbations, for galaxies with $\mathcal{R} < 25.5$. Above this limit we consider our LF to be most robust. The results for $z \sim 2$ galaxies fainter than $\mathcal{R} = 25.5$ is less certain given that our determination of the $z \sim 2$ faint-end slope relies on a spectroscopic sample that extends only ~4 times fainter than the characteristic luminosity of $z \sim 2$ galaxies. Formally, we find a faint-end slope at $1.9 \leq z < 2.7$ of $\alpha = -1.88 \pm 0.27$, with a characteristic magnitude of $M^* = -21.01 \pm 0.38$.

The Steidel et al. (1999) analysis of the $z \sim 3$ LF included *U*-dropout galaxies in HDF-N, where the redshift distribution was modeled using the color criteria of Dickinson (1998) and assuming the range of intrinsic spectral shapes of LBGs found by Adelberger & Steidel (2000) (Fig. 12, *open squares*). Based on the combined Keck spectroscopic and HDF-N *U*-dropout samples, Steidel et al. (1999) found a steep faint-end slope $\alpha = -1.60 \pm 0.13$. Further refinement of the incompleteness

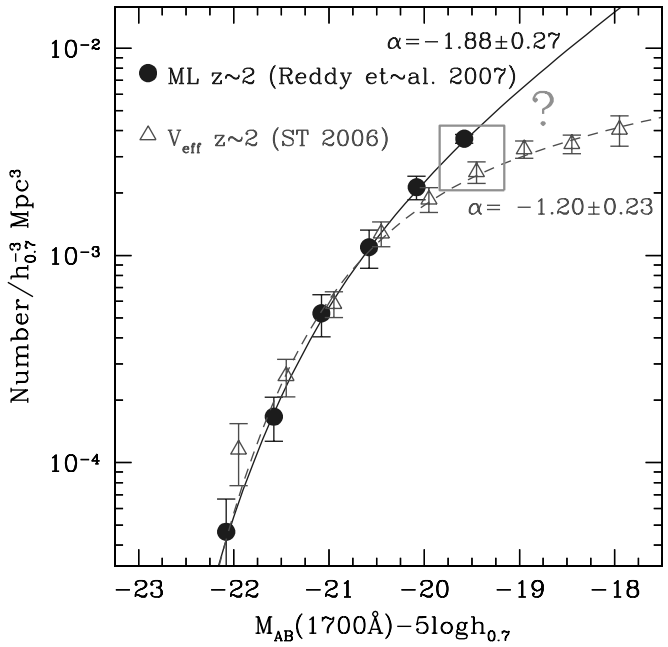

FIG. 13.—Comparison of the maximum likelihood LF at $z \sim 2$ with the $V_{\rm eff}$ determinations from our work (*open circles*) and Sawicki & Thompson (2006) (*open triangles*). [*See the electronic edition of the Supplement for a color version of this figure.*]

corrections by Adelberger & Steidel (2000) resulted in a combined fit to the ground-based spectroscopic and HDF *U*-dropout samples of $\alpha = -1.57 \pm 0.11$. Fitting only the ground-based (spectroscopically determined) points from our analysis at $z \sim 3$ yields $\alpha = -1.85 \pm 0.26$ and $M^* = -21.12 \pm 0.20$. Combining our data with the HDF-N *U*-drop points, and excluding the faintest HDF point that may suffer from incompleteness (Steidel et al. 1999), results in a fit with $\alpha = -1.57 \pm 0.11$ and $M^*_{\rm AB}(1700\ {\rm \AA}) = -20.84 \pm 0.12$. Not surprisingly, these values are in excellent agreement with those found by Adelberger & Steidel (2000) primarily because the same faint (HDF) data are used to determine the faint-end slope. The best-fit Schechter function at $z \sim 3$ is also indicated in Figure 12.

While α and M^* are useful in parameterizing the general shape of the LF, we caution against overinterpreting their validity when accounting for faint galaxies that are beyond current spectroscopic capabilities. The absence of spectroscopic constraints on the asymptotic faint-end slope and a less than exponential falloff of bright sources both conspire to make α steeper (i.e., more negative). However, these parameters are useful in describing a local approximation to data points that are not far from L^*. For convenience, the best-fit parameter values from our analysis are listed in Table 7. In the subsequent analysis, we will assume $\alpha = -1.6$ for the faint-end slope of the UV LF at $z \sim 2$–3. Note that if the steeper faint-end slopes inferred from our shallower ground-based data ($\alpha \sim -1.88$) accurately reflect reality, then this will serve to increase the total UV luminosity density of galaxies with SFRs between 0.1 and 1000 $M_\odot$ yr^{-1} by ∼20% and ∼50% at $z \sim 2$ and $z \sim 3$, respectively, relative to the values obtained with $\alpha = -1.6$.

5.4. *Field-to-Field Variations*

Access to multiple uncorrelated fields allows us to judge the effects of large-scale structure on the derived LF. The dispersion in normalization between the luminosity function in bins of $\mathcal{R}$ derived in individual fields is a strong function of $\mathcal{R}$, as illustrated in Figure 14 for the $z \sim 2$ sample. The points in this figure are determined using the following steps. First, we computed the maximum likelihood LF in each of the 14 fields of the $z \sim 2$ survey. The dispersion in LF values from field to field, within a given magnitude bin, are determined by weighting the LF values by the field size such that LF determinations from larger fields are given more weight than LF determinations from smaller fields. The fractional dispersion in normalization is then defined as the ratio of the dispersion of these weighted values and the weighted mean value of the LF in each bin. This fractional dispersion in normalization is much larger at the bright end for $\mathcal{R} < 22.5$ and decreases significantly for galaxies with fainter magnitudes. This trend results from statistical fluctuations at the bright end due to the smaller number of galaxies and the fact that the clustering correlation function is a strong function of magnitude (Adelberger et al. 2005a). We further note that at least 4 of the 14 $z \sim 2$ survey fields show significant redshift-space overdensities (e.g., HS1700 field; Steidel et al. 2005). The effect of such overdensities on the derived LF will of course depend on the redshift of the overdensities with respect to the BX selection function. An overdensity at $z = 2.8$ is unlikely to affect the LF derived for $1.9 \leq z < 2.7$ galaxies to the same extent as an overdensity at $z = 2.3$ (placing it in the middle of the BX selection function). One option when working in single fields is to use the available spectroscopy and known selection function to model the effects of such overdensities on the derived LFs, or to use Monte Carlo simulations to estimate uncertainties in the normalization of the derived LF (Bouwens et al. 2006). Because our analysis includes many uncorrelated fields (14 and 29 for the $z \sim 2$ and $z \sim 3$ samples, respectively) spread throughout the sky, we assume that the average LFs are representative of $1.9 \lesssim z \lesssim 3.4$ galaxies. Any remaining uncertainty in normalization of the average LF (i.e., the uncertainty reflected in the field-to-field fractional dispersion shown in Fig. 14) is added in quadrature with Poisson counting error (shown as open circles in Fig. 14) to determine the total error bars shown in Figure 12. We remind the reader that the *systematic* effects of photometric bias and Lyα perturbations are already reflected in the derived LFs.

5.5. *Effect of Photometric Redshifts*

In light of recent literature regarding photometric estimates of the UV LFs at redshifts $z \sim 2$–3 (e.g., Gabasch et al. 2004), it is worthwhile to briefly examine how our derived LFs would

TABLE 7
BEST-FIT SCHECHTER PARAMETERS FOR UV LFS OF $1.9 \lesssim z \lesssim 3.4$ GALAXIES

Redshift Range	α	$M^*_{\rm AB}(1700\ {\rm \AA})$	ϕ^*	χ^2
$1.9 \leq z < 2.7$ (ground-based)	-1.88 ± 0.27	-21.01 ± 0.38	$(1.62 \pm 0.46) \times 10^{-3}$	0.40
$1.9 \leq z < 2.7$ (ground-based)	-1.60 (fixed)	-20.60 ± 0.08	$(3.31 \pm 0.22) \times 10^{-3}$	5.81
$2.7 \leq z < 3.4$ (ground-based)	-1.85 ± 0.26	-21.12 ± 0.20	$(1.12 \pm 0.52) \times 10^{-3}$	0.11
$2.7 \leq z < 3.4$ (ground + space)	-1.57 ± 0.11	-20.84 ± 0.12	$(1.66 \pm 0.63) \times 10^{-3}$	5.72

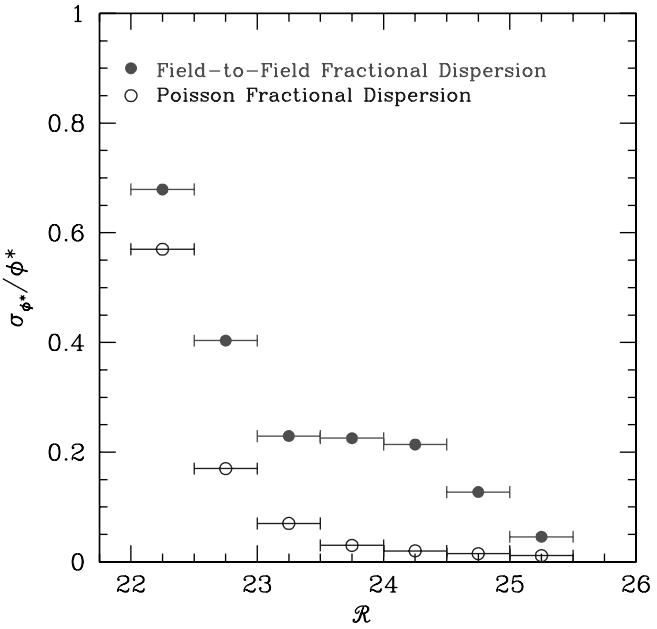

FIG. 14.—Fractional dispersion in normalization of the $z \sim 2$ UV LF as a function of apparent magnitude, both in terms of field-to-field (*solid circles*) and Poisson (*open circles*) variations. [*See the electronic edition of the Supplement for a color version of this figure.*]

change in the absence of spectroscopic information, instead relying on photometric redshifts ($z_{\rm phot}$). We derived the photometric redshift error, defined as

$$\Delta z \equiv z_{\rm phot} - z_{\rm spec}, \tag{15}$$

for a sample of 925 star-forming galaxies with spectroscopic redshifts $1.4 < z_{\rm spec} < 3.5$ that lie in fields with sufficient multiwavelength data to warrant SED analysis. This is by far the largest spectroscopic sample at these redshifts, and it enables us to investigate how Δz varies as a function of both redshift and magnitude since, in principle, the error will depend both on the relative placement of spectral breaks across the photometric filters (i.e., the redshift of the galaxy) and on the quality of the photometry and significance of the detection (i.e., the apparent magnitude of the galaxy).

Photometric redshifts were estimated using the HyperZ code of Bolzonella et al. (2000). We only considered galaxies with detections in at least the following bands: G, $\mathcal{R}$, and K_s. At least half of the resulting 925 objects also have detections in either the J band and/or *Spitzer* IRAC bands. All but 52 of the 925 objects are detected at U_n; the remaining 52 are all "C" candidates (§ 2.3) at redshifts $z > 2.7$. We considered a variety of star formation histories, reddening, and redshifts when fitting the data using HyperZ. Figure 15 compares the photometric and spectroscopic redshifts for the sample of 925 galaxies. The biases and dispersions in photometric redshifts for galaxies fainter and brighter than $M^* = -21.01$ in different redshift ranges are listed in Table 8, both including and excluding catastrophic outliers with $z_{\rm phot} < 0.6$. Even excluding outliers with $z_{\rm phot} < 0.6$ results in significant redshift error dispersions of $\sigma(\Delta z) \sim 0.33$–$0.42$. Furthermore, in all cases over the redshift ranges where we compute the LFs, $1.9 \leq z < 2.7$ and $2.7 \leq z < 3.4$, we find significant photometric biases ranging from $\Delta z \sim 0.2$–0.5, in the sense that $z_{\rm phot}$ is systematically underestimated (i.e., luminosity is overestimated).

A simulation was constructed to examine the effect of these biases and dispersions on the LF, similar to the method presented in Marchesini et al. (2007) but modified to (1) allow for many realizations of the intrinsic LF and (2) account for photometric redshift errors using the empirical data of Figure 15 and Table 8. To accomplish this, we first generated many realizations of the UV LF as allowed by the (normally distributed) errors of the spectroscopically determined LF. We then drew magnitudes randomly from a Schechter distribution determined by fitting a Schechter

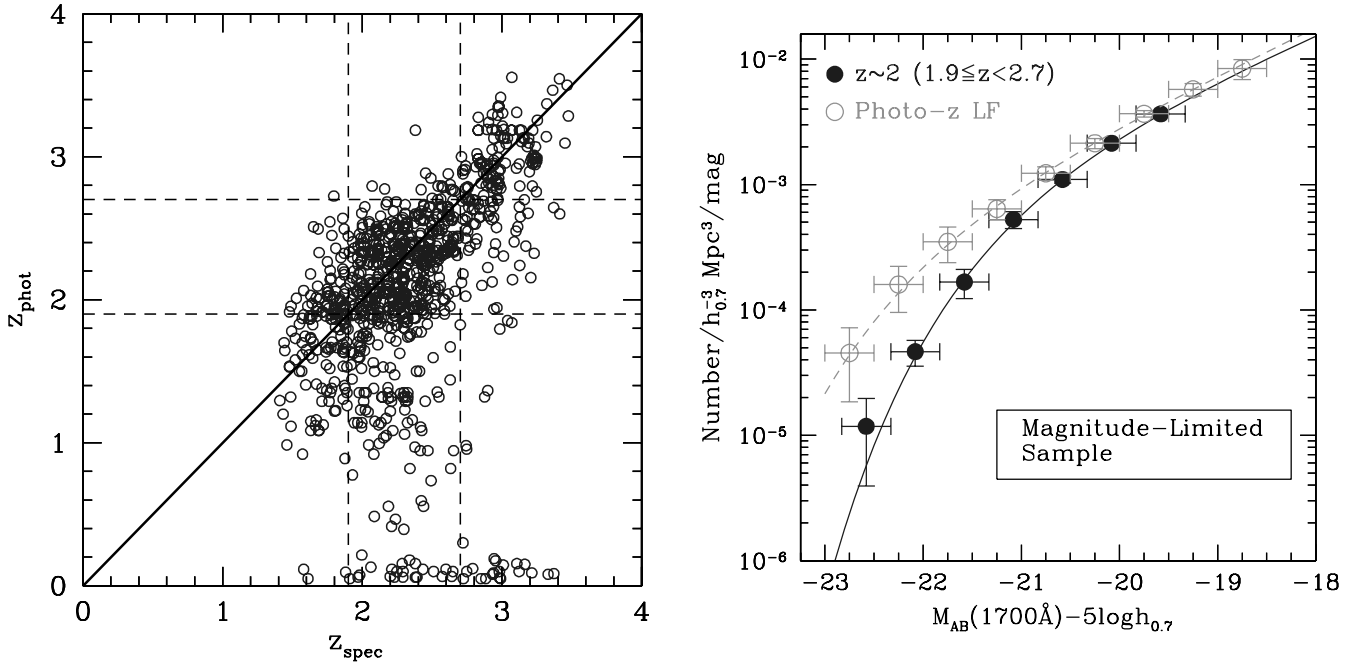

FIG. 15.—(*Left*:) Comparison between the photometric redshifts derived using HyperZ (Bolzonella et al. 2000) and spectroscopic redshifts from our ground-based survey for a sample of 925 star-forming galaxies. The solid line denotes the unity relationship, and dashed lines demarcate the region over which the UV LF is computed. (*Right*:) Comparison of the UV LF derived using the photometric redshift distribution in the left panel (*open circles*) with our spectroscopic determination (*solid circles*). [*See the electronic edition of the Supplement for a color version of this figure.*]

TABLE 8
BIASES AND DISPERSIONS IN PHOTOMETRIC REDSHIFT ERRORS ($\Delta z = z_{\rm phot} - z_{\rm spec}$) FOR STAR-FORMING GALAXIES AT $1.4 \leq z \leq 3.5$

Redshift Range	All Galaxies $M > -21.01$, $M \leq -21.01$	Excluding $z_{\rm phot} \leq 0.6$ Galaxies $M > -21.01$, $M \leq -21.01$
$1.4 \leq z < 1.9$	0.01 ± 0.40, 0.07 ± 0.48	0.04 ± 0.35, 0.07 ± 0.33
$1.9 \leq z < 2.7$	-0.26 ± 0.58, -0.28 ± 0.62	-0.18 ± 0.42, -0.14 ± 0.40
$2.7 \leq z < 3.5$	-0.50 ± 0.93, -0.43 ± 0.86	-0.20 ± 0.42, -0.21 ± 0.39

NOTE.—Here $\Delta z \equiv z_{\rm phot} - z_{\rm spec}$.

function to each of these realizations of the intrinsic LF. Since the probability of a galaxy lying at redshift z,

$$p(z) \propto \frac{dV}{dz} \propto \frac{d_L^2(z)}{(1+z)^2} \frac{1}{\sqrt{\Omega_\Lambda + \Omega_M (1+z)^3}}, \qquad (16)$$

is roughly constant over the redshift interval $1.4 \leq z \leq 3.5$, we drew redshifts from a uniform distribution. The result is a list of simulated redshift and magnitude pairs, ($z_{\rm spec}$, M), for galaxies. A photometric redshift was assigned to each galaxy by randomly drawing a redshift from the distribution of $z_{\rm phot}$ (in Fig. 15, *left panel*) within a box of width $\delta z_{\rm spec} = 0.4$ centered at $z_{\rm spec}$, using the $z_{\rm phot}$ distribution for galaxies either brighter or fainter than $M^* = -21.01$ depending on the magnitude M of the simulated galaxy. The absolute magnitude of the galaxy was then recomputed assuming the photometric redshift. We then reconstructed the LF at $1.9 \leq z < 2.7$ for each realization assuming the photometric redshifts. The average LF from these many realizations is indicated by the open circles in the right panel of Figure 15. Because there are more galaxies scattered into, rather than out of, the redshift range $1.9 \leq z < 2.7$, the net result is that we would have overestimated the intrinsic LF had we relied on photometric redshifts. While the difference in the photometric and spectroscopic LFs on the faint end is small, it becomes quite significant for galaxies brighter than M^*. This systematic difference arises from the fact that the change in absolute magnitude (ΔM) for a fixed Δz and apparent magnitude will be larger for galaxies scattered from low to high redshift than for galaxies scattered from high to low redshift. For example, a galaxy at redshift $z_{\rm spec} = 1.6$ scattering to redshift $z_{\rm phot} = 2.0$, implying $|\Delta z| = 0.4$, results in $\Delta M \approx 0.44$. However, a galaxy at redshift $z_{\rm spec} = 3.0$ scattering to redshift $z_{\rm phot} = 2.6$ (i.e., the same $|\Delta z|$ as above) results in $\Delta M \approx 0.26$. The net effect is that the bright end of the LF is systematically inflated with respect to the faint end.

There are three further issues to note. First, it has become common in the literature to estimate photometric redshift errors independent of fitting the stellar populations of galaxies by simply shifting prescribed fixed templates until a best-fit redshift is reached. Redshift errors derived in this manner will underestimate the true error in redshift obtained by marginalizing over the uncertainties of fitting those templates to the broadband photometry. Second, the simulation performed here benefited from the a priori knowledge that all the galaxies truly lie at the correct redshifts $1.9 \leq z < 2.7$. Photometric redshift scatter (e.g., Fig. 15) will generally be larger than that presented here since there will undoubtedly be some very low-redshift galaxies ($z < 1.4$) that are scattered into the range $1.9 \leq z < 2.7$. Third, we remind the reader that the photometric redshift errors derived here are for optically bright ($\mathcal{R} < 25.5$) objects with spectroscopic redshifts. It is likely that the photometric redshift errors will be larger than assumed here for very faint galaxies where the photometric uncertainties may be larger. This, in turn, may bias the faint-end slope more severely than reflected in our simulations. We stress that the results of the photometric redshift simulation presented here (Fig. 15) are *unique* to our sample. As a result, the biases in the LF may be different for surveys that incorporate a different number of photometric filters with differing photometric data quality, although the photometric redshift accuracy found here is similar to that presented in Shapley et al. (2005) and Reddy et al. (2006b) using more (different) bands. In any case, this section illustrates how photometric redshifts can induce nontrivial biases in the LF.

5.6. *UV LF Summary*

To summarize, this section has focused on our measurements of the UV LF at $z \sim 2$ and $z \sim 3$. Our method for computing the LFs takes into account a number of systematic effects including contamination from low-redshift interlopers and AGNs, Lyα line perturbations to the observed colors of galaxies, and photometric scatter. A large number of independent fields allows us to control for sample variance. Further, spectroscopic redshifts enable us to precisely correct for the effect of IGM opacity on the rest-UV colors. Our method for computing the LFs uses a maximum likelihood technique to account for the systematic scattering of galaxies in parameter (e.g., luminosity, reddening, and redshift) space. Given this detailed treatment, we consider the UV LF at $z \sim 2$ and $z \sim 3$ derived here to be the most robust measurements yet. Comparison of our UV LF with the (corrected) determination from a magnitude limited sample suggests that our determination must be reasonably complete for galaxies with $\mathcal{R} < 25.5$ (see § 8.2).

In the following sections, we will discuss how we can combine our determinations of the UV LFs at $z \sim 2$–3 with what we know about the extinction properties of high-redshift galaxies to infer LFs at other wavelengths. We will primarily focus on inferences of the IR and bolometric LFs at $z \sim 2$–3, but also present Hα LFs at similar redshifts, the latter of which may be useful for current and future emission line studies.

6. RESULTS: REST-FRAME 8 μm, INFRARED, AND BOLOMETRIC LUMINOSITY FUNCTIONS

As suggested in the previous analysis, correcting the rest-UV LF for the effects of dust extinction is a key component in recovering the star formation rate density. Aside from our knowledge of the $E(B-V)$ distribution at high redshift (§ 4.2), extensive multiwavelength data enable us to independently determine the extinction corrections relevant for the same sample of spectroscopically confirmed galaxies that we used to compute the UV LF.

Before the advent of panchromatic galaxy surveys, it was common to simply apply an average correction for extinction, typically a factor of 4–5 (Steidel et al. 1999). Subsequently, extensive multiwavelength data have placed our extinction corrections on a much more solid footing. For instance, initial X-ray and radio

stacking analyses (e.g., Nandra et al. 2002; Reddy & Steidel 2004) indicated that high-redshift UV-selected populations with $\mathcal{R} < 25.5$ have average obscuration factors ($L_{\rm IR}/L_{\rm UV}$) around 4–5, supporting the average correction advocated by Steidel et al. (1999). Further progress was made by taking advantage of the unique sensitivity of the *Spitzer* MIPS instrument, allowing us to directly detect for the first time the dust emission from L^* galaxies at $z \gtrsim 1.5$ (Reddy et al. 2006b). The Reddy et al. (2006b) analysis confirmed the *average* trends established by previous X-ray stacking studies and further demonstrated that moderate luminosity galaxies ($10^{11}\ L_\odot \lesssim L_{\rm bol} \lesssim 10^{12.3}\ L_\odot$) at $z \sim 2$ follow the Meurer et al. (1999) attenuation law found for local UV-selected starburst galaxies. The importance of this analysis for the present study is that we can directly relate the $E(B-V)$ distribution of most $z \sim 2$ galaxies (§ 4.2) with their distribution in obscuration, $L_{\rm IR}/L_{\rm UV}$.

In this section, we present our constraints on the 8 μm, infrared, and bolometric luminosity functions of $z \sim 2$–3 galaxies, as derived from our UV LFs and the known extinction properties of galaxies at these redshifts. We present IR LFs based on two different recipes [our $E(B-V)$ distribution and the distribution of 24 μm fluxes] for evaluating the dust attenuation of galaxies. In § 6.1, we combine our UV LF with the $E(B-V)$ distribution to infer the IR LF. In subsequent sections, we combine our UV LF with the observed 24 μm properties of galaxies to infer the IR LF. The two methods are compared in detail in § 6.4.

6.1. *Extinction-corrected Measures of the Luminosity Function*

As a first step, we can use the Meurer et al. (1999) relation to recover the dust-corrected LF. The method proceeded with the following steps:

1. We first generated many realizations of the maximum likelihood UV LF and $E(B-V)$ distribution at $z \sim 2$, assuming normal LF and $E(B-V)$ distribution errors. We randomly chose an LF and $E(B-V)$ distribution from these many realizations to create an LF/$E(B-V)$ pair, $\{\mathcal{L},\ \mathcal{E}\}$.

2. Because the LF and $E(B-V)$ distributions do not change significantly over the redshift range $1.9 \leq z < 2.7$ and because the $E(B-V)$ distribution is insensitive to absolute magnitude down to our spectroscopic limit (§ 4.2.3), we can assume that the *intrinsic* redshift z, magnitude M, and reddening $E(B-V)$ of a galaxy are independent variables. Redshifts were drawn randomly from a uniform distribution. Magnitudes were drawn from the range $-23 \lesssim M(1700\ \text{Å}) \lesssim -15.5$ according to a Schechter distribution that described the luminosity function $\mathcal{L}$ from the $\{\mathcal{L},\ \mathcal{E}\}$ pair. The faint limit of $M(1700\ \text{Å}) = -15.5$ corresponds to an unobscured SFR of $\sim 0.1\ M_\odot\ \text{yr}^{-1}$ using the Kennicutt (1998) calibration. We drew galaxies down to this low limit of unobscured luminosity because such galaxies can be scattered to bins of higher luminosity after correcting for extinction. Similarly, $E(B-V)$ values were drawn randomly from the $E(B-V)$ distribution $\mathcal{E}$ from the $\{\mathcal{L},\ \mathcal{E}\}$ pair, excluding negative $E(B-V)$ values that reflect unphysical reddening values. The result is a list of galaxies associated with a triplet [z, M, $E(B-V)$].

3. The rest-frame 1700 Å specific luminosity of each galaxy is calculated as

$$L_{1700} = \frac{4\pi d_L^2}{(1+z)}\, 10^{-0.4(48.60+m_{1700})}, \qquad (17)$$

where d_L is the luminosity distance at redshift z and m_{1700} is the apparent magnitude of the galaxy with absolute magnitude M at redshift z (eq. [14]). We then calculate νL_ν at 1700 Å to yield the UV luminosity. The $E(B-V)$ for the galaxy is used in conjunction with the Calzetti et al. (2000) relation to derive the dust-corrected UV luminosity.

4. To determine the IR luminosity corresponding to this dust-corrected UV luminosity, we assumed that the UV and IR emission are tied directly to the SFR of the galaxy. The IR luminosity is assumed to be the luminosity, which, when added to the unobscured UV luminosity, yields the same SFR that would have been obtained from the dust-corrected UV luminosity, assuming the Kennicutt (1998) relations. These IR luminosities are then perturbed by a normal distribution with σ of 0.3 dex to account for the dispersion between dust-corrected UV and IR luminosity (or, alternatively, the dispersion between $E(B-V)$ and IR luminosity; e.g., Meurer et al. 1999).

5. These IR luminosities are then binned to produce an IR LF. This is the IR LF corresponding to the $\{\mathcal{L},\ \mathcal{E}\}$ pair selected in step 1.

Steps 1–5 are repeated many times, each time randomly drawing different $\{\mathcal{L},\ \mathcal{E}\}$ pairs. Aside from uncertainties in the rest-frame UV faint-end slope, there are two other systematics that can bias our determination of the IR LF: (1) a change in the faint-end slope of the rest-frame UV LF and (2) a change in the attenuation of UV-faint galaxies. We now discuss these two systematic effects in detail.

First, we must determine how changing the number density of such faint objects, determined by the faint-end slope α, affects the IR LF. In principle, we could simply fix $\alpha = -1.6$ when fitting the different realizations of the UV LF at $z \sim 2$ and compare with the results obtained by allowing α to vary freely in the Schechter fits to the realizations. However, this method will cause us to underestimate the errors on the faint end of the IR LF. To obtain a truer estimate at the faint end, we allowed α to vary freely around a normal distribution with a mean of $\langle\alpha\rangle = -1.6$ and standard deviation of $\sigma(\alpha) = 0.11$, similar to the dispersion in α that we measure when fitting the UV LF (Fig. 12 and Table 7). For simplicity, we assume that α varies according to $\langle\alpha\rangle = -1.6 \pm 0.11$ at $z \sim 2$ in the subsequent discussion.

A second systematic effect that can bias the determination of the IR LF is the distribution of extinction among $\mathcal{R} > 25.5$ galaxies. For the calculation of the IR LF from $E(B-V)$ we considered two cases. In the first case, we assume that the $E(B-V)$ distribution is constant to arbitrarily faint rest-UV magnitudes. In the second case, we assume that the $E(B-V)$ distribution is constant to $\mathcal{R} = 25.5$ (e.g., Fig. 11 and § 4.2.3), but then suddenly changes to have a mean $\langle E(B-V)\rangle = 0.04$ (with same dispersion) for galaxies fainter than $\mathcal{R} = 25.5$ [we refer to this second case as a discontinuous $E(B-V)$ distribution]. We have assumed this value of $E(B-V) = 0.04$ because it is similar to the $E(B-V)$ observed for very faint ($\lesssim 0.1\ L^*$) UV-selected galaxies inferred from dropout samples at higher redshifts (Bouwens et al. 2007). Because $\mathcal{R} = 25.5$ is an arbitrary limit dictated by efficient spectroscopic follow-up, it is highly unlikely that the $E(B-V)$ distribution will suddenly change fainter than this limit. Rather, the distribution is likely to gradually fall toward lower $E(B-V)$, or bluer rest-frame continuum spectral slopes (β), proceeding to fainter galaxies, assuming that such fainter galaxies have lower star formation rates and are less dusty than $\mathcal{R} < 25.5$ galaxies. Therefore, the true $E(B-V)$ distribution will very likely fall between the two extremes assumed above. We will return to this point shortly.[15]

[15] We make the reasonable assumption that very dusty ULIRGs with faint UV luminosities make up a small fraction of the total number of UV-faint galaxies. Assuming otherwise would imply a significantly larger number of IR-luminous galaxies than are presently observed in shallow IR surveys (e.g., Pérez-González et al. 2005; Caputi et al. 2007).

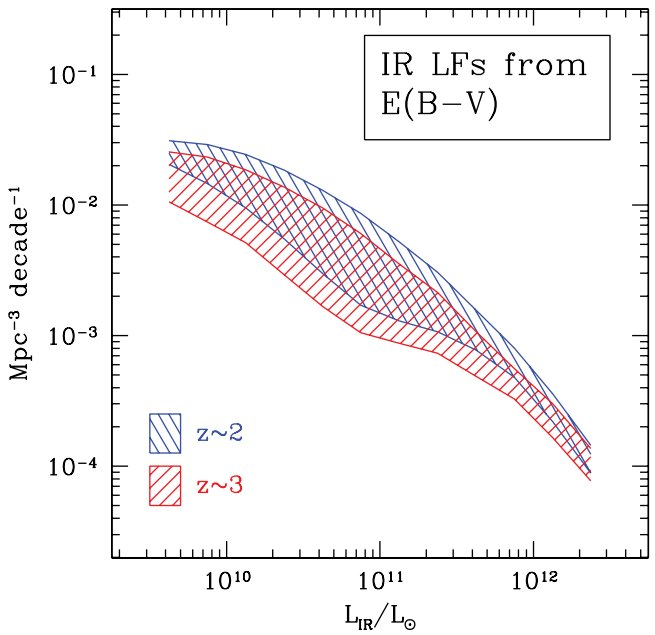

FIG. 16.—Infrared luminosity functions at $z \sim 2$ and $z \sim 3$, calculated assuming the Meurer et al. (1999) and Kennicutt (1998) relations to convert unobscured UV luminosity and $E(B-V)$ to infrared luminosities. The width of the shaded regions reflect the uncertainty in the rest-frame UV-slope and the attenuation distribution for $\mathcal{R} > 25.5$ galaxies (see text).

For now, our IR LFs estimated from the $E(B-V)$ distributions are shown in Figure 16 and tabulated in Table 9. The uncertainty in the LFs include uncertainty in the rest-frame UV faint-end slope and the uncertainty in the $E(B-V)$ distribution for $\mathcal{R} > 25.5$ galaxies. The upper limit of each LF corresponds to the first case where $E(B-V)$ is held constant. The lower limit of each LF corresponds to the second case where $E(B-V)$ suddenly decreases to have a mean of $\langle E(B-V)\rangle = 0.04$ for galaxies fainter than $\mathcal{R} = 25.5$. In general, the systematic uncertainties related to a changing attenuation distribution for UV-faint galaxies will dominate the uncertainties in the faint-end slope (§ 6.3).

6.2. *Distribution of Dust Attenuation Factors*

As alluded to above, the distribution of rest-frame 5–8.5 μm luminosities ($L_{5-8.5\,\mu\mathrm{m}}$) of $z \sim 2$ galaxies observed by *Spitzer* MIPS can be used to assess the infrared luminosity function independent of any assumption regarding the relationship between rest-frame UV slope and extinction, as per the previous discussion. To this end, we must quantify the distribution of dust attenuation among $z \sim 2$ galaxies. For the subsequent discussion, we will define the mid-IR ($\mathcal{A}_{\mathrm{MIR}}$), far-IR ($\mathcal{A}_{\mathrm{IR}}$), and bolometric attenuation ($\mathcal{A}_{\mathrm{bol}}$) factors as the ratio between $\nu L_\nu(8\ \mu\mathrm{m})$, L_{IR}, and L_{bol}, respectively, and L_{1700}. Following the calibration of Reddy et al. (2006b) we can relate these $\mathcal{A}$ factors to each other,

$$\mathcal{A}_{\mathrm{IR}} \approx 12.9\mathcal{A}_{\mathrm{MIR}},$$
$$\mathcal{A}_{\mathrm{bol}} \equiv \frac{L_{\mathrm{IR}} + L_{1700}}{L_{1700}} \equiv \mathcal{A}_{\mathrm{IR}} + 1. \quad (18)$$

Note that these attenuation factors, $\mathcal{A}$, are distinguished from the rest-frame UV attenuation factor, which is the ratio between the dust-corrected and unobscured UV luminosities.

The normal distribution of $E(B-V)$ for galaxies at $z \sim 2$–3 (e.g., Figs. 9 and 10) implies that the attenuation factors $\mathcal{A}$ will abide by a lognormal distribution. We modeled the shape of the $\log \mathcal{A}$ distribution by considering the measured $\log \mathcal{A}$ of rest-UV-selected galaxies with bolometric luminosities $L_{\mathrm{bol}} < 10^{12.3}\ L_\odot$. From Reddy et al. (2006b) $\langle \log \mathcal{A}_{\mathrm{IR}}\rangle \approx 0.67$, implying $L_{\mathrm{IR}}/L_{1700} \approx 4.7$, for the combined sample of 24 μm detected and undetected rest-UV–selected galaxies to $\mathcal{R} = 25.5$. This mean attenuation implies the Gaussian fit shown in Figure 17, compared with the distribution of $\log \mathcal{A}$ for 24 μm detected galaxies.

To construct a fair representation of the attenuation factors of high-redshift galaxies, there is another issue that is pertinent. Namely, the distribution above does not take into account the non-negligible fraction of $z \sim 2$–3 galaxies that have attenuation factors much larger, *on average*, than those of typical galaxies at these redshifts (e.g., Chapman et al. 2003; Reddy et al. 2005; van Dokkum et al. 2003). Virtually all of these galaxies have luminosities $L_{\mathrm{bol}} \gtrsim 10^{12.3}\ L_\odot$ (Reddy et al. 2006b) and ≈50% of those that are also bright at submillimeter wavelengths, $f_{850\,\mu\mathrm{m}} \gtrsim 5$ mJy, also satisfy the BX/LBG criteria. Because our data are most sensitive to galaxies with luminosities $L_{\mathrm{bol}} \lesssim 10^{12.3}\ L_\odot$ and because most galaxies with the largest attenuation factors have $L_{\mathrm{bol}} \gtrsim 10^{12.3}\ L_\odot$, we will only consider the $L_{\mathrm{bol}} < 10^{12}\ L_\odot$ regime when computing the IR LF. We combine our spectroscopically constrained estimate of the IR LF with higher luminosity data from the literature in order to compute the total luminosity and star formation rate densities in §§ 8.3, 8.4, and 8.5.

6.3. *Attenuation of Rest-UV Faint Galaxies*

As discussed in § 6.1, the attenuation distribution of galaxies fainter than our $\mathcal{R}$-band limit for spectroscopy can affect significantly our inferences of the faint end of the IR LFs. Remember that in constructing the IR LFs that we would have inferred based on the UV continuum slope, we considered two cases. In the first, the distribution of $E(B-V)$ is held fixed to the maximum likelihood value (e.g., Fig. 10) irrespective of optical magnitude. In the second, we assumed the maximum likelihood value for those galaxies with $\mathcal{R} < 25.5$; for those fainter than this limit, we assumed a mean $\langle E(B-V)\rangle = 0.04$ (corresponding to $\beta \sim -2.0$ using the Calzetti et al. 2000 relation). To construct the 8 μm, IR, and bolometric LFs based on MIPS 24 μm data, we assumed two cases similar to the ones considered above. In the first, we assume that all galaxies can be ascribed to the attenuation distribution shown in Figure 17. In the second, we assume that the attenuation distribution shifts to a mean of $\langle \log \mathcal{A}_{\mathrm{IR}}\rangle = 0$, with the same dispersion as before, for galaxies with $25.5 \leq \mathcal{R} < 27.5$, then shifts again to a lower mean of $\langle \log \mathcal{A}_{\mathrm{IR}}\rangle = -1$ for galaxies fainter than $\mathcal{R} = 27.5$. The latter corresponds to an attenuation such that 90% of the bolometric luminosity of the galaxy emerges in the UV. Changing the distribution about the specified means does not significantly affect our conclusions. The two cases are illustrated in Figure 18.

It is very likely that the attenuation distribution does not remain constant to arbitrarily faint UV magnitude, as is assumed in case 1. Alternatively, because our $\mathcal{R} = 25.5$ spectroscopic limit is arbitrary, we do not expect the attenuation properties of galaxies fainter than this limit to drastically change. It is more likely that the attenuation distribution gradually shifts to lower mean values for galaxies fainter in the UV. Case 2 can therefore be considered a reasonable lower extreme to the gradient of attenuation as a function of rest-UV magnitude. The true IR LF derived from a realistic attenuation distribution will likely lie between the IR LFs derived assuming case 1 and case 2.

Is there any reason to believe that the attenuation has a much steeper gradient than "case 2" (i.e., Fig. 18, *bottom*)? Future deep stacking analyses and deep spectroscopic campaigns should

TABLE 9
8 μm, IR, and Bolometric Luminosity Functions of $1.9 \lesssim z \lesssim 3.4$ Galaxies

Function	Value	$1.9 \leq z < 2.7$ ($h_{0.7}^3$ Mpc^{-3} decade^{-1})	$2.7 \leq z < 3.4$ (Predicted) ($h_{0.7}^3$ Mpc^{-3} decade^{-1})
$\log [\nu L_\nu(8\ \mu\mathrm{m})]$	8.25–8.50	$(3.01 \pm 1.81) \times 10^{-2}$	$(2.36 \pm 1.79) \times 10^{-2}$
	8.50–8.75	$(3.08 \pm 1.92) \times 10^{-2}$	$(2.25 \pm 1.69) \times 10^{-2}$
	8.75–9.00	$(2.73 \pm 1.70) \times 10^{-2}$	$(1.89 \pm 1.40) \times 10^{-2}$
	9.00–9.25	$(2.20 \pm 1.39) \times 10^{-2}$	$(1.45 \pm 1.07) \times 10^{-2}$
	9.25–9.50	$(1.59 \pm 1.02) \times 10^{-2}$	$(1.02 \pm 0.72) \times 10^{-2}$
	9.50–9.75	$(1.10 \pm 0.69) \times 10^{-2}$	$(6.55 \pm 4.50) \times 10^{-3}$
	9.75–10.00	$(7.26 \pm 4.21) \times 10^{-3}$	$(4.13 \pm 2.38) \times 10^{-3}$
	10.00–10.25	$(4.47 \pm 2.31) \times 10^{-3}$	$(2.64 \pm 1.33) \times 10^{-3}$
	10.25–10.50	$(2.72 \pm 1.08) \times 10^{-3}$	$(1.60 \pm 0.55) \times 10^{-3}$
	10.50–10.75	$(1.54 \pm 0.54) \times 10^{-3}$	$(8.71 \pm 2.37) \times 10^{-4}$
	10.75–11.00	$(7.75 \pm 1.92) \times 10^{-4}$	$(4.62 \pm 1.02) \times 10^{-4}$
	11.00–11.25	$(3.39 \pm 0.71) \times 10^{-4}$	$(2.09 \pm 0.48) \times 10^{-4}$
$\log L_{\mathrm{IR}}$[a]	9.50–9.75	$(2.68 \pm 1.67) \times 10^{-2}$	$(1.89 \pm 1.40) \times 10^{-2}$
	9.75–10.00	$(2.24 \pm 1.40) \times 10^{-2}$	$(1.50 \pm 1.11) \times 10^{-2}$
	10.00–10.25	$(1.69 \pm 1.09) \times 10^{-2}$	$(1.09 \pm 0.78) \times 10^{-2}$
	10.25–10.50	$(1.21 \pm 0.78) \times 10^{-2}$	$(7.49 \pm 5.30) \times 10^{-3}$
	10.50–10.75	$(8.23 \pm 4.93) \times 10^{-3}$	$(4.78 \pm 3.03) \times 10^{-3}$
	10.75–11.00	$(5.52 \pm 3.01) \times 10^{-3}$	$(3.16 \pm 1.68) \times 10^{-3}$
	11.00–11.25	$(3.40 \pm 1.61) \times 10^{-3}$	$(2.01 \pm 0.91) \times 10^{-3}$
	11.25–11.50	$(2.13 \pm 0.76) \times 10^{-3}$	$(1.23 \pm 0.40) \times 10^{-3}$
	11.50–11.75	$(1.18 \pm 0.38) \times 10^{-3}$	$(6.86 \pm 1.86) \times 10^{-4}$
	11.75–12.00	$(5.94 \pm 1.31) \times 10^{-4}$	$(3.58 \pm 0.58) \times 10^{-4}$
	12.00–12.25	$(2.88 \pm 0.59) \times 10^{-4}$	$(1.69 \pm 0.44) \times 10^{-4}$
	12.25–12.50	$(1.10 \pm 0.34) \times 10^{-4}$	$(6.55 \pm 2.37) \times 10^{-5}$
$\log L_{\mathrm{bol}}$[a]	9.50–9.75	$(3.69 \pm 1.78) \times 10^{-2}$	$(2.57 \pm 1.60) \times 10^{-2}$
	9.75–10.00	$(3.23 \pm 1.27) \times 10^{-2}$	$(2.06 \pm 1.15) \times 10^{-2}$
	10.00–10.25	$(2.47 \pm 0.96) \times 10^{-2}$	$(1.49 \pm 0.82) \times 10^{-2}$
	10.25–10.50	$(1.61 \pm 0.83) \times 10^{-2}$	$(9.53 \pm 5.88) \times 10^{-3}$
	10.50–10.75	$(1.04 \pm 0.57) \times 10^{-2}$	$(6.00 \pm 3.61) \times 10^{-3}$
	10.75–11.00	$(6.89 \pm 3.41) \times 10^{-3}$	$(3.90 \pm 1.86) \times 10^{-3}$
	11.00–11.25	$(4.25 \pm 1.84) \times 10^{-3}$	$(2.49 \pm 1.05) \times 10^{-3}$
	11.25–11.50	$(2.51 \pm 0.80) \times 10^{-3}$	$(1.48 \pm 0.45) \times 10^{-3}$
	11.50–11.75	$(1.37 \pm 0.42) \times 10^{-3}$	$(7.81 \pm 1.98) \times 10^{-4}$
	11.75–12.00	$(6.67 \pm 1.32) \times 10^{-4}$	$(4.05 \pm 0.74) \times 10^{-4}$
	12.00–12.25	$(3.12 \pm 0.65) \times 10^{-4}$	$(1.85 \pm 0.52) \times 10^{-4}$
	12.25–12.50	$(1.17 \pm 0.38) \times 10^{-4}$	$(7.67 \pm 2.12) \times 10^{-5}$

Note.—Errors include systematic uncertainty in attenuation distribution for $\mathcal{R} > 25.5$ galaxies, as described in the text.
[a] The values listed in this table are derived assuming the Caputi et al. (2007) calibration between $\nu L_\nu(8\ \mu\mathrm{m})$ and L_{IR}.

resolve this question. For now, we point out that much more extreme cases for the attenuation of UV-faint galaxies (i.e., such that they are even less obscured than what we have considered in case 2) would result in *total* IR LD and SFRD estimates that are comparable, if not lower, than estimates based on samples of the brightest [$\mathcal{R} < 25.5$ and K_s(Vega) < 22] objects at these redshifts, most of which have luminosities comparable to LIRGs and ULIRGs (Reddy et al. 2005). Since the total IR LD and SFRD must be *at least as large* as that contributed by LIRGs and ULIRGs, the attenuation distribution of sub-ULIRG galaxies cannot be much lower than what we have considered here. We will return to this point in § 8.5.

6.4. *Rest-Frame* 8 μm *and IR Luminosity Functions*

Combining our UV LFs with the attenuation distribution derived from MIPS 24 μm observations (using the same method described in § 6.1) results in estimates of the IR LFs. Given the amount of focus in using MIPS 24 μm observations to probe star-forming populations at $z \sim 2$ (e.g., Caputi et al. 2007; Reddy et al. 2006b; Papovich et al. 2006), it is useful to derive a rest-frame 8 μm luminosity function; we did this using the 8 μm attenuation factors observed for $z \sim 2$ galaxies (Reddy et al. 2006b).[16] We then use the relationship between $\mathcal{A}_{\mathrm{IR}}$ and $\mathcal{A}_{\mathrm{MIR}}$ (eq. [18]) to infer the IR luminosity function.

Our inference of the 8 μm and IR LFs at $1.9 \leq z < 2.7$ at faint and moderate luminosities ($L_{\mathrm{IR}} \lesssim 10^{12}\ L_\odot$) are shown in Figure 19 and listed in Table 9. For later comparison, we have assumed the relation between 8 μm and IR luminosity given by Caputi et al. (2007). The upper and lower limits of the shaded regions in the figure correspond to the two different cases of attenuation distributions discussed in the previous section. We cannot directly measure the rest-frame mid-IR luminosities of galaxies at $2.7 \leq z < 3.4$, but we show the predicted 8 μm and IR LFs at these redshifts assuming (1) the same attenuation distribution and (2) the same relationship between mid-IR and total IR luminosities found for $z \sim 2$ galaxies. Figure 19 demonstrates that the IR LF we would have inferred at $10^{9.5}\ L_\odot \lesssim L_{\mathrm{IR}} \lesssim 10^{12}\ L_\odot$ from the rest-frame UV slope, or $E(B-V)$, is consistent with the one inferred from

[16] For ease of comparison with previous literature, we express the mid-IR attenuation factor $\mathcal{A}_{\mathrm{IR}}$ in terms of $\nu L_\nu(8\ \mu\mathrm{m})$ rather than $L_{5-8.5\ \mu\mathrm{m}}$ as was used in Reddy et al. (2006b). The relationship between the two for the typical mid-IR SED of star-forming galaxies is $\nu L_\nu(8\ \mu\mathrm{m}) \approx 0.75 L_{5-8.5\ \mu\mathrm{m}}$.

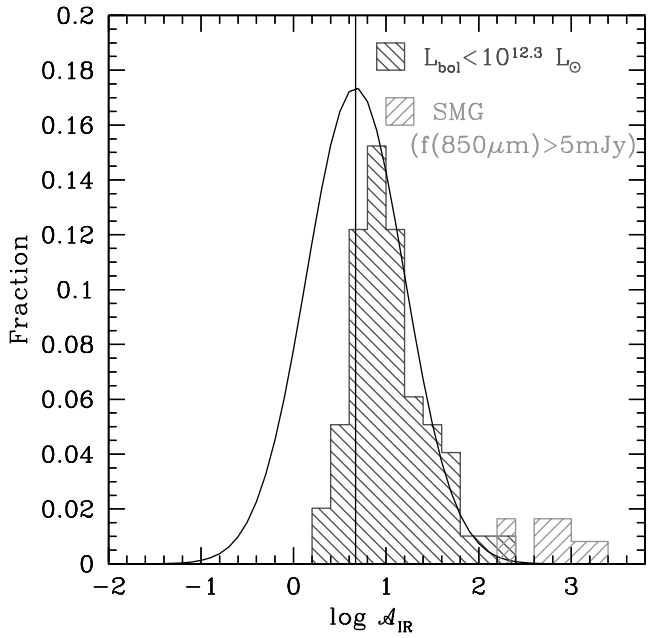

FIG. 17.—Distribution of measured log $\mathcal{A}_{IR}$ for 24 μm detected galaxies with $\mathcal{R} < 25.5$ and luminosities $L_{bol} < 10^{12.3}$ $L_\odot$, indicated by the red hashed histogram. The solid curve denotes the Gaussian fit to the inferred distribution of all $U_nG\mathcal{R}$-selected galaxies with $\mathcal{R} < 25.5$, irrespective of 24 μm detection limit, and the vertical line indicates the mean of the distribution, $\langle \log \mathcal{A}_{IR} \rangle \approx 0.67$. Log $\mathcal{A}_{IR}$ for bright SMGs from the analysis of Reddy et al. (2006b) is also shown. [*See the electronic edition of the Supplement for a color version of this figure.*]

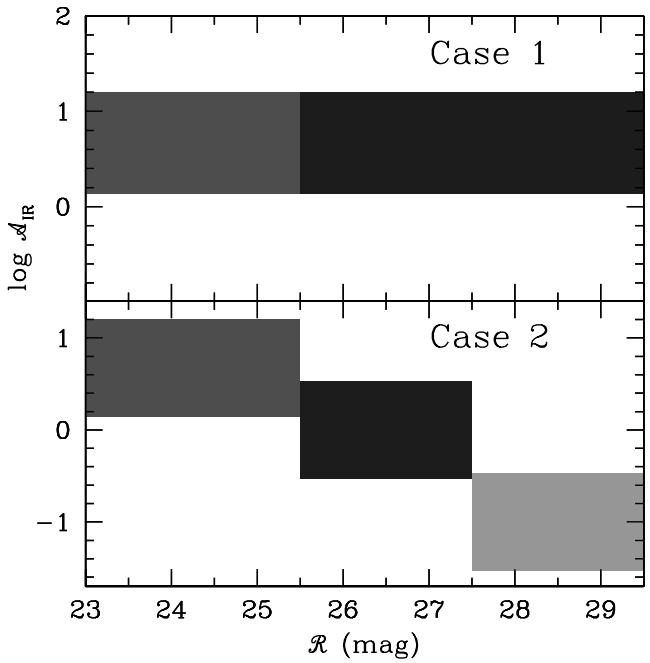

FIG. 18.—Illustration of the two cases we consider for the attenuation distribution of galaxies as a function of rest-frame UV magnitude. In both cases, the height of the bars reflect a 1 σ dispersion of 0.53 dex. [*See the electronic edition of the Supplement for a color version of this figure.*]

the MIPS-determined attenuation factors of these galaxies. This similarity reflects the significant correlation between $E(B-V)$ and attenuation for galaxies with moderate luminosities, and such galaxies are typical of the redshift $z \sim 2$–3 population (i.e., with luminosities corresponding to $\sim L^*$).

Because our data are most sensitive to galaxies with $L_{IR} \lesssim 10^{12}$ $L_\odot$, we must incorporate direct measurements of the IR LF for high-luminosity objects, such as those from *Spitzer* mid-IR surveys. There are several published values of the IR LF for ULIRGs; here we assume the most recent determination from Caputi et al. (2007). Table 10 lists the contribution of galaxies in different luminosity ranges to the IR LD, where we take the total LD to be that of galaxies with $L_{IR} > 6 \times 10^8$ $L_\odot$. This limit corresponds to galaxies with SFRs of ~ 0.1 $M_\odot$ yr^{-1}. The total LD changes negligibly by integrating to zero luminosity. Table 10 shows that—despite the large systematic uncertainties at the faint end induced by variations in the attenuation distribution—a significant fraction of the IR LD at $z \sim 2$ arises from galaxies with sub-ULIRG luminosities. We will return this point in § 8.4.

6.5. *Bolometric Luminosity Functions*

Finally, to gain an accurate picture of the distribution of total energetics of star-forming galaxies, we must consider the combined contribution from unobscured (UV) luminosity and obscured (IR) luminosity. While the bolometric luminosity should closely follow the infrared luminosity for luminous galaxies ($L_{bol} \approx L_{IR} \gtrsim 3 \times 10^{11}$ $L_\odot$), Reddy et al. (2006b) show that such an assumption is no longer valid for galaxies with $L_{bol} \lesssim 3 \times 10^{11}$ $L_\odot$ (at $z \sim 2$), given the very tight correlation between dust obscuration and bolometric luminosity. For example, a 10^{11} $L_\odot$ galaxy at $z \sim 2$ will on average have half of its total luminosity emerging at UV wavelengths; similarly, a $10^{10.5}$ $L_\odot$ galaxy at $z \sim 2$ will on average have 84% of its bolometric luminosity emerging at UV wavelengths.[17] Figure 20 shows the bolometric luminosity functions of star-forming galaxies at redshifts $1.9 \leq z < 3.4$, and the values are listed in Table 9. The bolometric LF is larger in all luminosity bins considered than the IR LFs given that objects will shift from lower to higher luminosity bins after accounting for the emergent UV luminosity of high-redshift galaxies. We note that in computing our prediction for the bolometric LF at $2.7 \leq z < 3.4$, we have assumed the same distribution of attenuation factors that was found for $z \sim 2$ galaxies, as was done in computing the IR LFs. The bolometric LFs are presented here because they give a true picture as to the total energetic output of galaxies, irrespective of dust extinction or the fraction of unobscured luminosity. In section § 8.5, we will discuss what the spectroscopically constrained bolometric LFs imply for the contribution of moderate luminosity (10^{11} $L_\odot \lesssim L_{bol} \lesssim 10^{12}$ $L_\odot$) galaxies to the global luminosity density.

7. RESULTS: Hα LUMINOSITY FUNCTION

We briefly discuss our derivation of the Hα LFs here, as they may be useful for current and future high-redshift emission line studies. The key ingredient that allows us to convert our UV LF into an estimate of the Hα LF is the correlation between dust-corrected UV and Hα estimates of star formation rates. Erb et al. (2006b) found a significant (6.8 σ) correlation with 0.3 dex scatter between the extinction-corrected UV estimates and Hα estimates of the SFRs, assuming the Calzetti et al. (2000) relation

[17] While the tight correlation between L_{bol} and attenuation has been observed both locally and at high redshift, the *normalization* of the relationship increases at higher redshift. This means, for example, that galaxies at $z \sim 2$ are on average 10 times more luminous for a given dust obscuration (or are 10 times less dust obscured for a given L_{bol}) than $z = 0$ galaxies (Reddy et al. 2006b). Hence, the fraction of total luminosity emerging in the UV is larger at higher redshift than it is locally for galaxies of a given bolometric luminosity. Note that this observation is still consistent with the finding that dustier systems dominate the luminosity density at $z \sim 1$–2 relative to the present day (e.g., Le Floc'h et al. 2005; Takeuchi et al. 2005), as we discuss in § 8.4.

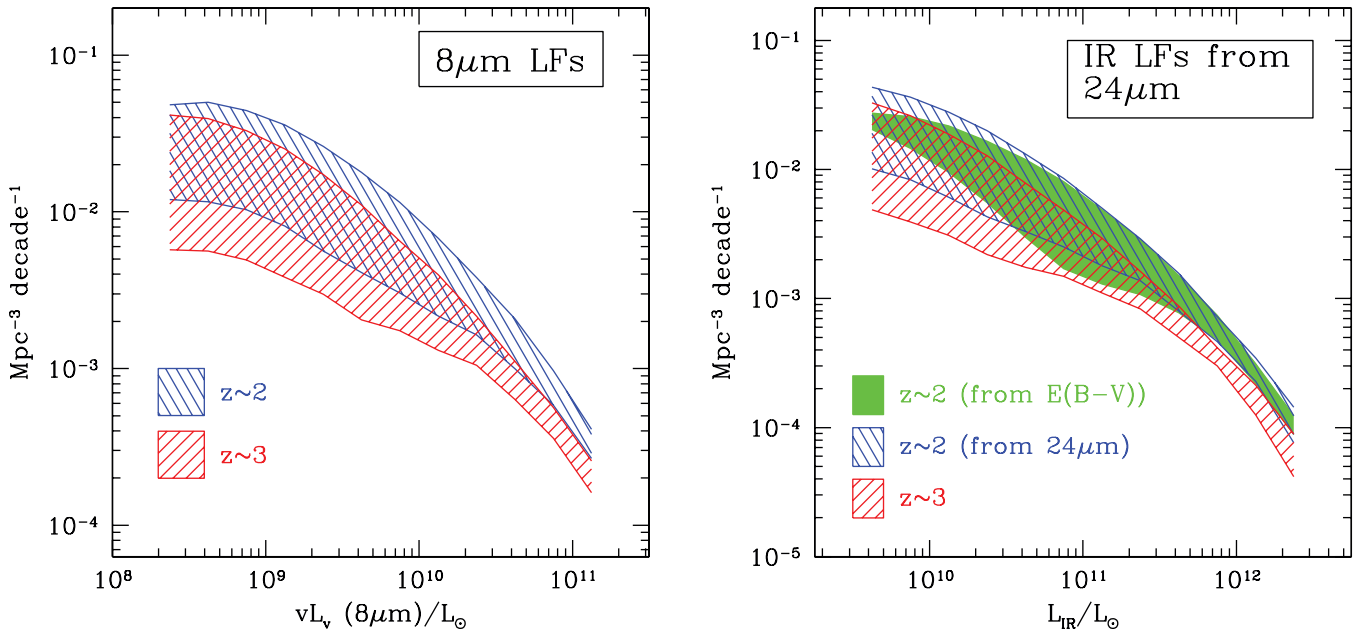

FIG. 19.—Infrared and 8 μm luminosity functions at redshift $1.9 \leq z < 2.7$, compared with predictions in the higher redshift range $2.7 \leq z < 3.4$. The right panel also demonstrates the similarity in the IR LF derived from the rest-frame UV slope (Fig. 16) with that derived using the attenuation factors calculated from *Spitzer* MIPS observations of $1.5 \lesssim z \lesssim 2.6$ galaxies in the GOODS-N field (Reddy et al. 2006b).

for a sample of 114 rest-frame UV-selected galaxies at $z \sim 2$. We can invert the relationship between extinction-corrected SFR and Hα line emission in order to infer the Hα LF. The spectroscopic Hα observations used to establish the correlation between Hα and UV-determined SFRs are described in detail in Erb et al. (2006a, 2006b, 2006c).

7.1. *Method*

The method used to estimate the Hα LF of $z \sim 2$ galaxies is analogous to that presented in § 6.1. We generated many realizations of the LF and $E(B-V)$ distributions and randomly selected magnitudes and $E(B-V)$. To determine the Hα luminosity corresponding to this dust-corrected UV luminosity, we assumed that the UV and Hα emission are tied directly to the SFR of the galaxy, where the SFR is calibrated using the Kennicutt (1998) relations. It is then easy to show that

$$L_{\mathrm{H}\alpha}[\mathrm{ergs\ s^{-1}}] \approx 1.77 \times 10^{13} L_{1700}[\mathrm{ergs\ s^{-1}\ Hz^{-1}}]. \quad (19)$$

The resulting Hα luminosities are then perturbed by 0.3 dex to account for the dispersion in the relation between the dust-corrected UV and Hα estimates (Erb et al. 2006b). For consistency with previous determinations of the Hα LF at lower redshifts, it is useful to derive an Hα luminosity function *uncorrected* for extinction at $z \sim 2$. To accomplish this, we assume that the $E(B-V)$ value, which is derived from the rest-frame UV colors, reflects the nebular reddening of the galaxy (see also Erb et al. 2006b). Applying the Calzetti et al. (2000) relation to the intrinsic Hα luminosity, and assuming the same value of $E(B-V)$, yields an estimate of the observed Hα luminosity.[18] Note that because the

[18] Erb et al. (2006b) show that assuming the same $E(B-V)$ in dust-correcting the Hα estimates, as opposed to a smaller nebular reddening as advocated by Calzetti et al. (2000), results in better agreement with dust-corrected UV and stacked X-ray estimates.

TABLE 10
CONTRIBUTIONS OF THE IR LD AT $z \sim 2$

L_{IR}	log IR LD
10^9–10^{10} $L_\odot$	8.03 ± 0.17 (9%)
10^{10}–10^{11} $L_\odot$	8.45 ± 0.09 (23%)
10^{11}–10^{12} $L_\odot$	8.68 ± 0.06 (39%)
$>10^{12}$ $L_\odot$	8.48 ± 0.32 (25%)[a]
Total ($6 \times 10^8 < L_{\mathrm{IR}} < \infty$)[b]	9.09 ± 0.08

[a] From Caputi et al. (2007).
[b] The lower limit of $L_{\mathrm{IR}} = 6 \times 10^8$ $L_\odot$ roughly corresponds to an SFR of 0.1 $M_\odot$ yr^{-1}.

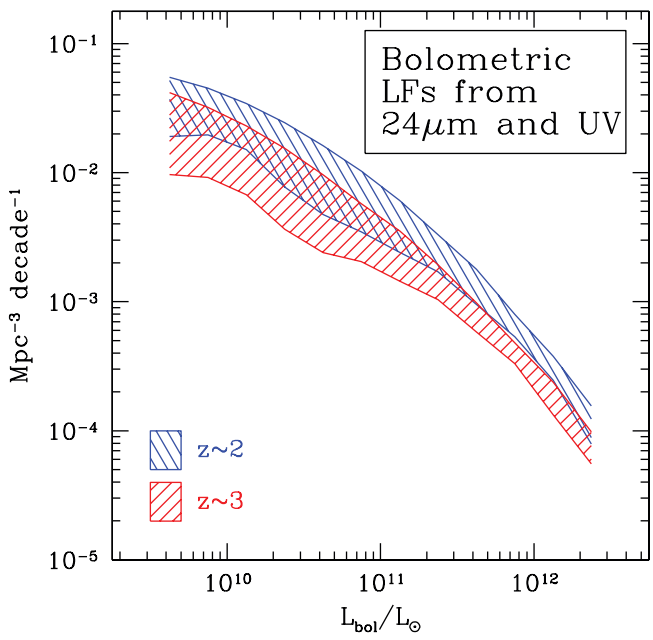

FIG. 20.—Bolometric luminosity function at redshift $1.9 \leq z < 2.7$, calculated using the sum of the UV (unobscured) and IR (obscured) luminosities of galaxies. Our prediction of the bolometric LF at $2.7 \leq z < 3.4$ is also shown.

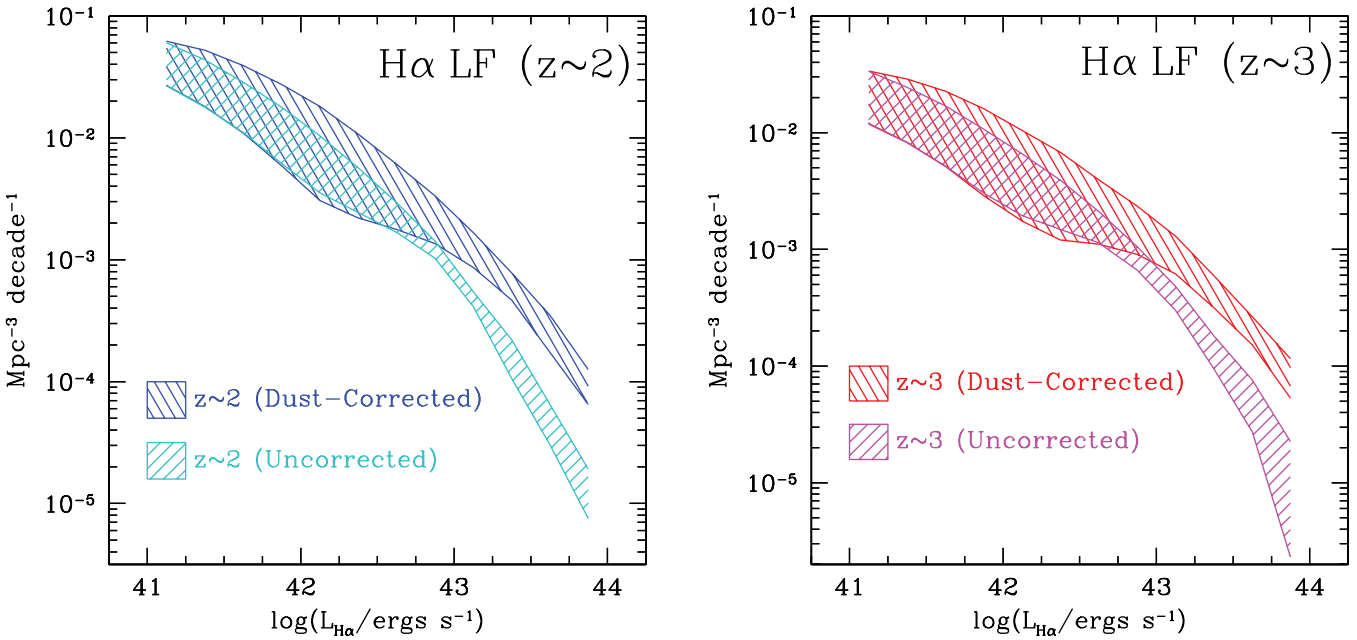

FIG. 21.—Dust-corrected and observed (uncorrected for extinction) Hα LFs inferred for star-forming galaxies with redshifts $1.9 \leq z < 2.7$ (*left*) and $2.7 \leq z < 3.4$ (*right*). The uncertainty of each LF, represented by the width of the shaded regions, is dictated by the uncertainty in (1) the $E(B-V)$ distribution for $\mathcal{R} > 25.5$ galaxies and (2) the rest-frame UV faint-end slope. Values are tabulated in Table 11.

attenuation $A_\lambda/E(B-V)$ is a factor of ≈3 smaller at the wavelength of Hα, 6563 Å, than at 1700 Å, it is not correct to simply convert the observed UV luminosity to a SFR and then back to an observed Hα luminosity: one must take into account the differential extinction, for a given $E(B-V)$, between these two wavelengths. The dust-corrected (intrinsic) and uncorrected (observed) Hα luminosities are then binned to produce a dust-corrected and observed Hα LF, respectively. We considered the same two cases for the $E(B-V)$ distribution of UV-faint galaxies as in § 6.1. Our predictions for the uncorrected and dust-corrected Hα LFs at $z \sim 2$ are shown in Figure 21 and listed in Table 11.

7.2. *Predicted* Hα *LFs at* $z \sim 3$

The correlation between UV and Hα SFRs has only been tested directly at redshifts $2.0 \lesssim z \lesssim 2.6$, where the Hα line falls within the *K* band, making it accessible to near-IR spectrographs, such as Keck II NIRSPEC (McLean et al. 1998). It is useful, nonetheless, to predict the form of the Hα LF at $z \sim 3$ assuming that the correlation between UV and Hα SFRs holds at these higher redshifts. This is a reasonable assumption to make given that, to $\mathcal{R} = 25.5$, the $z \sim 2$ and $z \sim 3$ samples host galaxies with a virtually identical range of $E(B-V)$ (Fig. 10), and galaxies in these respective samples have similar average dust attenuation factors, represented as the ratio of the dust-corrected UV and unobscured UV luminosities, of ∼4–5 based on X-ray and radio stacking analyses (Nandra et al. 2002; Reddy & Steidel 2004). Our predictions for the uncorrected and dust-corrected Hα LFs at $z \sim 3$, computed using the steps above and using the combined ground-based and HDF samples to generate the UV LF realizations, are shown in Figure 21 and listed in Table 11. We briefly present a comparison of our Hα LFs and luminosity densities with others from the literature in § 8.3.2.

8. DISCUSSION

We have presented the most robust estimates of the rest-frame UV LFs and moderate luminosity regime of the IR LFs of

TABLE 11

Hα LUMINOSITY FUNCTIONS OF $1.9 \lesssim z \lesssim 3.4$ GALAXIES

$\log L(\mathrm{H}\alpha/\mathrm{ergs\ s^{-1}})$	$1.9 \leq z < 2.7$ Observed ϕ ($\mathrm{Mpc^{-3}\ decade^{-1}}$)	$1.9 \leq z < 2.7$ Dust-corrected ϕ ($\mathrm{Mpc^{-3}\ decade^{-1}}$)	$2.7 \leq z < 3.4$ (Predicted) Observed ϕ ($\mathrm{Mpc^{-3}\ decade^{-1}}$)	$2.7 \leq z < 3.4$ (Predicted) Dust-corrected ϕ ($\mathrm{Mpc^{-3}\ decade^{-1}}$)
41.00–41.25	$(4.34 \pm 1.66) \times 10^{-2}$	$(4.44 \pm 1.75) \times 10^{-2}$	$(1.72 \pm 0.55) \times 10^{-2}$	$(2.27 \pm 1.09) \times 10^{-2}$
41.25–41.50	$(3.07 \pm 1.29) \times 10^{-2}$	$(3.52 \pm 1.71) \times 10^{-2}$	$(1.33 \pm 0.48) \times 10^{-2}$	$(1.63 \pm 0.81) \times 10^{-2}$
41.50–41.75	$(1.98 \pm 0.88) \times 10^{-2}$	$(2.51 \pm 1.41) \times 10^{-2}$	$(9.18 \pm 3.83) \times 10^{-3}$	$(1.11 \pm 0.59) \times 10^{-2}$
41.75–42.00	$(1.20 \pm 0.59) \times 10^{-2}$	$(1.67 \pm 1.07) \times 10^{-2}$	$(6.07 \pm 2.70) \times 10^{-3}$	$(6.87 \pm 3.85) \times 10^{-3}$
42.00–42.25	$(6.95 \pm 3.42) \times 10^{-3}$	$(1.05 \pm 0.75) \times 10^{-2}$	$(3.94 \pm 1.26) \times 10^{-3}$	$(4.25 \pm 2.31) \times 10^{-3}$
42.25–42.50	$(4.07 \pm 1.62) \times 10^{-3}$	$(6.48 \pm 4.28) \times 10^{-3}$	$(2.44 \pm 0.82) \times 10^{-3}$	$(2.70 \pm 1.22) \times 10^{-3}$
42.50–42.75	$(2.31 \pm 0.63) \times 10^{-3}$	$(3.93 \pm 2.16) \times 10^{-3}$	$(1.55 \pm 0.33) \times 10^{-3}$	$(1.63 \pm 0.49) \times 10^{-3}$
42.75–43.00	$(1.23 \pm 0.20) \times 10^{-3}$	$(2.35 \pm 0.99) \times 10^{-3}$	$(7.63 \pm 2.21) \times 10^{-4}$	$(8.60 \pm 1.94) \times 10^{-4}$
43.00–43.25	$(4.80 \pm 0.66) \times 10^{-4}$	$(1.27 \pm 0.40) \times 10^{-3}$	$(3.30 \pm 0.93) \times 10^{-4}$	$(3.91 \pm 0.90) \times 10^{-4}$
43.25–43.50	$(1.63 \pm 0.58) \times 10^{-4}$	$(6.22 \pm 1.57) \times 10^{-4}$	$(1.38 \pm 0.91) \times 10^{-4}$	$(1.38 \pm 0.43) \times 10^{-4}$
43.50–43.75	$(4.74 \pm 1.71) \times 10^{-5}$	$(2.61 \pm 0.88) \times 10^{-4}$	$(3.44 \pm 2.23) \times 10^{-5}$	$(5.13 \pm 2.41) \times 10^{-5}$
43.75–44.00	$(1.34 \pm 0.58) \times 10^{-5}$	$(9.53 \pm 3.03) \times 10^{-5}$	$(2.11 \pm 1.89) \times 10^{-5}$	$(1.24 \pm 1.01) \times 10^{-5}$

NOTE.—Errors include the systematic uncertainty in the $E(B-V)$ distribution for $\mathcal{R} > 25.5$ galaxies, as described in the text.

star-forming galaxies at redshifts $1.9 \leq z < 3.4$ (§§ 5, 7, and 6). We have demonstrated how photometric redshifts over this redshift range can introduce nontrivial biases in the LF, underscoring the need for spectroscopy where it is feasible (§ 5.5). Further, our extensive spectroscopy allows us to examine other systematic effects, including Lyα line perturbations to the intrinsic rest-frame UV colors of galaxies (§§ 7 and 6). In the next section, we will examine more closely the trend between Lyα emission and redshift and its dependence on the physical properties of galaxies. In § 8.2, we discuss recent results that have indicated an excess of bright galaxies at $z \sim 3$ over that observed in the initial LBG studies of Steidel et al. (1999) and Dickinson (1998). Comparison of our UV, Hα, and IR LFs with those of previous studies, and the evolution in the LF and luminosity density, are discussed in §§ 8.3 and 8.4. Integral constraints on the star formation rate density are presented in § 8.5.

8.1. $W_{\rm Ly\alpha}$ *Distribution as a Function of Redshift*

The analysis of § 4.1 demonstrated that the intrinsic $W_{\rm Ly\alpha}$ distribution of galaxies at $1.9 \leq z < 3.4$ was not significantly modulated by the BX and LBG color criteria and, furthermore, that the fraction of galaxies with $W_{\rm Ly\alpha} \geq 20$ Å ($f20$) was larger at higher redshifts. This trend was recognized by comparing $f20$ between (1) BX galaxies and LBGs and (2) BX galaxies at $z \leq 2.48$ and $z > 2.48$, with the results summarized in Table 4. In the latter case, the fact that we see a trend in $f20$ with redshift even for galaxies selected using a single set of color criteria (BX) further strengthens our conclusions that $f20$ increases with redshift, irrespective of selection biases (see Fig. 3).

To interpret this trend in a physical context, we assembled the stellar population parameters for galaxies with measured $W_{\rm Ly\alpha}$, where SED modeling was available from Shapley et al. (2005) and Reddy et al. (2006a). The resulting sample includes 139 galaxies, 14 with $W_{\rm Ly\alpha} \geq 20$ Å. We used K-S tests to determine whether the SED parameters (star formation histories, ages, stellar masses, and star formation rates) for galaxies with $W_{\rm Ly\alpha} < 20$ Å are drawn from the same parent population as those with $W_{\rm Ly\alpha} \geq 20$ Å. Doing this, we found no significant differences in the star formation histories, ages, stellar masses, and star formation rates of galaxies between these two samples. This result is not surprising given (1) the small sample size analyzed here, (2) the significant systematic degeneracies between SED parameters (e.g., Shapley et al. 2005; Erb et al. 2006c; Papovich et al. 2001), and (3) the large uncertainty in the measured $W_{\rm Ly\alpha}$ for individual galaxies. Galaxies with $W_{\rm Ly\alpha} \geq 50$ Å have an average age of $\sim$300 $\pm$ 300 Myr, whereas those below this limit have an average age of $\sim$460 $\pm$ 600 Myr. The difference in average age is not significant given the large dispersion in ages measured for the two samples.

Nonetheless, several previous studies at $z \gtrsim 4$ suggest that Lyα emitting galaxies are young ($\lesssim$50 Myr), low-metallicity systems with small stellar masses (e.g., Stanway et al. 2007; Pentericci et al. 2007; Dow-Hygelund et al. 2007; Pirzkal et al. 2006; Finkelstein et al. 2007; Lehnert & Bremer 2003), particularly in relation to galaxies without Lyα in emission at the same redshifts ($z \sim 6$; Stanway et al. 2007; Dow-Hygelund et al. 2007). Results at $z \sim 2$ also indicate that low stellar mass and low-metallicity galaxies have significantly stronger Lyα emission than high stellar mass and high-metallicity galaxies (Erb et al. 2006a). Among UV-continuum–selected samples, both Dow-Hygelund et al. (2007) and Stanway et al. (2007) find a fraction of $z \sim 6$ galaxies with $W_{\rm Ly\alpha} \lesssim 25$ Å similar to the fraction found at $z \sim 3$ (Shapley et al. 2003), but the former find an excess of high equivalent width galaxies ($W_{\rm Ly\alpha} > 100$ Å) compared to the $z \sim 3$ sample. Further, the connection between Lyα profiles and the physical properties of galaxies is well-known to be quite complicated, with a sensitivity to ionizing flux, dust obscuration, and velocity of outflowing material (e.g., Tapken et al. 2007; Reddy et al. 2006b; Hansen & Oh 2006; Shapley et al. 2003; Adelberger et al. 2003). Despite these complications, the advantage of our large spectroscopic analysis is that we can very accurately quantify the trends between Lyα emission and redshift (§ 4.1). The presently small samples at $z \sim 6$ prevent us from determining whether the trends observed at $1.9 \leq z < 3.4$ extend to higher redshift, but the general expectation is that if younger and less dusty galaxies preferentially show Lyα in emission, then the frequency of such Lyα emitting galaxies should increase with increasing redshift as the average galaxy age (and average dust-to-gas ratios; see Reddy et al. 2006b) decreases.

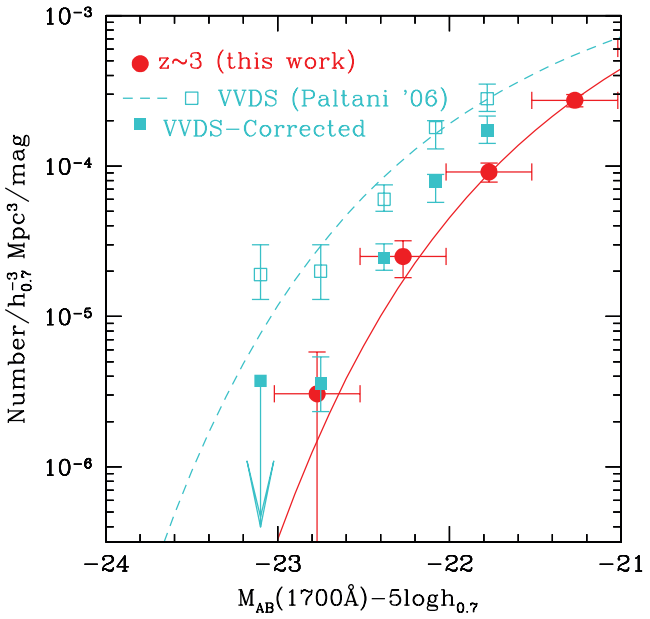

FIG. 22.—Comparison of our $z \sim 3$ UV LF determination (circles for data, and solid line for best-fit Schechter function) and that of the VVDS (*open squares and dashed line*). Correcting the VVDS points for (*a*) objects outside the redshift range $2.7 \leq z < 3.4$ and (*b*) AGNs/QSOs at redshifts $2.7 \leq z < 3.4$, as determined from our spectroscopic sample, results in much better agreement between the two LFs, as indicated by the filled squares.

8.2. *VVDS-Inferred Excess of Bright* $M(1700\ \text{Å}) \lesssim -22.0$ *Galaxies at Redshifts* $2.7 \lesssim z \lesssim 3.4$

Recently, Le Fèvre et al. (2005) reported results from the *I*-band magnitude limited VIMOS VLT Deep Survey (VVDS) that indicated a significant excess of bright [$M(1700\ \text{Å}) \lesssim -22.0$] galaxies with redshifts $2.7 \lesssim z \lesssim 3.4$ compared with the earlier results of Steidel et al. (1999) and those inferred here from our likelihood analysis. Paltani et al. (2007) further quantified this excess by casting it into the form of a luminosity function, which we reproduce in Figure 22.[19]

We suggest two reasons for the discrepancy between our LF and that of the VVDS. First, the frequency of objects with redshifts *outside* the redshift range $2.7 \leq z < 3.4$ (i.e., the contamination fraction; f_c) for $M(1700\ \text{Å}) \lesssim -22.0$ is significantly larger than the value inferred by Paltani et al. (2007) and Le Fèvre et al.

[19] Although the VVDS UV LF of Paltani et al. (2007) is computed in a slightly different redshift range, $3 \lesssim z \lesssim 4$, from that considered for our $z \sim 3$ LF ($2.7 \leq z < 3.4$), the comparison between the two is valid since we find little evolution in the number density of $M(1700\ \text{Å}) \lesssim -22.0$ galaxies between $z \sim 3$ and $z \sim 4$.

(2005) based on the statistics of our much larger spectroscopic sample. To illustrate this, we must first consider how Paltani et al. (2007) weight their galaxies in their computation of the LF to account for f_c. The VVDS redshifts used to compute the LF fall within four categories. Flag-1 and flag-2 objects are considered to have the least secure redshifts, whereas flag-3 and flag-4 objects are more secure (Paltani et al. 2007). Paltani et al. then determine a contamination fraction of $f_c \sim 0.54$ for the 254 flag-1 and 2 sources and assume a value of $f_c = 0$ for the 12 flag-3 and 4 sources that are used in their LF computation. Weighting the fractions according to the number of sources then yields a net contamination rate of $[254 \times 0.54 + 12 \times 0]/[254 + 12] \approx 0.52$.[20]

The actual contamination rate among VVDS objects must be larger than $f_c = 0.52$ for several reasons. First, the BX and LBG criteria account for the $U_nG\mathcal{R}$ colors of ~70%–80% of VVDS objects claimed to lie at $2.7 \leq z < 3.4$ (see Fig. 5 of Paltani et al. (2007) and Fig. 3 of Le Fèvre et al. (2005), where most of the objects lie in the *same* region of color space encompassed by either the BX or LBG criteria). However, 77% of spectroscopically confirmed candidates in the BX and LBG samples with $M(1700\ \text{Å}) \lesssim -22.0$ are low-redshift interlopers (Table 3).[21]

Second, VVDS objects that do not satisfy the BX and LBG color criteria because of their redder $G - \mathcal{R}$ colors lie in the same region of color space as low-redshift star-forming galaxies (e.g., Adelberger et al. 2004; Reddy et al. 2005). Without additional K_s-band data to exclude these low-z interlopers (e.g., *BzK* selection of Daddi et al. 2004b), the contamination rate among these red $G - \mathcal{R}$ objects is likely to be at least as large as the rate among objects that are targeted by criteria specifically *designed* to selected galaxies at $2.7 \leq z < 3.4$ (e.g., the LBG color criteria). To quantify this further, we turned to the magnitude limited Team Keck Redshift Survey database in the GOODS-N field (TKRS; Wirth et al. 2004; Cowie et al. 2004). There are 2471 TKRS sources with $\mathcal{R} \leq 24$ (roughly corresponding to the VVDS magnitude limit) with matching $U_nG\mathcal{R}$ photometry in our catalog. Of these matches, there are 755 sources that satisfy the following conditions: (1) spectroscopically observed in the TKRS, (2) do not satisfy either the BX or LBG criteria, and (3) have $U_n - G > 0.4$ and $G - \mathcal{R} < 1.8$. These limits define the region in color space of the ≈20% of VVDS objects that do not satisfy the BX or LBG criteria.[22] Of these 755 bright sources that were observed in TKRS, 581, or ≈77%, are spectroscopically confirmed to lie at redshifts $z \lesssim 1.4$. This is a strict lower limit to the contamination rate since there will be (1) some $1.4 < z < 2.7$ galaxies that are missed simply because the lines used for redshift identification are shifted out of the TKRS wavelength coverage and (2) some galaxies with $z < 1.4$ that are unidentified because of poor weather, bad reduction, and other reasons.

Finally, the instrumental setup used by the VVDS to obtain spectroscopy, resulting in observed wavelengths of 5500 and 9500 Å, is highly nonoptimal for selecting LBGs, particularly because of the lack of coverage around the Lyα line. In summary, our value of $f_c = 0.77$ is significantly larger than the value of $f_c = 0.52$ claimed by Paltani et al. (2007) yet is based on our sample of 285 *secure* spectroscopic redshifts versus only 12 secure redshifts and 254 unsecure redshifts of the VVDS survey. For the reasons discussed above, the real contamination rate among VVDS objects is likely to be larger than $f_c = 0.77$. Even so, assuming this fraction would conservatively lower the brightest VVDS LF points by a factor of at least 2. We already alluded to how catastrophic redshift errors can artificially boost the bright end of the LF in § 5.5.

The excess of bright galaxies in the VVDS LF is also likely to be due in part to the presence of non–star-forming galaxies at redshifts $2.7 \leq z < 3.4$, in other words QSOs and other bright AGNs. We have explicitly excluded AGNs from our LF determination, as described in § 2.5, but this was not done for the VVDS analysis. Based on our spectroscopy, the AGN/QSO contamination rate is a strong function of magnitude and is larger than ~60% in the brightest luminosity bin of the VVDS analysis (Table 2). In fact, of the 14 spectroscopically confirmed LBGs in our sample with $M(1700\ \text{Å}) \lesssim -22.5$, 11 (or roughly 80%) are QSOs or bright AGNs. Applying the AGN/QSO contamination fractions (as determined from our spectroscopy) will further reduce the brightest VVDS LF points by a factor of 2.5.

To conclude our comparison, the two primary causes for the excess of bright galaxies inferred by the VVDS is (1) their underestimate of the fraction of objects that lie outside the redshift range $2.7 \leq z < 3.4$ and (2) the fraction of bright AGNs and QSOs at redshifts $2.7 \leq z < 3.4$. Our spectroscopy, which is the most extensive at the redshifts in question and was obtained using the most optimal instrumental setup to identify galaxies at $2.7 \leq z < 3.4$, allows us to very accurately quantify the magnitude of both sources of contamination, all within a combined survey area that is roughly twice as large as the VVDS field. Figure 22 demonstrates that applying the contamination fractions determined from our spectroscopy to the VVDS points (after factoring out the VVDS contamination correction) results in a better agreement between the VVDS and our LF. Taking all these results into consideration, we find no convincing evidence for an excess of bright galaxies at $2.7 \leq z < 3.4$.

Finally, the agreement between our corrected estimate of the VVDS LF (derived from a magnitude-limited survey) with the one from our likelihood analysis (derived from a color-selected survey), strongly suggests that our LF must be reasonably complete for UV-bright galaxies.

8.3. *Evolution of the UV and* Hα *Luminosity Functions and Densities*

8.3.1. *UV LFs*

Figure 12 summarizes our determinations of the rest-frame UV LFs at redshifts $1.9 \leq z < 3.4$, compared with the Steidel et al. (1999) LF at $z \sim 4$. As our method of constraining the reddening and luminosity distributions takes into account a number of systematic effects (e.g., contamination fraction particularly at the bright end of the LF, photometric bias and errors, and Lyα line perturbations to the observed colors[23]) that have not been considered in previous analyses (e.g., Gabasch et al. 2004; Le Fèvre et al. 2005) or were only partially considered (Steidel et al. 1999; Adelberger & Steidel 2000; Sawicki & Thompson 2006), we regard our LFs as the most robust determinations at $z \sim 2$ and $z \sim 3$ to $\mathcal{R} = 25.5$.

Our analysis indicates that the rest-frame UV LF shows little evolution for galaxies brighter than M^* (at $z \sim 2$) between redshifts

[20] This gives the same result as the "photometric rejection" method, where 137 of 266 objects are likely to lie outside the redshift range $2.7 \leq z < 3.4$, as discussed in Paltani et al. (2007).

[21] For the BX sample, most of the contamination at bright magnitudes arises from foreground galaxies. For the LBG sample, most of the contamination arises from stars.

[22] Note that although nominally the BX criteria are designed to select galaxies with $z < 2.7$, we include them in the discussion here since a significant fraction of VVDS objects claimed to lie at $z \gtrsim 3$ fall in the same region of color space as BX candidates.

[23] Our determinations of the LFs are insensitive to small changes in the assumed $W_{\text{Ly}\alpha}$ distributions, such as those caused by trends in $W_{\text{Ly}\alpha}$ with apparent magnitude and color.

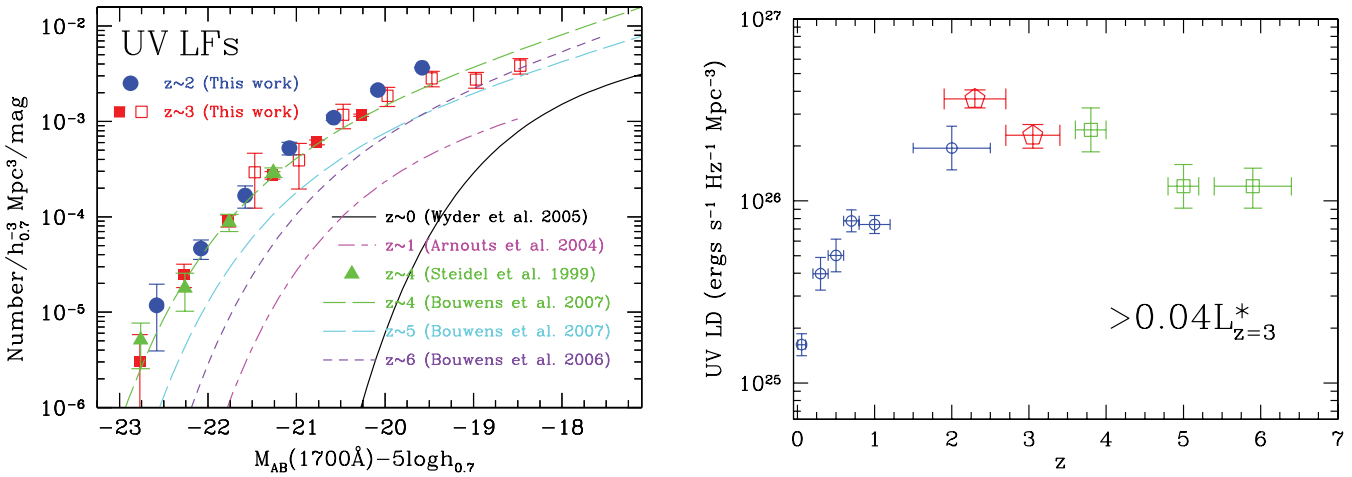

FIG. 23.—*Left*: Comparison of a *few* UV LFs from the literature. The local UV LF (derived from *GALEX* data) is shown (Wyder et al. 2005) along with the $z \sim 1$ UV LF from Arnouts et al. (2005) as well as higher redshift determinations from the *B*, *V*, and *I* dropout samples of Bouwens et al. (2007). *Right*: Unobscured (uncorrected for extinction) UV luminosity density, integrated to a fixed luminosity of $L_{\rm lim} = 0.04L^*_{z=3}$, from the following sources: Wyder et al. (2005) at $z \sim 0$; Schiminovich et al. (2005) at $z \sim 0.3$–1.0; Arnouts et al. (2005) at $z \sim 2.0$ from a photometric redshift analysis of the HDF–North and HDF–South fields; and Bouwens et al. (2007) at $z \sim 4$–6. Our determinations at $z \sim 2$ and $z \sim 3$ are shown by the large red pentagons.

$1.9 \leq z < 4.5$: the number density of galaxies brighter than $M^* = -21.01$ appears to be constant over the $\sim$1.3 Gyr timespan between $z \sim 4$ and $z \sim 2.3$. This lack of evolution in the bright end of the UV LFs does not specifically address how a galaxy of a particular luminosity will evolve. For example, the lack of evolution at the bright end [$M_{\rm AB}(1700\ {\rm Å}) \lesssim -21$] of the LF does not imply that there is a population of UV-bright galaxies that is unevolving. Rather, if galaxies follow an exponentially declining star formation history, then UV-bright galaxies at $z \sim 3$ will become fainter in the UV by $z \sim 2$ but will not necessarily be absent from the $z \sim 2$ sample. A precipitously declining star formation history may imply that some UV-bright galaxies at $z \sim 3$ will be too faint to be included in UV-selected samples at $z \sim 2$. In any case, the lack of evolution at the bright end of the UV LF implies that whatever UV-bright galaxies at $z \sim 3$–4 fall out of UV-selected samples by $z \sim 2$ must be made up in number by younger galaxies, those that are merging and just "turning on" and/or those that are caught in an active phase of star formation at $z \sim 2$. The net effect is that the number density of galaxies with [$M_{\rm AB}(1700\ {\rm Å}) \lesssim -21$] remains essentially constant.

For galaxies fainter than M^*, we do find evidence for a small evolution between $z \sim 3$ and $z \sim 2$: the number density of galaxies fainter than $M^* = -21.01$ is systematically larger at $z \sim 2$ than at $z \sim 3$ to a lower luminosity limit of $\mathcal{R} = 25.5$ or $M_{\rm AB}(1700\ {\rm Å}) \sim -19$, although the result is not of great significance given the generally overlapping error bars on the points between $z \sim 2$ and $z \sim 3$. What is clear is that the number density of $-21 \lesssim M_{\rm AB}(1700\ {\rm Å}) \lesssim -19$ galaxies at $z \sim 2$ is *at least* as large as the corresponding number density at $z \sim 3$. To put these results in context, Figure 23 summarizes our results at $z \sim 2$ and $z \sim 3$ with a few results at higher and lower redshifts.[24]

Figure 23 demonstrates the evolution of the UV LF. The number density of bright galaxies increases from $z \sim 6$ to 4, causing a brightening of M^* by $\sim$0.6–0.7 mag. In contrast, the number of faint galaxies appears to undergo less evolution between $z \sim 6$ and $z \sim 4$. To quantify this further, we have calculated the rest-frame 1700 Å unobscured UV luminosity density (LD). The luminosity density and error are estimated by simulating many realizations of the UV LF consistent within the normally distributed LF errors and evaluating the mean luminosity-weighted integral of the LFs from each of these realizations. The mean value and dispersion of these integrated values give the mean luminosity density and error, and the values are listed in Table 12. We have assumed a faint-end slope of $\alpha = -1.6 \pm 0.11$ (i.e., as in § 6.1) at $z \sim 2$. For consistency, all the LFs are integrated to a luminosity limit of $L_{\rm lim} = 0.04L^*_{z=3}$. This corresponds to a luminosity of $L_{\rm lim} = 3.9 \times 10^{27}$ ergs s^{-1} Hz^{-1} at 1700 Å, is equivalent to $\approx 0.05L^*_{z=2}$, and corresponds to an unobscured SFR of $\sim$0.5 $M_\odot$ yr^{-1} assuming the Kennicutt (1998) relation. The right panel of Figure 23 summarizes the integrated (unobscured) UV LD as a function of redshift including several published values, showing the significant evolution between $z \sim 2$ and $z = 0$.

[24] The figure is not meant to be comprehensive with respect to all determinations of the UV LF, particularly at $z \gtrsim 4$, where there are some differences between studies (e.g., Sawicki & Thompson 2006; Ouchi et al. 2004; Iwata et al. 2007; Beckwith et al. 2006).

TABLE 12

SUMMARY OF TOTAL UV, Hα, AND IR LUMINOSITY DENSITIES AT $1.9 \leq z < 3.4$

Redshift Range	UV LD[a] (ergs s^{-1} Hz^{-1} Mpc^{-3})	Hα LD (ergs s^{-1} Mpc^{-3})	IR LD[b] ($L_\odot$ Mpc^{-3})
$1.9 \leq z < 2.7$	$(3.63 \pm 0.40) \times 10^{26}$	$(4.41 \pm 1.10) \times 10^{40}$	$(1.23 \pm 0.21) \times 10^{9}$
$2.7 \leq z < 3.4$	$(2.29 \pm 0.34) \times 10^{26}$	$(2.71 \pm 0.57) \times 10^{40}$	$(6.61 \pm 1.24) \times 10^{8}$

[a] Uncorrected for extinction and integrated to $0.04L^*_{z=3}$.

[b] Values assume the Caputi et al. (2007) calibration between $\nu L_\nu(8\ \mu{\rm m})$ and $L_{\rm IR}$. The IR LD at $z \sim 2$ includes the contribution from ULIRGs (Caputi et al. 2007).

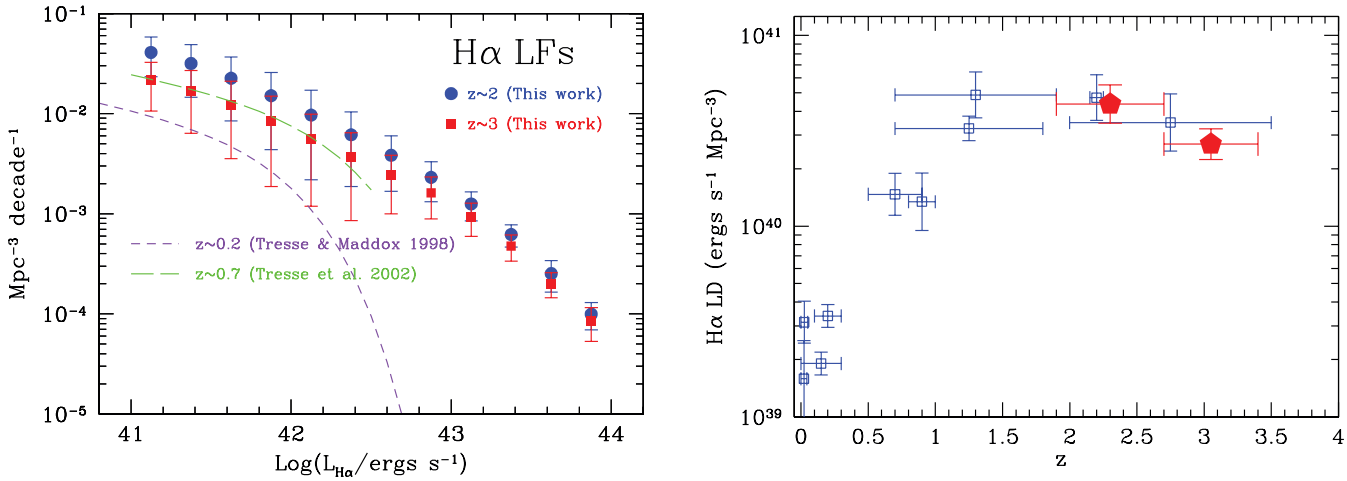

FIG. 24.—*Left*: Comparison of our inferred dust-corrected Hα luminosity function at $z \sim 2$ and predicted one at $z \sim 3$, with the direct Hα LF determinations at lower redshift from Tresse et al. (2002); Tresse & Maddox (1998). *Right*: Extinction-corrected Hα luminosity density: open squares are from Hopkins (2004) and include determinations from Gallego et al. (1995), Pérez-González et al. (2003), Sullivan et al. (2000), Tresse & Maddox (1998), Tresse et al. (2002), Glazebrook et al. (1999), Hopkins et al. (2000), Yan et al. (1999), and Moorwood et al. (2000). The point at $z = 2.75$ is the Hβ determination from Pettini et al. (1998). The large red pentagons denote values from this work.

While the observed evolution in the UV LF is hardly surprising, we have placed this evolution during the most active epoch of star formation ($z \sim 2$–4) on a secure footing with our extensive spectroscopic analysis and detailed completeness corrections. Our analysis covers a larger number of uncorrelated fields than what has typically been considered in previous studies, thus enabling us to mitigate the effects of sample variance. We note that part of the evolution of the unobscured UV LF may be a result of extinction, as we will discuss shortly.

8.3.2. Hα *LFs*

Figure 24 compares our inference of the Hα LF at $z \sim 2$ and our prediction at $z \sim 3$, with the direct determinations at lower redshifts by Tresse & Maddox (1998) and Tresse et al. (2002). The evolution of the dust-corrected Hα LF qualitatively mimics the evolution observed in the UV LF (Fig. 23) for redshifts $z \lesssim 2$–3. We see a factor of 2 decline in the number density of moderately luminous galaxies with 10^{41} ergs s^{-1} $< L(\mathrm{H}\alpha) <$ $10^{42.5}$ ergs s^{-1} from $z \sim 2$ to $z \sim 0.7$. The decline of moderately luminous galaxies is at least a factor of 4–10 between $z \sim 2$ and $z \sim 0.2$.

The systematic excess of $z \sim 2$ galaxies with respect to $z \sim 3$ for luminosities $L(\mathrm{H}\alpha) \lesssim 10^{43}$ ergs s^{-1} is primarily a result of the fact that galaxies on the faint end of the UV LF (where we observed the same small systematic excess; see Fig. 12) are scattered to correspondingly more luminous bins of Hα luminosity after correcting for extinction. The significance of the systematic excess at $z \sim 2$ with respect to $z \sim 3$ is hard to judge since, unlike the case with the UV LFs, there are no direct determinations of the Hα LFs at $z \gtrsim 2$. What is certain is that the number (and luminosity) density of moderately Hα-luminous galaxies at $z \sim 2$ is *at least* as large as the number at $z \sim 3$. In contrast, the significance of the increased frequency of moderately luminous galaxies at $z \sim 2$ with respect to $z \sim 0.7$ is supported by the fact that the Hα luminosity density shows a decline from $z \sim 2$ to $z = 0$. To illustrate this, we have compiled estimates of the Hα LD from Hopkins (2004) in the right panel of Figure 24, including our new inferences at $z \sim 2$ and $z \sim 3$ (the latter are listed in Table 12). Values from Hopkins (2004) have been reddening-corrected assuming a luminosity dependent obscuration correction. Our values at $z \sim 2$ and $z \sim 3$ are computed from the dust-corrected Hα LFs. Quantitatively, the Hα LD per comoving Mpc decreases by a factor ~25 between $z \sim 2$ and the local value. While Hβ observations have been performed for a handful of objects at $z \sim 3$ (Pettini et al. 1998), larger samples are needed to directly constrain the Hα LF at $z \sim 3$. Since our Hα results on the SFRD are degenerate with those estimated from the UV and IR LFs, we will not discuss the Hα LFs any further.

8.4. *Average Extinction and IR and Bolometric LFs*

8.4.1. *Evolution of Dust Obscuration with Redshift*

As mentioned in § 8.3.1, the evolution observed in the unobscured rest-frame UV LF between $z \sim 2$ and $z = 0$ may be partly a result of systematic differences in extinction with redshift. It is already known that galaxies of a fixed bolometric luminosity have an average attenuation factor at $z \sim 2$ that is ~8–10 times smaller than the attenuation factors of local galaxies (Reddy et al. 2006b; Burgarella et al. 2007; Buat et al. 2007). Figure 25, adapted from Reddy et al. (2006b) and the *GALEX* results of Buat et al. (2006) and Burgarella et al. (2007) illustrates the offset between the $z \sim 2$, $z \sim 1$, and $z = 0$ trends between L_{bol} and attenuation. Reddy et al. (2006b) interpreted this trend as a result of the increasing extinction per unit SFR (or increasing dust-to-gas ratio) as galaxies age. The dependence of attenuation on bolometric luminosity at low redshifts has been discussed by many authors (e.g., Buat et al. 2005; Pérez-González et al. 2003; Afonso et al. 2003; Sullivan et al. 2001; Hopkins et al. 2001a, 2001b). The analyses of Reddy et al. (2006b), Adelberger & Steidel (2000), and Figure 25 demonstrate that this dependence continues unabated from $z = 0$ to $z \sim 2$–3.

If the LF was unevolving between $z \sim 2$ and $z = 0$, then the offset shown in Figure 25 implies that, when integrating the UV (or Hα) LF to a fixed luminosity, the extinction correction will be larger at lower redshifts. However, as Figures 23 and 24 demonstrate, there is a very strong evolution in the LF between $z \sim 2$ and $z \sim 0$. We find a similar evolution in the IR LFs and IR LDs, shown in Figures 26 and 27, respectively, where we summarize the comparison between the $z \sim 2$ and $z \sim 3$ IR LFs and luminosity densities from our analysis with other published measurements. The important point is that the average extinction correction needed to recover bolometric LDs from UV LDs will depend both on the

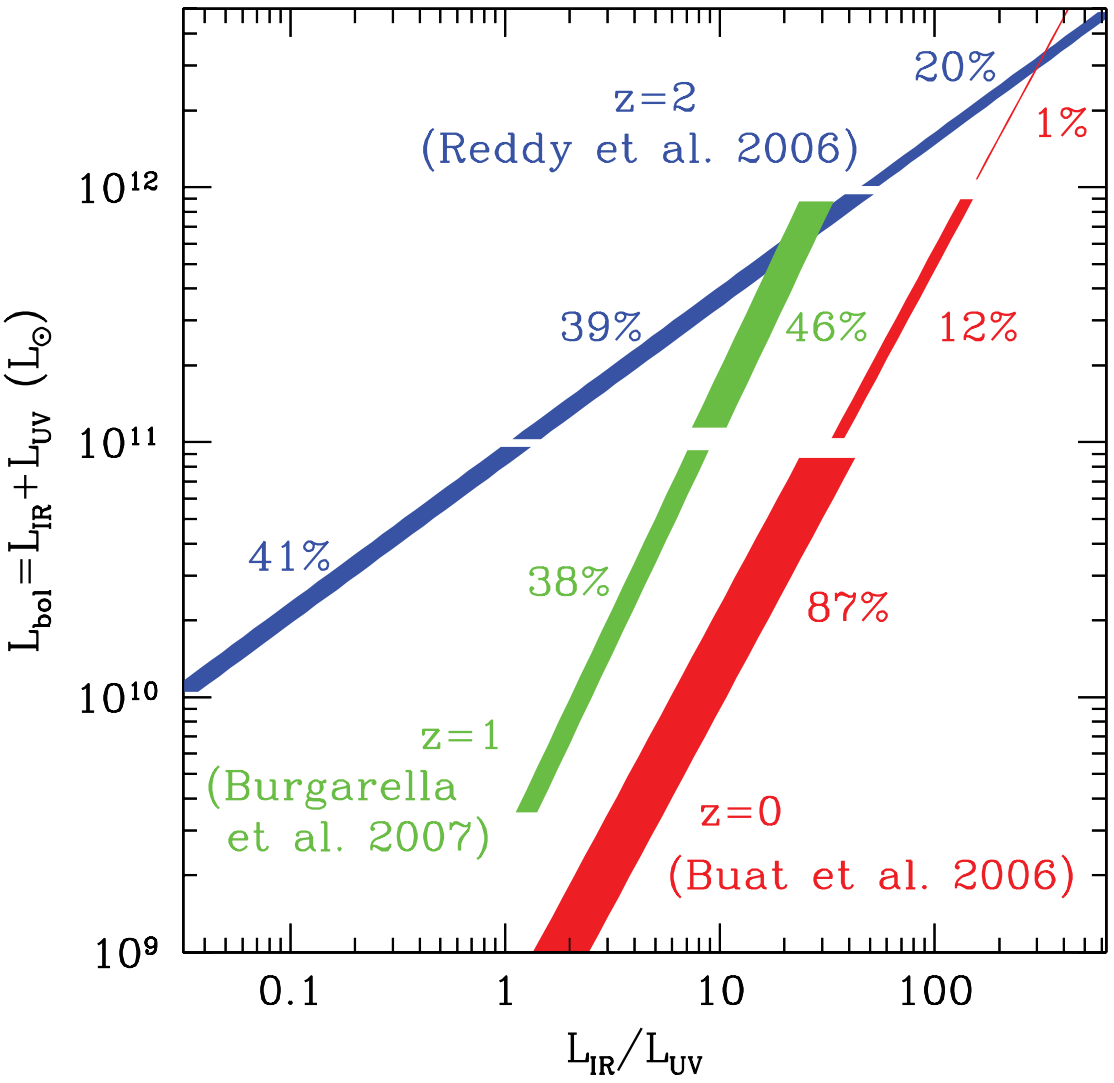

FIG. 25.— Trend between bolometric luminosity and dust attenuation based on the analyses of Reddy et al. (2006b) at $z \sim 2$, Burgarella et al. (2007) at $z \sim 1$, and Buat et al. (2006) at $z \sim 0$. The thickness of the lines show schematically the contribution of galaxies in different ranges of bolometric luminosity to the bolometric luminosity density, with the relative fractions listed. Fractional contributions at $z \sim 2$ were determined from our estimate of the bolometric LF at this epoch (Fig. 20). The contributions at $z \sim 0$ and $z \sim 1$ were taken from Le Floc'h et al. (2005).

offset in the L_{bol} versus attenuation trends between $z \sim 2$ and $z = 0$, as well as the relative numbers of galaxies in different luminosity ranges that contribute to the LD. For example, LIRGs at $z \sim 2$ are on average 8–10 times less dusty than LIRGs at $z = 0$, but there are many more LIRGs at $z \sim 2$ than at $z \sim 0$. The contribution of galaxies in different luminosity ranges to the bolometric LD at $z \sim 2$, $z \sim 1$, and $z = 0$ are shown schematically in Figure 25.

If the IR LF was unevolving between $z \sim 2$ and $z = 0$, then the fact that galaxies of a fixed L_{bol} are 8–10 times less dusty at $z \sim 2$ than at $z \sim 0$ would imply that the average extinction correction needed to recover the bolometric LD from the UV LD would be roughly 8–10 times *larger* at $z \sim 0$ than at $z \sim 2$. However, because of the evolution in number density, the average correction at $z \sim 0$ is not 8–10 times larger than the value at $z \sim 2$. Schiminovich et al. (2005) find an average attenuation factor for UV-selected samples at $z \lesssim 1$ of $\langle L_{bol}/L_{UV} \rangle \sim 7$, which is only 1.6 times larger than the value of 4.5 found for UV-selected galaxies at $z \sim 2$–3. It is interesting to note that even taking into account the evolution in number density, the average correction at $z \sim 0$ is still larger than the correction at $z \sim 2$, despite a greater fraction of the LD in dustier galaxies at high redshift. This result may be partly due to the redshift evolution in L_{bol} versus attenuation trend (Fig. 25), but the larger correction at $z \sim 0$ may also be needed to account for IR-luminous galaxies that altogether escape UV selection at $z \sim 0$.

8.4.2. *Evolution of the Dust-obscured and Bolometric Luminosity Densities*

There are several important conclusions to draw from our analysis of the IR luminosity density. First, the unobscured UV LD drops by a factor ~23 between $z \sim 2$ and $z \sim 0$, whereas the IR LD drops by a factor of ~14 between $z \sim 2$ and the present day. This difference can be partly accounted for by an evolution in the average extinction correction, as discussed in the previous section. The *independent* determinations of the average extinction corrections at $z \sim 2$ ($\langle L_{bol}/L_{UV} \rangle \sim 4.5$; Reddy et al. 2006b) and at $z \sim 0$ ($\langle L_{bol}/L_{UV} \rangle \sim 7$; Schiminovich et al. 2005) result in an evolution of the dust-corrected UV LD that is in remarkable agreement with the evolution of the IR LD between $z \sim 2$ and $z = 0$ (see § 8.5).

Second, the IR LD at $z \sim 2$ appears to be at least as large as the value at $z \sim 3$, a result consistent with that of the UV LD analysis.

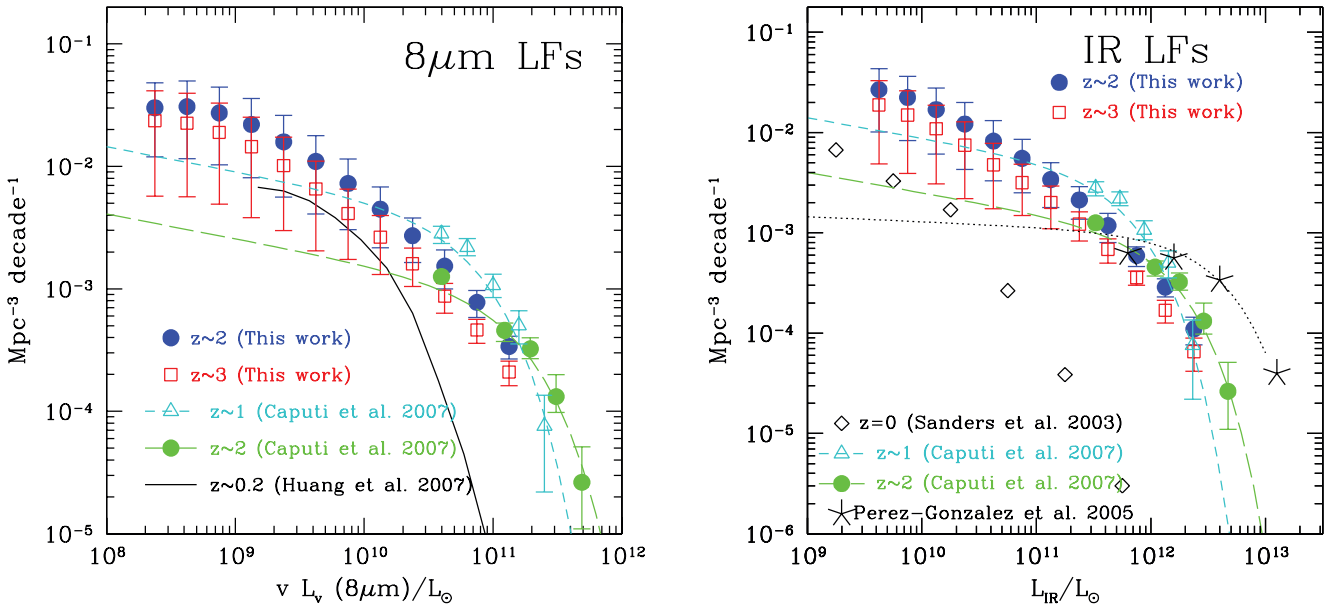

FIG. 26.— Comparison of our inference of the 8 μm (*left*) and IR LFs (*right*) at $z \sim 2$ and our prediction at $z \sim 3$, with direct measurements from the literature: $z \sim 1$ and $z \sim 2$ points from Caputi et al. (2007) and Pérez-González et al. (2005), 8 μm LF at $z \sim 0.2$ from Huang et al. (2007), and the local IR LF from the *IRAS* BGS sample (Sanders et al. 2003). The Pérez-González et al. (2005) points at $z \sim 2$ are significantly larger than those of Caputi et al. (2007) primarily because the former exclude only the most extreme AGNs from their analysis and adopt a conversion between rest-frame mid-IR and IR luminosity that has been shown to overpredict the bolometric luminosities of $\gtrsim 2 \times 10^{12}\ L_{\odot}$ galaxies by a factor of >2 (Papovich et al. 2007; Daddi et al. 2007b; see text).

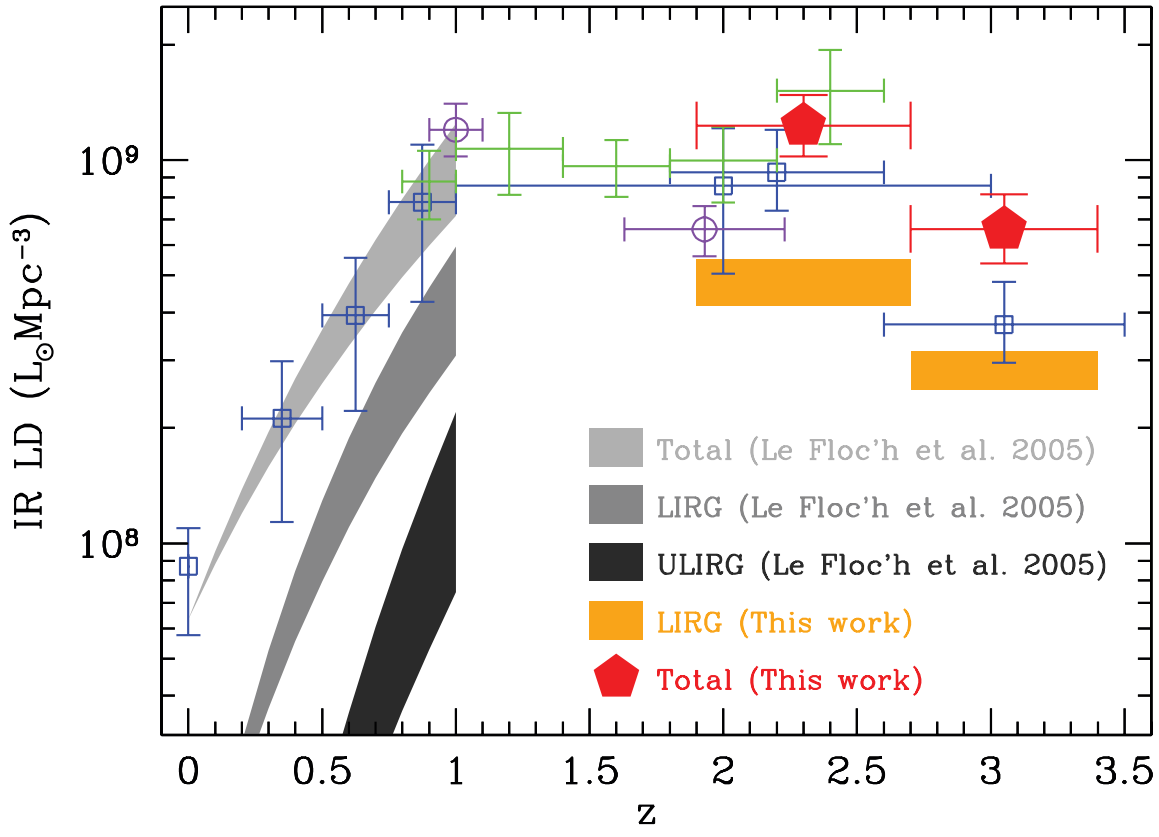

FIG. 27.— Infrared luminosity density as a function of redshift, including data from Yun et al. (2001) at $z = 0$, Flores et al. (1999) at $0.2 \lesssim z \lesssim 1.0$, Barger et al. (2000) at $z \sim 2$, and Chapman et al. (2005) at $z \gtrsim 2$; all shown with open squares. Results from Caputi et al. (2007) and Pérez-González et al. (2005) are shown by the open circles and green lines, respectively. Our points at $1.9 \leq z < 2.7$ and $2.7 \leq z < 3.4$ are shown by the solid pentagons, assuming the Caputi et al. (2007) calibration between $\nu L_{\nu}(8\ \mu\mathrm{m})$ and L_{IR}. The Reddy et al. (2006b) calibration would raise the points by ≈30%. The ULIRG, LIRG, and total contributions to the IR LD inferred by Le Floc'h et al. (2005) are indicated by the light, medium, and dark gray shaded regions, respectively, up to $z = 1$. The inferred contribution of LIRGs from our analysis at $z \sim 2$–3 is denoted by the shaded rectangles.

This should not come as a surprise since the same incompleteness-corrected rest-frame UV LF was used to infer the IR LF. Nonetheless, our *spectroscopic* analysis puts the constraints on the Hα and IR LD on a more secure footing. In particular, our analysis provides the first spectroscopic constraints on the sub-ULIRG regime of the IR LFs at $z \gtrsim 2$.

Third, the constraints on the IR LD between $1.9 \leq z < 3.4$ yield critical information on the relative contribution of galaxies to the IR LD as a function of luminosity. Figure 26 hints that previous studies of the IR LF at $z \sim 2$ underpredicted the number (and luminosity) density of sub-ULIRGs with $L_{\rm IR} < 10^{12}\,L_{\odot}$ (i.e., compare our IR LF points with the extrapolation of Pérez-González et al. (2005) and Caputi et al. (2007) for galaxies with $L_{\rm IR} < 10^{12}\,L_{\odot}$ in Fig. 26). When integrating the IR LF to account for *all* galaxies, we find a total IR LD of $\sim 1.2 \times 10^{9}\,L_{\odot}\ {\rm Mpc}^{-1}$, about a factor of 2 larger than the previous determination at $z \sim 2$. Note that the Pérez-González et al. (2005) determination of the IR LD at $z \sim 2.4$ is consistent with our measurement, primarily for two reasons. First, they only excluded the most extreme AGNs, which by number made up 5% of their sample, whereas other surveys indicate a larger contamination rate of 10%–20% (see § 3.2 of Pérez-González et al. 2005 and references therein). Second, Pérez-González et al. (2005) use a conversion relation between rest-frame 12 μm and IR luminosity that has been shown to overproduce by factors of >2 the IR luminosities of the most IR-luminous galaxies based on 70 and 160 μm stacking analysis (Papovich et al. 2007). This result is also supported by Daddi et al. (2007b), who also find a systematic excess of rest-frame 8 μm emission relative to UV and radio emission for a sample of $z \sim 2$ star-forming ULIRGs. Further, Daddi et al. (2007a) suggest that the obscured AGN fraction among ULIRGs at $z \sim 2$ is significantly larger than previously inferred. A more conservative approach of excluding IR-luminous AGNs, e.g., such as that adopted by Caputi et al. (2007) and assuming their calibration between 8 μm and IR luminosity, results in an IR LD from ULIRGs that is roughly a factor of 2–3 lower than the Pérez-González et al. (2005) determination. The critical point of this discussion is that, while both the Pérez-González et al. (2005) and Caputi et al. (2007) studies were able to probe the ULIRG regime of the IR LF with a high degree of completeness, the shallowness of their data precluded strong constraints on galaxies significantly fainter than $10^{12}\,L_{\odot}$. Our sample and analysis yield the first constraints on the IR and bolometric LFs for *moderately* luminous galaxies at redshifts $1.9 \leq z < 3.4$, thus allowing us to evaluate the unobscured SFRD over a larger range of intrinsic luminosity and redshift than previously possible. Our results suggest that the luminosity density contributed by sub-ULIRGs with $L_{\rm IR} < 10^{12}\,L_{\odot}$ at $z \sim 2$ is larger than previously inferred. Table 10 indicates that such galaxies would comprise roughly 70% of the total IR LD at $z \sim 2$.

It is important to take a step back at this point and reexamine the systematic effects induced by the unknown attenuation distribution of UV faint galaxies, since this is the dominant uncertainty in our determination of the faint end of the IR LF. The only way to reconcile the relatively steep faint end slope of the UV LF ($\alpha = -1.6$) with the shallow faint-end slope of the IR LF as suggested by Caputi et al. (2007) and Pérez-González et al. (2005) is if there is a sudden change in the attenuation properties of UV galaxies such that those with $\mathcal{R} > 25.5$ have negligible dust attenuation. The implication is that such UV-faint galaxies would be forming stars in pristine metal-poor ISM with very low dust-to-gas ratios, akin to "dwarf" galaxies in the local universe. While there are certainly likely to be such dwarfs at high redshift, they would have to dominate the number counts on the faint end of the UV LF. Future deep spectroscopic observations should place both the determination of the UV faint-end slope and the extinction properties of sub-L* galaxies on a more secure footing. However, as we discuss in the next section, comparison of our *total* IR LDs with those corresponding to SFRD values estimated in previous studies (e.g., Reddy et al. 2005) suggest the IR LD cannot be much lower than the value derived here, effectively placing a constraint on the attenuation of sub-ULIRGs.

Finally, we note that UV emission comprises a non-negligible fraction of the bolometric luminosity of LIRGs. This is an effect that becomes more pronounced at higher redshift as the average dust attenuation of galaxies of a given bolometric luminosity decreases, as already discussed. The bolometric LFs derived in § 6 allow us to assess the contribution of galaxies to the total LD, taking into account both the obscured (IR) and unobscured (UV) luminosity densities. The total bolometric luminosity density can be calculated by integrating our bolometric LF from $L \sim 0$ to $L = 10^{12}\,L_{\odot}$, and adding the contribution of ULIRGs from Caputi et al. (2007). Assuming that the fraction of bolometric luminosity emergent in the UV in ULIRGs is negligible, then the total bolometric LD at $z \sim 2$ is $\approx 1.5 \times 10^{9}\,L_{\odot}\ {\rm Mpc}^{-3}$. Roughly 80% of this bolometric LD arises from galaxies with $L_{\rm bol} \lesssim 10^{12}\,L_{\odot}$. This bolometric LD is more than 25% larger than what we would have inferred from the IR LF alone because the former includes the contribution of the LD emergent at UV wavelengths.

To summarize, there are essentially four points worth keeping in mind from our analysis of the IR and bolometric LD. First, the evolution of the UV LD shows a marked difference from the evolution of the dust-corrected Hα and IR LDs between $z \sim 2$ and $z \sim 0$. The difference can be explained by an evolution in the average extinction correction between $z \sim 0$ and $z \sim 2$. Second, we find that the IR LD at $z \sim 2$ is at least as large as the value at $z \sim 3$, implying that the decline in SFRD to the local value must have occurred after $z \sim 2$. Third, while our analysis becomes increasingly incomplete for the most luminous galaxies at $z \sim 2$–3, it *does* provide the first spectroscopic constraints on the moderate luminosity (e.g., LIRG) regime of the IR LF. Even taking into account the significant uncertainties associated with the dust obscuration of UV-faint galaxies, these results suggest that previous studies have significantly underestimated the contribution of galaxies with $L_{\rm IR} \lesssim 10^{12}\,L_{\odot}$ to the IR luminosity density. Finally, taking into account the emergent UV luminosity density of galaxies, we find that sub-ULIRG galaxies comprise roughly 80% of the total *bolometric* LD at $z \sim 2$. In the next section, we will discuss these results in the context of the global SFRD.

8.5. *Constraints on the Global Star Formation Rate Density*

We have converted the results of Figure 23 and 27 to star formation rates (SFRs) using the Kennicutt (1998) relations and assuming a Salpeter (1955) IMF from 0.1 to 100 $M_{\odot}$, with the results summarized in Figure 28.[25] The UV points at low redshift ($z \lesssim 1$) are corrected assuming a factor of 7 attenuation (Schiminovich et al. 2005). Our UV points are corrected by an average factor of 4.5 (e.g., Reddy et al. 2006b; Reddy & Steidel 2004; Nandra et al. 2002; Steidel et al. 1999). Note the difference in extinction correction between the low-redshift points and our $z \sim 2$–3 determinations, again reflecting the dependence of extinction on redshift. The higher redshift points of Bouwens et al. (2007) are corrected according to the extinction factors published therein. While there are a number of systematics that can affect our interpretation of SFRD plots such as Figure 28 (e.g.,

[25] Assuming the more realistic Chabrier (2003) IMF will reduce the SFRD by a factor of $\sim$1.8.

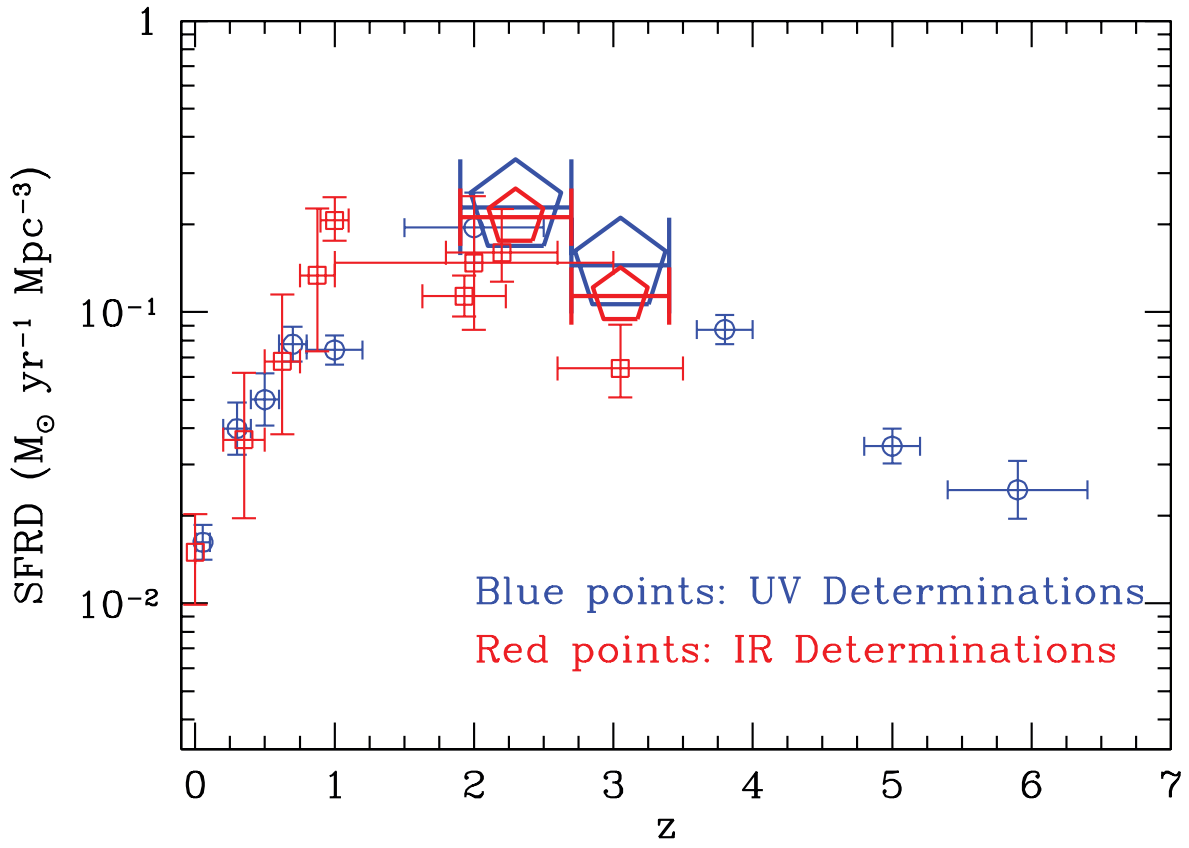

FIG. 28.—Summary of UV (*blue open circles*) and IR (*red open squares*) estimates of the global star formation rate density as a function of redshift. The UV points have been corrected for extinction in a differential manner (i.e., as a function of redshift): determinations at $z \lesssim 1$ are corrected by a factor of 7; our values at $z \sim 2$ and $z \sim 3$ are corrected by an average factor of 4.5; the high-redshift ($z \gtrsim 4$) determinations are corrected by the factors given in Bouwens et al. (2007): the dust corrections at $z \sim 4$–5 are determined from a linear interpolation of the $z \sim 3$ and $z \sim 6$ values. Our dust-corrected UV determinations are indicated by the large blue pentagons. Our IR estimates, computed using a differential extinction recipe with UV magnitude (see § 6.3) and which includes the contribution of ULIRGs from Caputi et al. (2007) at $z \sim 2$, are indicated by the red open pentagons. The errors on our UV and IR determinations at $z \sim 2$ and $z \sim 3$ are ~20% (derived from the errors on the luminosity density) and are smaller than the size of the large pentagons.

changes in the IMF with redshift), our analysis has allowed us to carefully and quantitatively assess two of these systematics: accounting for sample incompleteness and extinction. Our measurements indicate an SFRD at $z \sim 2$ that is *at least* as large as the value at $z \sim 3$. Applying a factor of 4.5, as suggested by stacking analyses (e.g., Reddy & Steidel 2004; Reddy et al. 2006b; Nandra et al. 2002), to correct our UV estimates for extinction yields values that are in general accord with the IR estimates. On the one hand, we might not have expected such good agreement given that the factor of 4.5 has only been measured for LIRGs, and the average factor applied to the *total* UV LD may be lower depending on the extinction of UV-faint galaxies. However, we note that the IR-estimated SFRD includes the contribution from ULIRGs (whereas the UV-estimated SFRD does not explicitly take them into account), so the difference in the two estimates is less than we might have expected. The important point is that despite the significant uncertainties regarding the attenuation of UV-faint galaxies, applying a factor of 4.5 to total UV LDs as advocated in many studies is not too far off from the value obtained from IR estimates.

As alluded to previously, independent estimates of the SFRD based on "census" studies of high-redshift galaxies (Reddy et al. 2005) can be compared with our completeness-corrected estimate. Such census studies estimate the global SFRD by adding up the contribution from galaxies directly targeted by various selection criteria. For example, Reddy et al. (2005) estimated the SFRD at $z \sim 2$ by taking into account the overlap between galaxies selected using the BX, *BzK* (Daddi et al. 2004b), Distant Red Galaxy (DRG; Franx et al. 2003) criteria, and submillimeter selection (e.g., Chapman et al. 2005). Taking into account the overlap between galaxies selected using these methods, Reddy et al. (2005) compute an SFRD at $z \sim 2$ of $0.15 \pm 0.03\ M_\odot\ \mathrm{yr}^{-1}\ \mathrm{Mpc}^{-3}$ for galaxies with $\mathcal{R} < 25.5$, $K_s(\mathrm{AB}) < 23.8$, including the contribution from submillimeter-bright ($S_{850\ \mu\mathrm{m}} \gtrsim 5$ mJy) galaxies. Since the total SFRD cannot be smaller than that derived from census studies of directly detected (optical, near-IR, and submillimeter bright) galaxies, it suggests that our SFRD measurement cannot be significantly lower than the value derived here, $\sim 0.2\ M_\odot\ \mathrm{yr}^{-1}\ \mathrm{Mpc}^{-3}$. This in turn implies that the attenuation of sub-ULIRGs cannot be so low as to bring down our total SFRD estimate to the point where it is in violation of the census-computed SFRD. As an example, integrating the Caputi et al. (2007) IR LF at $z \sim 2$ yields an IR LD of $\sim 6.6^{+1.2}_{-1.0} \times 10^8\ L_\odot\ \mathrm{Mpc}^{-3}$, corresponding to an SFRD of $0.11^{+0.2}_{-0.1}\ M_\odot\ \mathrm{yr}^{-1}\ \mathrm{Mpc}^{-3}$. This "total" value is already comparable to, if not smaller than, the census value of $0.15 \pm 0.03\ M_\odot\ \mathrm{yr}^{-1}\ \mathrm{Mpc}^{-3}$ (Reddy et al. 2005); the latter can be treated as a lower limit to the SFRD. The implications are that the faint end of the IR LF is unlikely to be as shallow as that predicted from previous IR surveys, that such UV-faint galaxies are likely to have non-negligible dust attenuation, and that the contribution of sub-ULIRGs to the total LD and SFRD must be larger than previously inferred. Finally, we note that there are no observational constraints on the presence of dusty LIRGs at $z \sim 2$–3 that are both faint in the UV *and* fall below the detection

threshold of the *Spitzer* surveys. However, large numbers of such UV-faint dusty LIRGs would serve to increase the average attenuation of UV-faint galaxies and would strengthen our conclusions regarding the increased contribution of sub-ULIRGs to the total LD and SFRD at $z \sim 2$–3.

One of the principle conclusions from this work is that galaxies with $L_{\rm IR} \approx L_{\rm bol} \lesssim 10^{12}\ L_{\odot}$ account for ≈70% of the SFRD at $1.9 \leq z < 2.7$. The fraction rises to ∼80% if we take into account the emergent UV luminosity density of sub-ULIRGs. Our analysis suggests that much of the star formation activity at $z \sim 2$ may take place in faint and moderately luminous galaxies. As a consequence, such faint to moderate luminosity galaxies must have accounted for a significant fraction of the stellar mass density formed between $z \sim 3$ and $z \sim 2$. Assuming a constant SFRD of $\sim 0.16\ M_{\odot}\ {\rm yr}^{-1}\ {\rm Mpc}^{-3}$ (i.e., the average of our IR estimates of the SFRD at $z \sim 2$ and 3) between $z = 3.4$ and $z = 1.9$ (the limiting redshifts of our analysis) implies that ∼45% of the total stellar mass density of the universe (e.g., Cole et al. 2001) formed between these redshifts (e.g., see also Dickinson et al. 2003). If the fraction of the luminosity density contributed by galaxies with $L_{\rm bol} \lesssim 10^{12}\ L_{\odot}$ is roughly constant (≈80%) between $z = 3.05$ and $z = 2.3$, as suggested by our analysis, then it implies that one-third of the present-day stellar mass density was formed in such galaxies.[26]

Finally, including the $z \gtrsim 4$ rest-frame UV determinations (no such corresponding Hα or IR data exist at corresponding redshifts), suggests that the SFRD falls off at these early epochs (e.g., Bouwens et al. 2006 and references therein). Assuming a constant IMF implies that the SFRD at $z \sim 2$ is a factor of ∼9 larger than that observed at $z \sim 6$ (corrected for extinction). This trend may be suggesting a hierarchical buildup of galaxies at early times. The important result of our analysis is that this "growth" appears to halt and stay constant for roughly 1.2 Gyr, between $z \sim 4$ and $z \sim 2$ (Fig. 23). This result is not far from expectations if the rate of galaxies that are commencing rapid star formation and populating the bright end of the UV LF is offset by the rate of galaxies that are fading because of gas exhaustion or some other truncation of the star formation such as through AGN or supernova feedback (e.g., Kriek et al. 2006; Reddy et al. 2006b, 2005; Erb et al. 2006c). In fact, this very epoch hosts the emergence of a significant population of quiescent galaxies (e.g., Franx et al. 2003; Rudnick et al. 2003; van Dokkum et al. 2004; Reddy et al. 2005, 2006b; Kriek et al. 2006). The balance between rapidly star-forming galaxies and those that are fading appears to saturate around $z \sim 1$–2, at which point the latter becomes the dominant effect, leading to a decrease in the number density of bright galaxies between $z \sim 2$ and $z = 0$ (Fig. 23). As discussed above, this reversal in the evolution of the UV LF is likely due to gas exhaustion resulting from any number of processes (e.g., SN-driven outflows, AGN feedback; see also Bell et al. 2005). Once gas exhaustion has occurred and star formation proceeds quiescently, at least a couple of mechanisms have been proposed to explain why gas is unable to cool onto galaxies with the largest stellar masses, including AGN feedback (Croton et al. 2006; Scannapieco et al. 2005; Granato et al. 2004) and dilution of infalling gas due to virial shock (Dekel & Birnboim 2006). It is interesting to note that it is around this epoch, $z \sim 2$, that AGN activity appears to peak (e.g., Hopkins et al. 2007; Fan et al. 2001; Shaver et al. 1996).

[26] We assume a Salpeter IMF in these calculations. A Chabrier IMF will reduce the stellar mass density estimates by a factor of ∼1.8, but the relative contribution of sub-ULIRGs between $z = 3.05$ and $z = 2.3$ to the present-day stellar mass density will be the same, assuming the IMF does not evolve between $z \sim 2$–3 and the present day.

9. CONCLUSIONS

We have used the largest existing sample of spectroscopic redshifts in the range $1.9 \leq z < 3.4$ to evaluate the luminosity functions (LFs) of star-forming galaxies at rest-frame UV, Hα, and infrared (IR) wavelengths. The sample of rest-frame UV-selected galaxies includes ∼15,000 photometric candidates in 29 independent fields (for a total area of ∼0.9 deg^2) of which ∼2000 have spectroscopic redshifts $1.9 \leq z < 3.4$. The large spectroscopic database yields critical constraints on the contamination fraction of our sample from objects at lower redshifts ($z < 1.4$) and AGNs/QSOs; statistics that are vital to accurately estimate the bright end of the LFs. We use our extensive sample to correct for incompleteness and recover the intrinsic rest-frame UV LF at $z \sim 2$ and 3. Combining this result with Hα and *Spitzer* MIPS data in several of our fields enables us to infer the Hα and IR LFs of star-forming galaxies. The principle conclusions of this work are as follows:

1. The fraction of star-forming galaxies with rest-frame Lyα equivalent widths $W_{\rm Ly\alpha} > 20$ Å in emission ($f20$) increases with redshift in the range $1.9 \leq z < 3.4$, independent of selection bias, from a value of 8% at $1.90 \leq z < 2.17$ to 23% for Lyman break galaxies at $2.70 \leq z < 3.40$. If the general expectation is that young and less dusty galaxies show Lyα in emission, then the trend of increasing $f20$ with redshift reflects the decrease in average galaxy age and metallicity with increasing redshift.

2. Based on integrating our maximum likelihood LFs, the fraction of star-forming galaxies with redshifts $1.9 \leq z < 2.7$ and $M_{\rm AB}(1700\ {\rm Å}) < -19.33$ that have colors that satisfy BX criteria is ≈58%. Similarly, the fraction of star-forming galaxies with redshifts $2.7 \leq z < 3.4$ and $M_{\rm AB}(1700\ {\rm Å}) < -20.02$ that have colors that satisfy the LBG criteria is ≈47%. The total fraction of $1.9 \leq z < 3.4$ galaxies with $\mathcal{R} < 25.5$ that satisfy either the BX or LBG criteria is 55%. We find little evolution in the rest-frame UV LF between $z \sim 3$ and $z \sim 2$. Correcting for extinction implies the dust-corrected UV luminosity density at $z \sim 2$ is at least as large as the value at $z \sim 3$, and roughly 9 times larger than the value at $z \sim 6$. This evolution reverses at redshifts $z \lesssim 2$, where gas exhaustion is likely to dominate the evolution of UV-bright galaxies.

3. The incompleteness-corrected estimates of the $E(B - V)$ distribution indicate that there is very little evolution in the average dust extinction of galaxies between $z \sim 3$ and $z \sim 2$ and that such a distribution is approximately constant to our spectroscopic limit of $\mathcal{R} = 25.5$. These results are in agreement with stacked X-ray analyses of $z \sim 2$–3 galaxies (Reddy & Steidel 2004; Nandra et al. 2002). However, examining the attenuation distribution of galaxies over a larger dynamic range in lookback time indicates an increasing extinction per unit star formation rate with decreasing redshift (Reddy et al. 2006b; Buat et al. 2007). The implication of this trend in average extinction is that the evolution in the dust-corrected UV LD is less and more pronounced, respectively, at low ($z \lesssim 2$) and high ($z \gtrsim 2$) redshift than what one would have predicted from the observed UV LD (e.g., see also Bouwens et al. 2006).

4. Factoring in the contamination rate of our sample from galaxies at lower redshifts and AGNs/QSOs with redshifts $2.7 \leq z < 3.4$, we find no evidence for an excess of UV-bright galaxies over what was inferred in the initial LBG studies of Steidel et al. (1999) and Dickinson (1998) as has been recently claimed.

5. The incompleteness-corrected rest-frame UV-selected sample and deep *Spitzer* MIPS data in multiple fields are combined to yield the first spectroscopic constraints on the faint and moderate luminosity sub-ULIRG ($L_{\rm IR} \lesssim 10^{12}\ L_{\odot}$) regime of the total infrared

luminosity functions at $z \sim 2$ and 3. We use this information to show that the number density of $L_{IR} \lesssim 10^{12}\ L_{\odot}$ galaxies has been significantly underestimated by previous studies that have relied on shallower IR data. After accounting for the emergent UV luminosity, and assuming a realistic range of attenuation for UV faint galaxies, we find that ≈80% of the bolometric (IR+UV) luminosity density at $z \sim 2$ comes from galaxies with $L_{bol} < 10^{12}\ L_{\odot}$. Assuming a constant SFRD of 0.16 $M_{\odot}\ yr^{-1}\ Mpc^{-3}$ between $z = 3.4$ and $z = 1.9$ (the limiting redshifts of our $z \sim 2$–3 analysis), suggests that $L_{bol} < 10^{12}\ L_{\odot}$ galaxies at these redshifts were responsible for approximately one-third of the buildup of the present-day stellar mass density.

6. Our estimate of the total SFRD at $z \sim 2$ is consistent with the lower limit on the SFRD provided by census studies of optical, near-IR, and submillimeter bright galaxies at similar redshifts (Reddy et al. 2005). Our analysis takes into account the systematics associated with the attenuation of UV-faint ($\mathcal{R} > 25.5$) galaxies. Assuming more extreme changes in the dust attenuation of UV-faint galaxies than considered here would be required to reconcile the steep and shallow faint-end slopes of the UV and IR LFs, respectively, implying that the vast majority of UV-faint galaxies would be forming stars from chemically pristine gas. However, such an extreme scenario would result in a *total* SFRD that is comparable to, if not smaller than, the lower limit from census studies (Reddy et al. 2005). The implications are that some significant fraction of sub-ULIRGs must have non-negligible dust extinction, the faint end of the IR LF must be steeper than what previous studies have suggested, and the contribution of sub-ULIRGs to the total SFRD must be significantly larger than previously inferred.

We acknowledge useful conversations with Rychard Bouwens, Emeric Le Floc'h, Casey Papovich, Marcin Sawicki, and Lin Yan. We thank Emeric Le Floc'h for providing data from Le Floc'h et al. (2005) in electronic format, Rychard Bouwens for a careful reading of the manuscript, and the referee for helpful suggestions to improve the clarity of the paper. This work would not have been possible without the support of the staff of the Keck Observatory. The work presented here has been supported by grants AST 03-07263 and AST 06-06912 from the National Science Foundation and by the David and Lucile Packard Foundation.

REFERENCES

Abraham, R. G., et al. 2004, AJ, 127, 2455
Adelberger, K. L. 2002, Ph.D. thesis, Caltech
Adelberger, K. L., Erb, D. K., Steidel, C. C., Reddy, N. A., Pettini, M., & Shapley, A. E. 2005a, ApJ, 620, L75
Adelberger, K. L., Shapley, A. E., Steidel, C. C., Pettini, M., Erb, D. K., & Reddy, N. A. 2005b, ApJ, 629, 636
Adelberger, K. L., & Steidel, C. C. 2000, ApJ, 544, 218
Adelberger, K. L., Steidel, C. C., Shapley, A. E., Hunt, M. P., Erb, D. K., Reddy, N. A., & Pettini, M. 2004, ApJ, 607, 226
Adelberger, K. L., Steidel, C. C., Shapley, A. E., & Pettini, M. 2003, ApJ, 584, 45
Afonso, J., Hopkins, A., Mobasher, B., & Almeida, C. 2003, ApJ, 597, 269
Alexander, D. M., et al. 2003, AJ, 126, 539
Arnouts, S., et al. 2005, ApJ, 619, L43
Barger, A. J., Cowie, L. L., & Richards, E. A. 2000, AJ, 119, 2092
Barger, A. J., Cowie, L. L., Sanders, D. B., Fulton, E., Taniguchi, Y., Sato, Y., Kawara, K., & Okuda, H. 1998, Nature, 394, 248
Beckwith, S. V. W., et al. 2006, AJ, 132, 1729
Bell, E. F., et al. 2005, ApJ, 625, 23
Blain, A. W., Smail, I., Ivison, R. J., Kneib, J.-P., & Frayer, D. T. 2002, Phys. Rep., 369, 111
Bolzonella, M., Miralles, J.-M., & Pelló, R. 2000, A&A, 363, 476
Bouwens, R. J., Illingworth, G. D., Blakeslee, J. P., & Franx, M. 2006, ApJ, 653, 53
Bouwens, R. J., Illingworth, G. D., Thompson, R. I., & Franx, M. 2005, ApJ, 624, L5
Bouwens, R. J., et al. 2004, ApJ, 616, L79
———. 2007, ApJ, 670, 928
Buat, V., Marcillac, D., Burgarella, D., Le Floc'h, E., Rieke, G., Takeuchi, T. T., Iglesias-Paramo, J., & Xu, C. K. 2007, A&A, 469, 19
Buat, V., et al. 2005, ApJ, 619, L51
———. 2006, preprint (astro-ph/0609738)
Bunker, A., Stanway, E., Ellis, R., McMahon, R., Eyles, L., & Lacy, M. 2006, NewA Rev., 50, 94
Bunker, A. J., Stanway, E. R., Ellis, R. S., & McMahon, R. G. 2004, MNRAS, 355, 374
Burgarella, D., Le Floc'h, E., Takeuchi, T. T., Huang, J. S., Buat, V., Rieke, G. H., & Tyler, K. D. 2007, preprint (arXiv:0706.0810)
Calzetti, D., Armus, L., Bohlin, R. C., Kinney,. A. L., Koornneef, J., & Storchi-Bergmann, T. 2000, ApJ, 533, 682
Caputi, K. I., et al. 2007, ApJ, 660, 97
Chabrier, G. 2003, PASP, 115, 763
Chapman, S. C., Blain, A. W., Ivison, R. J., & Smail, I. R. 2003, Nature, 422, 695
Chapman, S. C., Blain, A. W., Smail, I., & Ivison, R. J. 2005, ApJ, 622, 772
Cole, S., et al. 2001, MNRAS, 326, 255
Conselice, C. J., et al. 2004, ApJ, 600, L139
Cowie, L. L., Barger, A. J., Hu, E. M., Capak, P., & Songaila, A. 2004, AJ, 127, 3137
Croton, D. J., et al. 2006, MNRAS, 365, 11
Daddi, E., Cimatti, A., Renzini, A., Fontana, A., Mignoli, M., Pozzetti, L., Tozzi, P., & Zamorani, G. 2004a, ApJ, 617, 746
Daddi, E., et al. 2004b, ApJ, 600, L127
———. 2007a, preprint (arXiv:0705.2832)
———. 2007b, preprint (arXiv:0705.2831)
Dekel, A., & Birnboim, Y. 2006, MNRAS, 368, 2
Di Matteo, T., Croft, R. A. C., Springel, V., & Hernquist, L. 2003, ApJ, 593, 56
Dickinson, M. 1998, in The Hubble Deep Field, ed. M. Livio, S. M. Fall, & P. Madau (Cambridge: Cambridge Univ. Press), 219
Dickinson, M., Papovich, C., Ferguson, H. C., & Budavári, T. 2003, ApJ, 587, 25
Dickinson, M., et al. 2004, ApJ, 600, L99
Dow-Hygelund, C. C., et al. 2007, ApJ, 660, 47
Erb, D. K., Shapley, A. E., Pettini, M., Steidel, C. C., Reddy, N. A., & Adelberger, K. L. 2006a, ApJ, 644, 813
Erb, D. K., Steidel, C. C., Shapley, A. E., Pettini, M., Reddy, N. A., & Adelberger, K. L. 2006b, ApJ, 647, 128
———. 2006c, ApJ, 646, 107
Fan, X., et al. 2001, AJ, 121, 54
Finkelstein, S. L., Rhoads, J. E., Malhotra, S., Pirzkal, N., & Wang, J. 2007, ApJ, 660, 1023
Flores, H., et al. 1999, ApJ, 517, 148
Franx, M., et al. 2003, ApJ, 587, L79
Gabasch, A., et al. 2004, ApJ, 616, L83
Gallego, J., Zamorano, J., Aragon-Salamanca, A., & Rego, M. 1995, ApJ, 455, L1
Giavalisco, M., Koratkar, A., & Calzetti, D. 1996, ApJ, 466, 831
Giavalisco, M., et al. 2004, ApJ, 600, L93
Glazebrook, K., Blake, C., Economou, F., Lilly, S., & Colless, M. 1999, MNRAS, 306, 843
Granato, G. L., De Zotti, G., Silva, L., Bressan, A., & Danese, L. 2004, ApJ, 600, 580
Hansen, M., & Oh, S. P. 2006, MNRAS, 367, 979
Hopkins, A. M. 2004, ApJ, 615, 209
Hopkins, A. M., Connolly, A. J., Haarsma, D. B., & Cram, L. E. 2001a, AJ, 122, 288
———. 2001b, AJ, 122, 288
Hopkins, A. M., Connolly, A. J., & Szalay, A. S. 2000, AJ, 120, 2843
Hopkins, P. F., Richards, G. T., & Hernquist, L. 2007, ApJ, 654, 731
Huang, J. S., et al. 2007, ApJ, 664, 840
Hughes, D. H., et al. 1998, Nature, 394, 241
Iwata, I., Ohta, K., Tamura, N., Akiyama, M., Aoki, K., Ando, M., Kiuchi, G., & Sawicki, M. 2007, MNRAS, 376, 1557
Kennicutt, R. C. 1998, ARA&A, 36, 189
Kriek, M., et al. 2006, preprint (astro-ph/0611724)
Law, D. R., Steidel, C. C., Erb, D. K., Pettini, M., Reddy, N. A., Shapley, A. E., Adelberger, K. L., & Simenc, D. J. 2007, ApJ, 656, 1
Le Fèvre, O., et al. 2005, Nature, 437, 519

Le Floc'h, E., et al. 2005, ApJ, 632, 169
Lehnert, M. D., & Bremer, M. 2003, ApJ, 593, 630
Lilly, S. J., Le Fevre, O., Hammer, F., & Crampton, D. 1996, ApJ, 460, L1
Lilly, S. J., Tresse, L., Hammer, F., Crampton, D., & Le Fevre, O. 1995, ApJ, 455, 108
Madau, P. 1995, ApJ, 441, 18
Madau, P., Ferguson, H. C., Dickinson, M. E., Giavalisco, M., Steidel, C. C., & Fruchter, A. 1996, MNRAS, 283, 1388
Maraston, C., Daddi, E., Renzini, A., Cimatti, A., Dickinson, M., Papovich, C., Pasquali, A., & Pirzkal, N. 2006, ApJ, 652, 85
Marchesini, D., et al. 2007, ApJ, 656, 42
McLean, I. S., et al. 1998, Proc. SPIE, 3354, 566
Meurer, G. R., Heckman, T. M., & Calzetti, D. 1999, ApJ, 521, 64
Moorwood, A. F. M., van der Werf, P. P., Cuby, J. G., & Oliva, E. 2000, A&A, 362, 9
Nandra, K., Mushotzky, R. F., Arnaud, K., Steidel, C. C., Adelberger, K. L., Gardner, J. P., Teplitz, H. I., & Windhorst, R. A. 2002, ApJ, 576, 625
Oke, J. B., & Gunn, J. E. 1983, ApJ, 266, 713
Ouchi, M., et al. 2004, ApJ, 611, 660
Paltani, S., et al. 2007, A&A, 463, 873
Papovich, C., Dickinson, M., & Ferguson, H. C. 2001, ApJ, 559, 620
Papovich, C., Giavalisco, M., Dickinson, M., Conselice, C. J., & Ferguson, H. C. 2003, ApJ, 598, 827
Papovich, C., et al. 2006, ApJ, 640, 92
———. 2007, preprint (astro-ph/07062164)
Pentericci, L., Grazian, A., Fontana, A., Salimbeni, S., Santini, P., De Santis, C., Gallozzi, S., & Giallongo, E. 2007, preprint (astro-ph/0703013)
Pérez-González, P. G., Zamorano, J., Gallego, J., Aragón-Salamanca, A., & Gil de Paz, A. 2003, ApJ, 591, 827
Pérez-González, P. G., et al. 2005, ApJ, 630, 82
Pettini, M., Kellogg, M., Steidel, C. C., Dickins on, M., Adelberger, K. L., & Giavalisco, M. 1998, ApJ, 508, 539
Pirzkal, N., Malhotra, S., Rhoads, J. E., & Xu, C. 2006, preprint (astro-ph/0612513)
Reddy, N. A., Erb, D. K., Steidel, C. C., Shapley, A. E., Adelberger, K. L., & Pettini, M. 2005, ApJ, 633, 748
Reddy, N. A., & Steidel, C. C. 2004, ApJ, 603, L13
Reddy, N. A., Steidel, C. C., Erb, D. K., Shapley, A. E., & Pettini, M. 2006a, ApJ, 653, 1004
Reddy, N. A., Steidel, C. C., Fadda, D., Yan, L., Pettini, M., Shapley, A. E., Erb, D. K., & Adelberger, K. L. 2006b, ApJ, 644, 792
Rudnick, G., et al. 2003, ApJ, 599, 847
Salpeter, E. E. 1955, ApJ, 121, 161
Sanders, D. B., Mazzarella, J. M., Kim, D.-C., Surace, J. A., & Soifer, B. T. 2003, AJ, 126, 1607
Sawicki, M., & Thompson, D. 2006, ApJ, 642, 653
Scannapieco, E., Silk, J., & Bouwens, R. 2005, ApJ, 635, L13
Schechter, P. 1976, ApJ, 203, 297
Schiminovich, D., et al. 2005, ApJ, 619, L47
Shapley, A. E., Steidel, C. C., Adelberger, K. L., Dickinson, M., Giavalisco, M., & Pettini, M. 2001, ApJ, 562, 95
Shapley, A. E., Steidel, C. C., Erb, D. K., Reddy, N. A., Adelberger, K. L., Pettini, M., Barmby, P., & Huang, J. 2005, ApJ, 626, 698
Shapley, A. E., Steidel, C. C., Pettini, M., & Adelberger, K. L. 2003, ApJ, 588, 65
Shaver, P. A., Wall, J. V., Kellermann, K. I., Jackson, C. A., & Hawkins, M. R. S. 1996, Nature, 384, 439
Smail, I. 2003, in The Mass of Galaxies at Low and High Redshift, ed. R. Bender & A. Renzini (Berlin: Springer), 310
Smail, I., Ivison, R. J., & Blain, A. W. 1997, ApJ, 490, L5
Stanway, E. R., et al. 2007, MNRAS, 376, 727
Steidel, C. C., Adelberger, K. L., Giavalisco, M., Dickinson, M., & Pettini, M. 1999, ApJ, 519, 1
Steidel, C. C., Adelberger, K. L., Shapley, A. E., Erb, D. K., Reddy, N. A., & Pettini, M. 2005, ApJ, 626, 44
Steidel, C. C., Adelberger, K. L., Shapley, A. E., Pettini, M., Dickinson, M., & Giavalisco, M. 2003, ApJ, 592, 728
Steidel, C. C., Hunt, M. P., Shapley, A. E., Adelberger, K. L., Pettini, M., Dickinson, M., & Giavalisco, M. 2002, ApJ, 576, 653
Steidel, C. C., Pettini, M., & Hamilton, D. 1995, AJ, 110, 2519
Steidel, C. C., Shapley, A. E., Pettini, M., Adelberger, K. L., Erb, D. K., Reddy, N. A., & Hunt, M. P. 2004, ApJ, 604, 534
Sullivan, M., Mobasher, B., Chan, B., Cram, L., Ellis, R., Treyer, M., & Hopkins, A. 2001, ApJ, 558, 72
Sullivan, M., Treyer, M. A., Ellis, R. S., Bridges, T. J., Milliard, B., & Donas, J. 2000, MNRAS, 312, 442
Takeuchi, T. T., Buat, V., & Burgarella, D. 2005, A&A, 440, L17
Tapken, C., Appenzeller, I., Noll, S., Richling, S., Heidt, J., Meinköhn, E., & Mehlert, D. 2007, A&A, 467, 63
Tresse, L., & Maddox, S. J. 1998, ApJ, 495, 691
Tresse, L., Maddox, S. J., Le Fèvre, O., & Cuby, J.-G. 2002, MNRAS, 337, 369
Valdes, F. 1982, FOCAS User's Manual (Tucson: NOAO)
van Dokkum, P. G., et al. 2003, ApJ, 587, L83
———. 2004, ApJ, 611, 703
Williams, R. E., et al. 2000, AJ, 120, 2735
———. 1996, AJ, 112, 1335
Wirth, G. D., et al. 2004, AJ, 127, 3121
Wyder, T. K., et al. 2005, ApJ, 619, L15
Yan, H., Windhorst, R. A., & Cohen, S. H. 2003, ApJ, 585, L93
Yan, L., McCarthy, P. J., Freudling, W., Teplitz, H. I., Malumuth, E. M., Weymann, R. J., & Malkan, M. A. 1999, ApJ, 519, L47
Yun, M. S., Reddy, N. A., & Condon, J. J. 2001, ApJ, 554, 803